Preparation of charge transfer salt/polymer composites, and characterisation by saturable absorption

Mark Carroll

Preparation of Charge Transfer Salt/Polymer Composites, and Characterisation by Saturable Absorption

A thesis submitted for the degree of

Doctor of Philosophy

By

Mark Carroll

Applied Physics Group

Department of Physics

University of Durham

Declaration

I hereby declare that the work reported in this thesis has not previously been submitted for any degree and is not being currently submitted in candidature for any other degree.

Sign

The work reported in this thesis was carried out by the candidate, other than that acknowledged in the main text.

Signed.....

PhD supervisor

Signed

Candidate

Statement of Copyright

Acknowledgements

I would like to thank Dr. G.H. Cross and Professor D. Bloor for their supervision, guidance and encouragement during the period of my research at Durham. I would also like to thank Dr. A. Blythe, my industrial supervisor for his support. I am endebted the techanical staff of the Applied Physics Group, in particular Mr. N. Thompson and Mr. D. Pattinson for their valuble assistance. Finally I would like to thank my sponsors, the SERC and BICC Cables Ltd. for funding my work.

Dedication

To my parents...

Abstract

This thesis describes the preparation of microcrystalline dispersions of a series of organic semiconductors (the alkali metal salts of tetracyanoquinodimethane) within a host polymer. The linear optical properties of these composites are found to be dependent on the method of preparation. Their third order nonlinear optical properties are then investigated by measurement of the intensity dependence of their transmision. Close to the low energy, local excitation band saturable absorption is observed. In the region of the charge transfer band reverse saturable absorption is observed. The results are discussed in terms of a two level model.

Contents

Chapter 1

Introduction

1.1 The need for nonlinear optical materials

The invention of the laser in the early 1960s (Maiman 1960), with its associated long coherence lengths and high beam intensities, enabled researchers to study a range of physical phenomena for the first time. At high intensities the response of a material to excitation by an optical field, deviates from the normal linear response measured at low light levels, and nonlinear optical (NLO) effects are observed. The optical parameters of the material, such as refractive index and absorption coefficient, become intensity dependent and, depending on the process in question, incident radiation can undergo frequency doubling, and frequency tripling.

It was realised that many of these phenomena had potential technological applications. In particular, following the development of optical fibre communication networks, devices based on NLO effects were proposed which would improve the performance of such networks. In optical fibre networks, information is encoded as modulations in the intensity of a light beam which propagates along the fibre. Such systems offer many advantages over traditional electrical cable based networks e.g. compactness, large bandwidths, freedom from crosstalk etc.. However, certain operations need to be performed on the beam at various points in the network. These include amplification of the signal, which

must be carried out periodically within the network to compensate for losses suffered by the light beam as it passes along the fibre; signal modulation to impress information on the light beam; gating of signals; directional coupling for routing signals. In most current systems these operations are carried out by converting the optical signal to an electrical signal, carrying out the operation and then reconverting to an optical signal. This introduces significant delays into the system. Many of the processes which require such optical-electrical-optical conversion could, in principle, be carried out entirely optically by employing the nonlinear effects described above, thereby avoiding the need for conversion to an electrical signal. This would result in all-optical communication networks. If the goal of such networks, with the associated benefits of large bandwidths, high speed etc., is to be realised, materials exhibiting significant optical nonlinearities at intensities attainable in an optical fibre network are required.

1.2 Nonlinear optical materials

In general a system's response to an impulse can be divided into linear and nonlinear regions. The response is said to be linear when it is directly proportional to the amplitude of the impulse. This is usually the case for low amplitude impulses. For large amplitudes the linear relationship between impulse and response breaks down and the nonlinear regime is reached. When considering the interaction of light with matter, the impulse is the electric field associated with the light beam, and the response is the induced electronic polarisation. At low intensity, the induced polarisation is directly proportional to the electric field. At higher intensities, in order to describe the response fully it is necessary to consider polarisation components proportional to the square and to the cube of the electric field. This additional polarisation contains components oscillating at the frequency of the incident electric field, and to components oscillating at multiples of this fundamental frequency.

The former lead to modified refractive index and absorption properties, the latter lead to harmonic generation.

NLO effects are often divided into quadratic, (second order) and cubic, (third order) effects. This nomenclature indicates whether the effect in question can be traced to induced polarisation components proportional to the square of the electric field (quadratic) or the cube of the electric field (cubic).

In the case of quadratic effects, a non-centrosymmetric structure is required for a non-zero response. $LiNbO_3$ has enjoyed considerable success as a basis for devices such as frequency doublers (Weiss 1985), and electro-optic modulators (Sasahi 1977), which rely on a quadratic response. $LiNbO_3$ does have certain disadvantages, namely it is quite expensive to produce, and is not amenable to integration with Si and GaAs, which is desirable if integrated optical circuits are to be made. In recent years a great deal of interest has been shown in polymeric systems. These have the advantage of high damage thresholds, excellent processibility and comparatively low cost. Several types of system have been investigated: guest/host systems (e.g. Karakus 1992), where an NLO active molecule is dispersed within a passive polymer host; main chain polymers (e.g. Katz 1989), where the NLO molecule forms part of the polymer backbone; and side chain polymer systems (e.g. Ye 1987), where the NLO molecule is attached to part of the polymer backbone. In such systems the required non-centrosymmetry is introduced by electric field induced alignment of the NLO molecules in the thermally softened polymer, followed by slow cooling, with the electric field still applied, to 'freeze in' the alignment. It seems likely that commercial devices using such organic systems will be realised soon, provided problems with thermal and optical stability in these systems can be overcome.

In contrast, materials with sufficiently large cubic nonlinearities to make possible device applications such as all-optical (Kerr) switches and bistable switches have proved elusive. Many types of material system have been studied: semiconductors, (e.g. Ziman 1990), semiconductor multiple quantum wells, (e.g. Berger 1988), semiconductor and metal doped glasses (e.g. Zheludev 1988), but no material with the necessary combination of properties, namely high nonlinearity, low absorption and fast response time has been found.

Over the last twenty years organic materials have been extensively studied with respect to their potential as third order NLO materials. Organic materials are particularly attractive in that there is potential to modify a material's structure using the vast resources of organic chemistry. This allows materials to be synthesised according to theoretically and experimentally determined guidelines for producing highly nonlinear systems. Molecular crystals (e.g. Zyss 1981), as well as polymers such as those of the polydiacetylene family (e.g. Sauteret 1976), have been extensively studied. They exhibit off-resonance, cubic nonlinearities ($\chi^{(3)}_{PTS} = 5x10^{-10}$ e.s.u.), which are comparable to those of inorganic semiconductors. The off-resonance response is purely electronic and is consequently very fast compared to say thermal processes. Members of the polydiacetylene family contain 1-dimensional, planar arrays of linear carbon atom chains, with alternating single, double and triple bonds, which is believed to be the microscopic origin of their nonlinear response.

Prototype devices have been demonstrated using the above types of material. However none of them have been found to be suitable for commercial device manufacture, and consequently new, nonlinear materials are being actively sought.

1.3 TCNQ salt/polymer composites

The aim of this work is to study the properties of a series of organic semiconductors with potential as highly nonlinear optical materials of cubic order. The semiconductors under study are the alkali metal salts of the organic electron acceptor tetracyanoquinodimethane (TCNQ). As described in chapter 2, TCNQ forms a wide range of salts with both organic and inorganic donors. These salts have been widely studied with respect to their magnetic, electrical and linear optical properties (Endres 1983). The existence in these materials of mobile π-electrons with translational freedom in one direction only (see chapter 3), suggested analogy with the polydiacetylene family of polymers mentioned previously, which are known to exhibit large third order nonlinearities. So far, research on the NLO properties of the TCNQ salts has been rare. This is in part due to the difficulty in obtaining samples of the salt in a form facilitating optical measurements: Crystals are small, of low mechanical strength and highly absorbing. Nevertheless, third harmonic generation measurements on powder compactions of Perylene(TCNQ), (Gotoh 1989), indicated a large resonance enhanced third order nonlinearity. The origin of the nonlinearity was believed to be the charge transfer transition between π-electrons associated with neighbouring TCNQ molecules. Using methods outlined in chapter 4 the alkali metal salts of TCNQ can be incorporated into polymer thin films of good optical quality and mechanical strength. The methods used to form the films are similar to those used by Jeszka (1985) and Ulanski (1985) which are described section in 1.4.1. In that work, composites of highly conducting TCNQ salts were studied. The technique became known as 'reticulate doping'. Of greatest interest in this previous work were the electrical properties of the films, with their optical transparency a lower priority. These methods were modified in the present work to enable the production of films containing sub-optical size crystallites (i.e. less than 0.5 μm), which were thus of greater optical quality.

The present work is analogous to that carried out on inorganic semiconductor, and metal particle doped glasses which is described in section 1.4.2. Such systems are promising materials for use in cubic nonlinear optical devices. Size dependent enhancements in the nonlinear optical constants of the dispersed particles have been observed in these systems. These enhancements can be due to dielectric and/or quantum confinement as described in section 1.5. It was hoped that such enhancements might also occur in the organic systems forming the present study.

1.4 Related background work

1.4.1 Reticulate doped polymers (RDPs)

Charge transfer salts were first incorporated into polymers by workers researching into the possibility of forming flexible conducting films from polymers containing highly conducting organic salts (Jeszka 1981), using the method of reticulate doping.

The process of reticulate doping consists of casting films from a solution of a chosen salt and polymer in a common solvent, a typical combination being tetrathiafulvalene-TCNQ and polycarbonate. A film of this solution is cast onto a suitable substrate and conditions are controlled (temperature and pressure for instance), such that, as the solvent evaporates and the film begins to solidify, the salt crystallises out in-situ within the polymer. The mechanical properties of the composite films are determined by the polymer matrix, due to the low concentration of the salt phase (typically less than 2% volume fraction).

The crystallisation process is complicated because of the many interrelated variables which influence it, such as temperature, solubility of the salt additive and of the polymer, rate of solvent evaporation and solution viscosity (which of course changes during the crystallisation process as solvent evaporates from the film). A quantitative theory relating experimental conditions to the resulting crystallite size and morphology has not as yet been formulated. Determination of the conditions which result in a particular crystal morphology within the film remains an empirical procedure. However, certain general guide lines have been determined (Ulanski 1985), and are now described.

Conductivity is found to be highest in films where the crystallite morphology is dendritic in nature, leading to an interlocking network of crystallites. Such morphologies are favoured in systems which use good solvents of the salt in the initial solution. The critical salt concentration at which crystallisation begins to occur is then reached with less solvent remaining in the film corresponding to a high viscosity regime. This reduces salt ion mobility and leads to supersaturation. When crystallisation does finally occur it is very rapid, resulting in a non-equilibrium, dendritic morphology. When poorer solvents of the salt are used, the critical concentration is reached earlier, with more solvent remaining in the film. The prevailing viscosity is then lower, avoiding supersaturation and leading to the normal needle form crystallites exhibited by these salts when grown under equilibrium conditions.

Among the interesting properties of RDPs are the low (0.3% volume fraction), percolation thresholds, i.e. the minimum concentration of dopant salt required to produce a continuous crystalline network, penetrating the polymer film. Such low values of percolation threshold, are due to the structural connectivity of the crystalline network (Ulanski 1985), which leads to highly conducting films even with such low doping levels. The

conductivities of composites containing certain salts are found to be enhanced relative to the values predicted by theory, assuming the crystals in the film have the same conductivity as bulk samples. This has led researchers to believe that different forms of the dopant salts are formed in the composites. This is attributed to the rapid crystallisation in a highly viscous environment, leading to novel forms of the material. For example N-propyl-phthalazinium-tetracyanoquinodimethane, (PrPht(TCNQ)$_2$), formed in poly(bisphenol-A)carbonate using the reticulate doping procedure, is found to have higher conductivity and lower activation energy (smaller band gap), compared to bulk samples of the salt (Tracz 1988). In addition tetrathiatetracene (TTT), and TCNQ in polycarbonate forms dendritic crystals with a 1:1 stoichiometry rather than the 1:2 stoichiometry normally exhibited (Tracz 1986).

A key finding as far as the present work is concerned, is the fact that if film drying is accelerated using reduced pressure and/or heating, crystallisation of the salt can be prevented by the rapidly increasing viscosity. This results in solid films containing the salt molecularly dispersed within the dried film. Subsequent treatment of such films, with vapours capable of infusing the polymer but in which the salt is not soluble, induces crystallisation in the surface layer of the film, (Jeszka 1985).

In general, large crystals (in excess of 10 μm) are formed using the methods described above. One of the aims of the work described in later chapters was to produce much smaller crystallites, so as to reduce light scattering and hence improve film transparency. Furthermore, it was hoped that if sufficiently small crystallites could be produced, enhancements in the NLO properties of dopants, due to effects described in the section 1.5, might be realised.

1.4.2 Inorganic semiconductor doped glasses.

In recent years, semiconductor and metal doped glasses have been studied as promising materials for third order nonlinear optics. As well as determining their potential as NLO materials, nonlinear optical techniques are being used to study the electronic properties of very small crystallites. Due to the homogeneity of the crystallite distribution and its consequent centrosymmetry, quadratic NLO effects are not exhibited by these materials. Instead cubic nonlinear effects - in particular intensity dependent changes in absorption and refractive index are of interest. Techniques for forming such materials have existed for many years and have found applications, for example, in optical cut-off filters. The early research into the NLO properties of these composite media centred on such commercially available glasses. The first NLO study of semiconductor crystallite dispersions was reported in 1964 where absorption saturation was observed in commercial Schott glass filters containing CdSSe (Bret and Gires 1964). Somewhat later Jain & Lind (1983), measured a third order susceptibility $\chi^{(3)}$, in these materials of between 10^{-8} e.s.u. and 10^{-9} e.s.u. close to the absorption edge. These promising results encouraged researchers to develop techniques allowing better control over the characteristics of the dispersions, in particular crystallite size and size distribution.

Semiconductor dispersions have been formed using a number of materials. In glass matrices, a thermal diffusion process is employed (Li-Chi Liu 1990). The constituent ingredients of the glass along with chemicals containing the elements required to form the semiconductor, e.g. Cd, S, Se are heated to high temperatures (up to 1400 °C). These high temperatures cause the chemical bonds to break allowing diffusion of the elements in atomic or ionic form. This leads to a uniform distribution of the semiconductor's constituent elements inside the liquid glass. The glass is then cooled. At this stage, the glass contains nucleation centres of a few hundred atoms in size, but the bulk of the

material is dispersed in ionic or atomic form. The actual crystallites are formed in the striking process which involves the reheating of the glass to around 700 °C. The characteristics of the final dispersions are determined by the striking temperature and the duration of heating.

Dispersions of CdS in Naflon, (perfluoroethylenesulfonic acid polymer), can be formed by H_2S treatment of a Naflon film containing Cd^{2+} ions. The Cd^{2+} ions are introduced by soaking a Naflon film in $Cd(acetate)_2$ for 24 hrs. Crystallites as small as 5 nm can be formed using this method (Hilinski 1988).

Size, and the size distribution of crystallites within these composites has been determined by small angle X-ray scattering and transmission electron microscopy (e.g. Allais 1990). In recent years neutron scattering has also been employed (De Giorgio 1990)

1.5 Confinement effects

One of the reasons for interest in semiconductor/metal doped glasses is the promise of enhancements in their nonlinear optical properties due to crystallite size dependent confinement effects. The two principal mechanisms for such effects are quantum confinement and dielectric confinement which are discussed in the next section.

1.5.1 Quantum confinement

Quantum confinement refers to the confinement of the electrons and holes within a crystallite small enough that their wavefunctions become perturbed by the presence of the

crystallite's boundary. In that case the crystallite cannot be considered to be an infinitely extended periodic system, as required for normal Bloch theory of bulk semiconductors to be applicable. This confinement can radically alter the electron and hole wavefunctions compared to those found in larger, bulk samples resulting in a quite different response to the stimulus of an optical field. In small crystallites the oscillator strength becomes concentrated in the sharp excitonic transitions of lower energy and the dominant nonlinear process becomes that of state filling of these excitonic transitions, as opposed to the band filling mechanism predominant in bulk materials, (Schmitt-Rink, 1987). This can lead to an enhanced third order nonlinear response. As described in appendix 1, the degree of confinement can be described as weak, intermediate or strong depending on the relative size of electron Bohr radius, a_e, hole Bohr radius, a_h, and crystallite radius, a.

Weak confinement refers to situations where $a_h < a_e < a$, intermediate confinement refers to situations where $a_h < a < a_e$ and strong confinement refers to situations where $a < a_h < a_e$.

The crystallite radius at which a system changes from one confinement regime to another depends on the semiconductor in question. Confinement effects appear for larger crystallite dimensions in materials with small electron and hole effective masses as such materials have larger bulk excitonic Bohr radii. For the same reason materials with a small bulk band gap (and larger dielectric constants), exhibit these effects for larger particle sizes. To maximise the enhancement of nonlinearity in these materials, it is important to produce dispersions of narrow crystallite size distribution. If this is not the case inhomogeneous broadening can greatly decrease the size of the enhancement (Banyai 1988).

Theoretically, it has been suggested that third order optical nonlinearity should increase monotonically with increasing degree of confinement, i.e. with decreasing crystallite size

(Banyai 1988). This is found to be the case experimentally in weakly confined and intermediate confined systems. For example Roussignol (1989), noted an enhancement in the magnitude of $\chi^{(3)}$ of CdSe crystals with decreasing size, by up to a factor of two compared to the bulk. Crystallite sizes were of 10-100 nm and therefore in the weak confinement regime (exciton Bohr radius in CdSSe=7.5 nm, (Efros 1982).

In recent years better fabrication techniques have enabled research to be performed on crystallite dispersions of dimensions where strong confinement effects are expected to become manifest. Measurements of the dependence of $\chi^{(3)}$ on crystallite size has produced some conflict with the calculations of Banyai (1988), which predict that greatest nonlinearity is exhibited by crystals suffering strong, as opposed to intermediate quantum confinement. For instance Shonojima (1991), noted a decrease in the magnitude of $\chi^{(3)}$ of $CdS_{0.2}Se_{0.88}$ crystallites in glass, in going to smaller crystallite size: $|\chi^{(3)}|$ fell from 10^{-9} esu to 10^{-11} esu as crystallite size fell from 100 Å to 10 Å. Biexponential temporal decay of the nonlinearity was observed. The fast decay component was attributed to carrier recombination at the surface of the crystallite and the slow decay to recombination inside the crystallite. The slow decay contribution decreased with diminishing crystallite size until only the fast component remained. The effective lifetime of the nonlinearity fell from, 70 ps to 2 ps as crystallite radii decreased from 100 Å to 10 Å. Park (1990) also noted a decrease in the magnitude of $\chi^{(3)}$ with decreasing size of CdSSe crystals. Vandyshev (1992), measured a decrease, of two orders of magnitude in both the real and imaginary parts of $\chi^{(3)}$ in CdSe microcrystals as crystallite radius was decreased from 100 Å to 35 Å. A mechanism for the reduction of nonlinearity with decreasing crystallite size was proposed by Vandyshev (1992). The reduction was assigned to a decrease in carrier lifetime in the smaller crystals due to an increase in radiationless recombination through surface states.

The presence of surface impurities in a crystallite can play an important role in determining a crystallites NLO properties. Wang (1991) proposed a novel mechanism for inducing optical nonlinearities in small semiconductor crystallites. After excitation by a laser pulse an electron hole pair is generated which is bounded by the crystallite surface. Because of the large surface area of the crystallite there is a high probability that the exciton will be rapidly trapped by surface defects. The presence of this trapped exciton perturbs the crystallite's absorption and produces resonant optical nonlinearity. Experiments have shown that the exciton absorption in CdS microcrystals of radius ~ 40 Å, is bleached during the lifetime of the exciton but recovers as the exciton decays (Wang 1991). From the intensity dependence of the bleaching efficiency in CdS crystallites it has been found that bleaching saturates when there is one trapped exciton per crystallite (Hilinski 1988). This was explained as being due to the existence of a strong interaction between the trapped exciton and an exciton which is subsequently excited. Wang (1991) described the interaction as being due to the decreased degree of overlap between the electron and hole wave functions of the newly formed exciton in the presence of the trapped exciton. This decrease in overlap is due to the hole associated with the newly formed exciton being trapped by the electron of the trapped exciton. Thus the wave function of the hole becomes localised whereas that of the free electron, with its smaller effective mass remains delocalised. The reduction in wavefunction overlap results in a reduction in oscillator strength by up to 90%.

The majority of work on semiconductor doped glasses has been carried out in the resonant regime i.e. close to or above the onset of absorption. This is because below this onset, the properties of the composite are dominated by the host medium due to the small volume fraction of crystallites present - typically 0.1%. However nonresonant studies of CdS clusters, capped with thiophenolate to halt crystallite growth, in DMF (Cheng 1989), have shown that individual clusters possess large intrinsic nonresonant nonlinearity ($\chi^{(3)}$= 3.2 x

10^{-10} e.s.u at 1.91μm). Nonlinearity increased with crystallite size in the size range studied (1.5 nm to 3 nm). Work is now underway to grow single crystals made up of these capped clusters which would result in a much higher volume fraction of CdS clusters. Thus these quantum confined systems also have potential as nonresonant nonlinear media.

The organic salts forming the basis of the present study have contrasting electronic properties to the inorganic semiconductors studied in the work described above. As described in chapter 3, the TCNQ salts possess quasi-one-dimensional electronic systems strongly influenced by Coulomb correlations. Thus it is not clear how quantum confinement, if it is manifest at all, would be influenced by the properties of microcrystals of these salts.

1.5.2 Dielectric confinement

Dielectric confinement effects are caused by the difference between the microscopic electric field which acts to polarise the crystallites and the macroscopic electric field associated with an incident light wave. Two sources of dielectric confinement effects exist. The first depends on the difference between the dielectric constant of the dispersed particles and of the surrounding medium. The theory describing it, which is outlined in appendix 1, is applicable to very small crystallites - i.e. much smaller than the wavelength of the incident light. This mechanism is subsequently termed the small particle, or SP-dielectric confinement effect. As described in appendix 1, SP-dielectric confinement results in an enhancement in the third order susceptibility by the fourth power of the local field correction factor f_1 according to the equation.

$$\tilde{\chi}^{(3)} = V|f_1^2|f_1^2\chi^{(3)} \qquad (1.1)$$

Where V is the volume fraction of crystallites, and $\tilde{\chi}^{(3)}$ and $\chi^{(3)}$ are the third order susceptibility of medium as a whole and of the dispersed crystallites respectively

For larger crystals the SP-dielectric confinement effect, though still present, is often swamped by the second dielectric confinement effect, subsequently referred to as large particle or LP-dielectric confinement. It is caused by resonances which can occur between light of the correct wavelength, and the natural optical modes, supported by the crystallites. Such resonances lead to large electric fields within the crystallite. A physical interpretation of these resonances is that light rays propagating within the crystallite are confined by near total internal reflection at the crystal surfaces and after crossing the particle, return to their starting position in phase. Consequently very large intensities can build up within the crystallite, (Hill 1988). Enhancements are particularly large if the crystallites have symmetrical shapes such as spheres or cylinders. The interactions can be explained in terms of Lorenz-Mie theory (Kerker 1969). Wang (1991), calculated the near field solutions of Lorenz-Mie theory for spheres of radii in the 10-1000 nm region. A factor Q_{NF} was defined which is a measure of the local field intensity at the surface of the crystallite. Q_{NF} is given by.

$$Q_{NF} = \frac{1}{\pi} \int_0^{2\pi} \int_0^{\pi} E_s . E_s^* \sin\theta d\theta d\phi \qquad (1.2)$$

Where E_S is the scattered electric field intensity at the surface of the sphere which is calculated using Lorenz-Mie theory.

Calculations for CdS crystals, (Wang 1991), indicate that for very small crystals (less than 50 nm) Q_{NF} is small (typically 1-2), and so little enhancement in the field within the crystal

results. For sizes up to 100 nm, Q_{NF} increases monotonically up to a value around 10. For still larger particles, the behaviour of Q_{NF} depends on whether the exciting wavelength is in a strongly absorbing or weakly absorbing region. In a weakly absorbing region, as crystallite radius goes from 200 nm to 700 nm, Q_{NF} oscillates with increasing crystal size. Sharp peaks in Q_{NF} are found, corresponding to crystal sizes at which the light field is in resonance with the modes of the crystallite. To indicate the extent of these oscillations, under illumination by light of wavelength 641nm, the value of Q_{NF} for crystallites of radius around 550 nm, oscillates between 6 and 18 as crystallite radius changes by ± 50 nm. Thus Q_{NF} is very sensitive to crystallite size. For an incident wavelength in a strongly absorbing region these oscillations though present are suppressed. The general trend of Q_{NF} is now to decrease as crystallite size increases from 100 nm. For instance, for excitation of CdS spheres with light of wavelength 515 nm Q_{NF} has a maximum value of 10 for crystals of around 100 nm radius. For further increases in crystal size Q_{NF} exhibits a downward trend onto which oscillations of around ±1 are superimposed corresponding to resonances between the optical field and the modes of the crystallites.

It should be noted that the large oscillations in Q_{NF} are only observable for particles with a narrow size distribution. If this is not the case an approximately constant value of Q_{NF} (around 8 in the case of CdS) is exhibited over the entire optical wavelength range.

Thus LP-dielectric confinement can produce large enhancements in the local field (and hence in the effective value of $\chi^{(3)}$), especially in the low absorption regions where strong resonances of Q_{NF} occur. It is clear that in the case of non-resonant nonlinearities, in semiconductor doped glasses, this type of dielectric confinement can play an important part

in enhancing third order susceptibilities. Experimental results indicating such enhancements have been obtained via third harmonic generation measurements on distributions of CdS crystals of varying sizes (Cheng 1989). In the case of resonant nonlinearity local-field effects have been suggested as a mechanism for producing optical bistability in semiconductor microcrystallites (Chemla 1986).

1.6 Layout of thesis

Chapter 2 describes in more detail the materials forming the basis of this study - salts of tetracyanoquinodimethane, (TCNQ). Chapter 3 sets out the theoretical models used to describe the electronic properties of quasi one-dimensional electronic systems present in the salts of TCNQ, with particular reference to the linear optical properties. Chapter 4 describes the methods used to form the microcrystalline dispersions of the alkali metal salts of TCNQ in poly(methyl methacrylate) and discusses the factors affecting the resulting crystallite morphology. Chapter 5 reports the results of linear absorption measurements on the composite films, and proposes explanations for the observed shifts in the position of the low energy, charge transfer band. Chapter 6 describes the results of refractive index measurements made on composite films and uses them to calculate the dielectric constant of the dispersed crystallites. Chapter 7 describes intensity dependent transmission measurements carried out on composite films, in the region of the low energy local excitation (LE1) band associated with the $TCNQ^-$ ion, and in the region of the charge transfer (CT) band associated with electron transfer between neighbouring $TCNQ^-$ ions. These measurements are used to calculate the imaginary part of the third order susceptibility of the composite films and of the dispersed crystallite. Comparison is made between these measured nonlinearities, and those of other materials whose third order NLO properties are currently being investigated. Finally, chapter 8 summarises the work.

Chapter 2

Properties of Tetracyanoquinodimethane and its Salts

2.1 Tetracyanoquinodimethane

7,7,8,8-Tetracyanoquinodimethane, (TCNQ) was first synthesised in the early 1960s (Acker 1962). It was soon demonstrated that TCNQ was able to act as an efficient electron acceptor and to form a large number of salt-like derivatives with both organic and inorganic electron donor species (Melby 1962). As well as arousing interest from synthesis chemists, research demonstrated that the family of TCNQ salts possessed many interesting physical properties, some of which are outlined below, and which attracted physicists to the study of these materials.

2.1.1 Structure and physical properties of TCNQ

TCNQ is a yellow/brown crystalline substance with a melting point of 297 °C. The structure of the TCNQ molecule is shown schematically in figure 2.1. It has a quinoid ring structure at its heart with an associated π-orbital electron system. It is a highly symmetrical, planar molecule. In the solid crystalline state, its structure consists of planes

of TCNQ molecules, arranged in stacks, with an inter-molecular separation of 3.45 Å. TCNQ has a room temperature conductivity of around $2x10^{-12}$ $\Omega^{-1}cm^{-1}$ and an activation energy of 0.6 eV (Bespelov 1975).

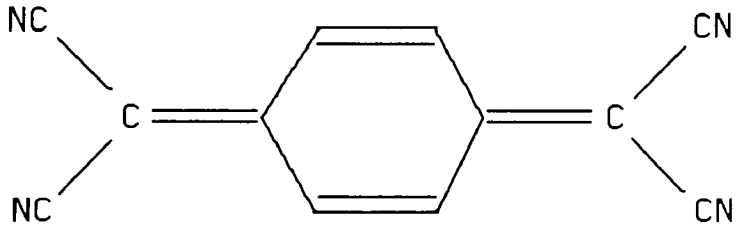

Figure 2.1 The TCNQ molecule

2.1.2 Chemical properties

TCNQ undergoes 1,6-addition reactions, the simplest being reduction by, for example, hydriodic acid, forming $(TCNQ)H_2$. In principle substitution reactions involving the hydrogen atoms and the CN groups are possible though reactions of the former type are rare. Examples of the second type include reactions with primary and secondary amines (Bespalov 1975).

Of more interest to the present discussion is the ability of TCNQ to form complexes with electron donating compounds. The TCNQ molecule's planarity, coupled with the powerful electron withdrawing effect of the four cyano groups, leads to TCNQ having a high electron affinity. With weak electron donors such as aromatic hydrocarbons, TCNQ forms π-complexes (charge transfer complexes), in which partial charge transfer takes place between the donor and TCNQ molecule. In such complexes, structures consisting of stacks

of alternate TCNQ and donor molecules are generally formed in the solid state, (Kobayashi 1974, Yakushi 1974), this is often termed a mixed stack structure. The molecular planes of donor and acceptor are approximately parallel with interplanar distances typically 3.3-3.7 Å. In such materials the molecules are held together by weak Van der Waals forces.

TCNQ also forms a series of salt-like derivatives in which charge transfer between donor and TCNQ is more complete forming the $TCNQ^-$ anion. For so-called simple salts the general formula is $M^{n+}(TCNQ)_n^-$. The visible absorption spectra of such compounds in solution contain bands typical of donor cations and of $TCNQ^-$ anions. The structure of these materials can be mixed stack as described above (Hanson 1965), or can consist of separate donor and TCNQ stacks of evenly spaced groups of molecules which can be arranged as dimers, triads or tetrads, (Etemad 1975). This latter type of crystal structure is referred to as a segregated stack. An example of such a structure is shown in figure 2.1a.

With certain donors, salts form in which formally neutral TCNQ molecules exist along with TCNQ anions in the stack. These are termed complex salts and have the general formula $M^{n+}(TCNQ)_n^-\ (TCNQ)^0$. The visible absorption spectra of these salts in solution exhibit absorption bands typical of $(TCNQ)^0$, in addition to those of the ion radicals. In certain materials, notably salts with 2:3 stoichiometry, X-ray data has indicated the presence of triads in which a $(TCNQ)^0$ molecule lies between two $TCNQ^-$ ions e.g. $(Trimethylammonium)_2(TCNQ)_3$, (Kobayashi 1973). However in most complex salts the charge seems to be evenly distributed between the TCNQ molecules (Bespalov 1975). These salt-like derivatives are discussed further in the next sections.

2.2 Conduction properties of TCNQ salts.

One of the striking features of the TCNQ salts is the wide range of conductivities exhibited by various members of the series. Examples of insulators, semiconductors and what can be termed organic metals are known, (Torrance 1977). A great deal of research has been carried out in an effort to determine the factors affecting conductivity. Certain crystal structural features have been found to be favourable for high conductivity. The segregated stack structure described in the previous section is often associated with high conductivities whereas the mixed stack structure tends to produce much lower conductivity systems, (Herbstein 1971).

The conductivity of salts and charge transfer complexes exhibiting a segregated stack structure is highly anisotropic. Overlap of π-orbitals on adjacent TCNQ molecules leads to extended electron states down the stack producing an essentially one dimensional electronic structure. The conductivity along the TCNQ stacking axis can be as much as two or three thousand times larger than that perpendicular to the stacking axis (Brau 1974).

Conductivity is also influenced by the type of overlap between neighbouring TCNQ molecules. High conductivity is favoured when overlap of π-orbitals on adjacent TCNQ molecules within the stack is maximised. This corresponds to maximising the degree of ring-ring overlap, (see figure 2.2), as opposed to ring-bond overlap, (see figure 2.3).

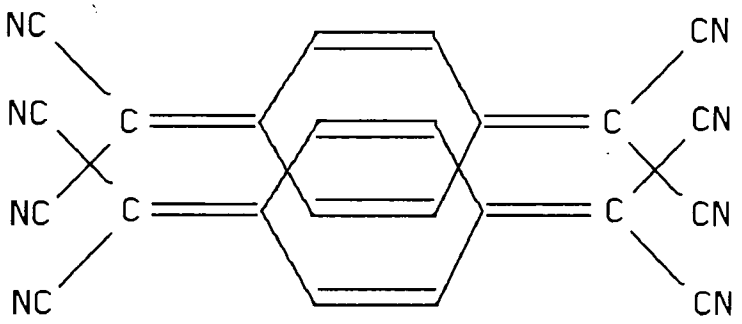

Figure 2.2 Ring-Ring overlap between adjacent TCNQ molecules

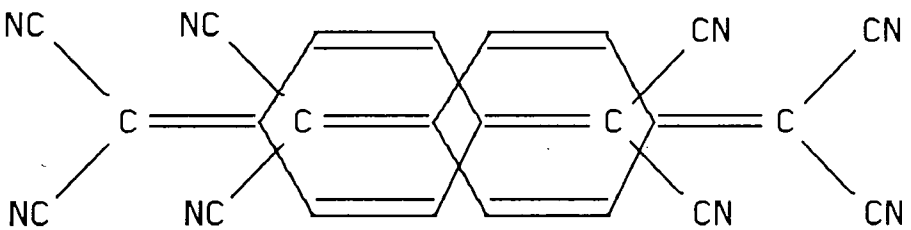

Figure 2.3 Ring-Bond overlap between adjacent TCNQ molecules

High conductivity is also favoured when neutral TCNQ is present in the TCNQ stacks (Torrance 1977). In monovalent or simple salts, where the donor to TCNQ ratio is 1:1, this can occur when charge transfer from donor to TCNQ is incomplete. Thus complexes formed by TCNQ with donors of intermediate ionisation potential, such as TTF, exhibit metallic conductivity. In such cases the average charge per TCNQ site, (ρ) is less than 1, and on a short time scale the TCNQ stack can be viewed as consisting of both $TCNQ^{-}$ and $TCNQ^{o}$. The high conductivity can be interpreted as being due to the increased ease of electron transfer from one TCNQ molecule to the next within the stack, resulting from the fact that this process no longer requires two electrons to reside on the same TCNQ

site. This avoids the large Coulomb repulsion associated with such a situation. In complex salts, where the TCNQ/donor ratio is, say, 2:1 or 3:2, the condition $\rho < 1$ arises naturally from the stoichiometry and they therefore tend to have higher conductivities than the simple salt of the same donor.

Being quasi-one-dimensional conductors the TCNQ salts are susceptible to a phase transition known as the Peierls transition, (Peierls 1955). This occurs on cooling a one-dimensional crystal lattice and manifests itself in these materials, as a distortion of the TCNQ stacks, whose structure changes from one in which the TCNQ molecules are evenly spaced, to a dimerised structure, consisting of evenly spaced pairs of molecules. Evidence for Peierls transitions comes from anomalies in the magnetic susceptibility, conductivity and from X-ray data (Endres 1983). In some salts the transition is first order, while in others it is second order. The transition results in a localisation of the charge on the molecules in the TCNQ stack. In certain salts, the transition results in a metallic to semiconducting transition e.g. TTF(TCNQ), (Epstein 1971), whilst certain salts remain semiconducting both above and below the transition (e.g. the alkali metal salts). These points will be discussed further in chapter 3.

2.3 The alkali metal salts

The alkali metal series of TCNQ salts: Li(TCNQ), Na(TCNQ), K(TCNQ) and Rb(TCNQ) were chosen as the basis for this study as they are easily synthesised, (see appendix 4), and have well documented structural and physical properties (Endres 1983). Thus they were ideal systems with which to develop techniques of dispersing TCNQ salts in polymers and to provide an indication of the potential of these salts as NLO materials.

2.3.1 Structural properties of alkali metal salts

Full X-ray structure determinations have been performed on Na(TCNQ), (Konno 1974), K(TCNQ), (Konno 1977) and Rb(TCNQ), (Shirotani 1973) though only unit cell data is available for Li(TCNQ), (Hoekstra 1972).

In the lithium, sodium and potassium salts the TCNQ radical ions form diads at room temperature where the separation between TCNQ molecules within a stack, alternates between successive sites. For instance in the case of Na(TCNQ), TCNQ separation alternates between 3.223 Å and 3.505 Å, (Konno 1974). The long axis of each TCNQ molecule in the stack, projected along the stack direction is perpendicular to those of the TCNQs in the adjacent stack, see figure 2.4.

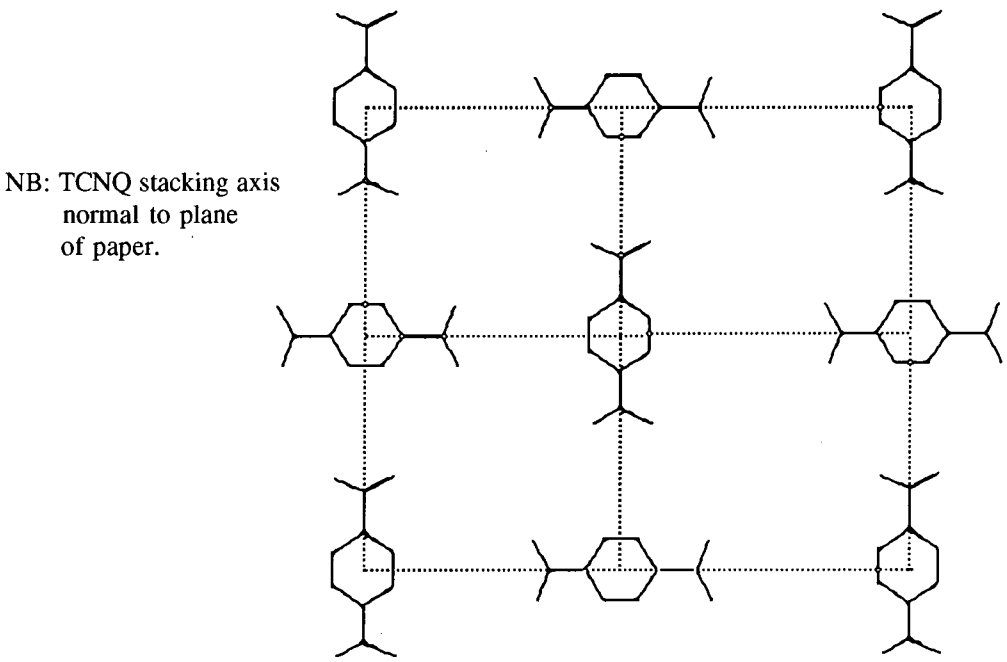

Figure 2.4 Perpendicular arrangement of TCNQ axes in adjacent stacks

Within the stacks, adjacent TCNQ species adopt a ring-ring overlap (see figure 2.2). On

heating, Na(TCNQ) and K(TCNQ), undergo a phase transition resulting in a regular stack, (e.g. for Na(TCNQ) at around 350 K, the spacing between adjacent TCNQ sites changes from the alternating values given above, to a constant 3.385 Å (Konno 1975)).

Rb(TCNQ) on the other hand, forms three polymorphs with no phase transition connecting them. Phase 1 Rb(TCNQ) has a dimerised stack at room temperature, where the long axis of each TCNQ molecule is perpendicular to that of its neighbour in the adjacent stack. The separation between successive TCNQ molecules alternates between 3.159 and 3.484 Å (Hoekstra 1972). Phase 1 Rb(TCNQ) undergoes a transition to a regular stack at around 375 K.

Phase 2 Rb(TCNQ) has a regular stack structure at room temperature, where each TCNQ long axis is parallel to that of its neighbour in the adjacent stack. The separation between successive TCNQ molecules within a stack is 3.43 Å (Shirotani 1973). Phase 2 Rb(TCNQ) undergoes a transition to a dimerised stack at around 225 K.

Both Phase 1 and Phase 2 Rb(TCNQ) are formed in normal preparation methods. Large crystals can be distinguished by means of colour - Phase 1 Rb(TCNQ) has a reddish purple colour, Phase 2 Rb(TCNQ) has a dark purple colour (Sakai 1972).

Phase 3 Rb(TCNQ) also has a regular stack with separation 3.33 Å. However this form has rarely been observed (Van Bodegom 1977)

The phase transitions in these materials have been studied by various techniques. In the case of K(TCNQ) for instance, conductivity (Afifi 1978), electron spin resonance (Blanc et al 1971), and magnetic properties (Vegter 1969), have been used to determine the transition temperature and the nature of the transition. From the behaviour of

magnetic susceptibility and X-ray measurements (Vegter 1975), the transitions are found to be first order in K(TCNQ) and Phase 1 and Phase 2 Rb(TCNQ). The dimerisation is accompanied by a doubling of the unit cell length in the stack direction. This is indicated by the abrupt disappearance of certain reflections in the X-ray spectra when passing through the transition. However the transition in Na(TCNQ) is shown to be continuous by the gradual reduction in the relevant reflection in its X-ray diffraction pattern (Vegter 1975).

2.3.2 Conductivity of alkali metal salts

All the alkali metal salts are semiconductors both above and below the transition temperature. Conductivities along the TCNQ stacking axis are typically of the order of 1-2 orders of magnitude larger than those perpendicular to the stack. Room temperature conductivities σ, and activation energies E_a, (Endres 1983) are shown in table 2.1.

Compound	σ(ohm^{-1}cm^{-1})	E_a(eV)	Reference
Li(TCNQ) (powder measurement)	5×10^{-5}	0.32	Siemons 1963
Na(TCNQ)	$1\times10^{-3}{}_a$; $3.3\times10^{-5}{}_b$	0.23-0.32	Sakai 1972
K(TCNQ)	$1\times10^{-4}{}_a$; $3.3\times10^{-6}{}_b$	0.15-0.45	Sakai 1972
Rb(TCNQ) (Phase 1)	$3.3\times10^{-6}{}_a$; $3.3\times10^{-7}{}_b$	0.44-0.53	Sakai 1972
Rb(TCNQ) (Phase 2)	$1\times10^{-2}{}_a$	0.16-0.22	Sakai 1972

a refers to conductivities parallel to the TCNQ stacks
b refers to conductivities perpendicular to the TCNQ stacks

Table 2.1 Room temperature conductivities, σ, and activation energies, E_a, of alkali metal TCNQ salts

The linear optical properties of the alkali metal salts are described in chapter 3

Chapter 3

Electronic Properties of the TCNQ Salts

3.1 Introduction

This chapter outlines the electronic properties of the TCNQ salts, with particular emphasis on the alkali metal salts. An understanding of the electronic properties is essential in explaining the optical characteristics of a material. Such an understanding is particularly important when interpreting the linear absorption spectra of the composite films described in chapter 5.

TCNQ salts exhibiting the segregated stack structure possess extended electron states along the TCNQ stacking axis. This makes electron motion along the TCNQ stacking axis much easier than in directions perpendicular to it, and gives such salts highly anisotropic electronic properties. Consequently they can often be treated to a good approximation as 1 -dimensional electronic systems.

The one-electron Hamiltonian for a linear TCNQ chain is constructed by considering the overlap of electron orbitals on neighbouring TCNQ molecules. The molecular orbitals of interest as far as understanding the properties of these materials are concerned are the partially filled π-orbitals of the TCNQ anions. In most models it is assumed that all lower lying levels are fully occupied and all higher levels are empty. This allows analysis of

charge transfer processes along the TCNQ stack but does not allow analysis of local excitations where electrons are promoted to higher levels on the same molecule. To do this one must include higher energy levels of the TCNQ molecule in the analysis.

In the TCNQ salts exhibiting the segregated stack structure, (such as the alkali metal salts), planar stacks of TCNQ ions exist with interplanar distances, $b \geq 3$ Å, however the distance between adjacent stacks is two or three times larger than this. This fact, together with the highly directional nature of the π-orbitals, leads to the overlap integral between the π-orbitals of neighbouring $(TCNQ)^-$ anions within the stack, $t_{\parallel}$, being much larger than that between the π-orbitals of $(TCNQ)^-$ anions in neighbouring stacks, $t_{\perp}$. The relatively large value of $t_{\parallel}$ causes the energy level associated with it to spread, producing an essentially one-dimensional band structure. Thus $t_{\parallel}$ is of great importance in describing the transport properties of electrons in these materials. It is subsequently referred to simply as t.

3.2 Band structure with uncorrelated electrons

For a single stack of $(TCNQ)^-$ anions, the overlap between electronic wavefunctions on neighbouring TCNQ molecules is small enough that a tight-binding approximation, (Mott 1974) can be used in describing electron transport properties. The one-electron wavefunction (see equation 3.1), can then be described by a superposition of the lowest unoccupied level of the isolated TCNQ molecule, $\Phi\pi(r)$, of all molecules in the stack, multiplied by a term e^{ikmb} which ensures the function as whole, has the correct translational symmetry (Schulz 1979, Harrison 1970).

$$\psi_k(r) = M^{-1/2} \sum_m e^{ikmb} \Phi_\pi(r - mb) \qquad (3.1)$$

Where M is the number molecules in a chain, b, is the separation of the TCNQ molecules, and Φ_π(r-mb) is the π molecular orbital at the mth site.

The energy of an electron in the conduction band is then determined by

$$\varepsilon_k = \int \psi_k^* H \psi_k dr \qquad (3.2)$$

$\Phi_\pi(r)$ falls off rapidly with r, so the only terms of significance in 3.2 are those involving orbitals associated with the same molecule or nearest neighbour molecules. The former term is simply E_α, the energy of the electron on an isolated TCNQ molecule. The latter terms combine to give a contribution

$$E_\beta = -2t \cos kb \qquad (3.3)$$

where $$t = -\int \Phi_\pi^*(r \pm b) H \Phi_\pi(r) dr \qquad (3.4)$$

is the transfer or overlap integral.

Thus neglecting electron correlations, $E_\alpha + E_\beta$ represents the energy of a conduction electron. It is often convenient to choose the zero of energy as being at the k=0 point. In this case the relation between conduction band energy E_k and k, is written as

$$E_k = 2t(1 - \cos kb) \qquad (3.5)$$

This relationship is plotted in figure 3.1. The Fermi energy and wavevector, for a half filled band (one-electron per TCNQ molecule), as found in the alkali metal salts are indicated. The bandwidth is seen to be equal to 4t.

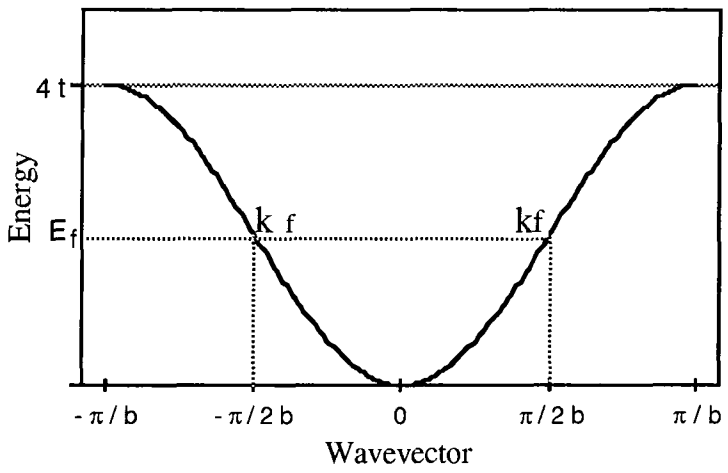

Figure 3.1 E_k versus wavevector, k, for a half filled 1-dimensional conduction band

3.2.1 The Peierls gap

The Peierls transition, a characteristic of one-dimensional electronic systems, was first predicted theoretically by Peierls, (Peierls 1955). At the Peierls transition temperature, a periodic lattice distortion develops with wave number $2k_f$ where $k_f=\pi n/2b$, is the Fermi wavevector of the undistorted lattice, and n and b are the number of electrons per unit cell and the undistorted lattice constant, respectively. This distortion produces a new lattice, consisting of TCNQ dimers, with a lattice constant of $2\pi/2k_f$, and therefore with a Brillouin zone of width $2k_f$. The total number of electrons to be accommodated remains the same, so the Fermi wave number remains k_f. Hence the effect of the distortion is to introduce a band gap at the Fermi energy. Electrons undergo a decrease in kinetic energy due to the downward bending of the energy wavevector dispersion curve near the gap.

Some of this energy is taken up by the lattice as it undergoes the distortion, (see figure 3.2).

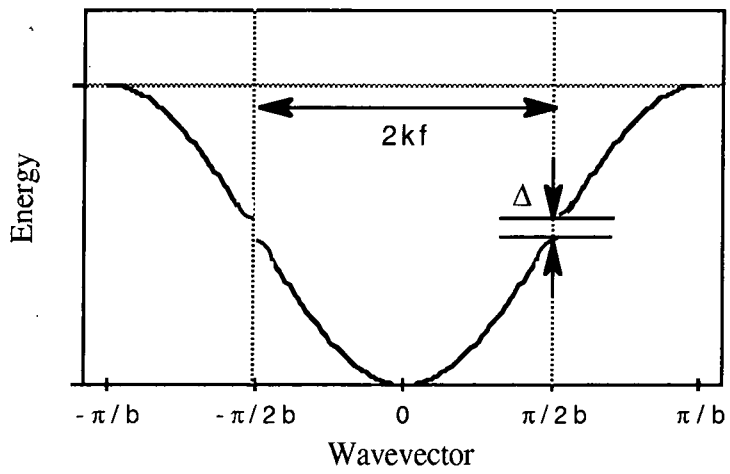

Figure 3.2 The Peierls gap in a 1-Dimensional lattice

The Peierls phase transition is often accompanied by a high conductivity to low conductivity transition due to formation of the energy gap. X-ray analysis can be used to detect the lattice distortion associated with the transition (Terauchi 1978).

3.3 Band structure with correlated electrons

The discussion above has considered an idealised system, in particular it took no account of electron-electron correlations. Electron motion along the TCNQ stack leads to double occupancy of TCNQ sites. This involves an increase in the potential energy of the electron U, equal to the repulsion between two electrons when on the same TCNQ site. In addition the Coulomb repulsion energy between electrons on neighbouring TCNQ sites, V, can influence the electronic properties.

The importance of electron correlations varies greatly with ρ, the average number of conduction electrons per TCNQ molecule. It has been found, (Mazumdar and Bloch, 1983), that correlations are important for ρ=1, i.e. the half filled band, (this is the case in the alkali metal salts) as well as for ρ close to 0.5. Both on-site and near neighbour Coulomb repulsion energies were considered in calculating the energy for electron transfer between neighbouring TCNQ molecules. All longer range Coulomb interactions were neglected due to the completeness of screening of such forces.

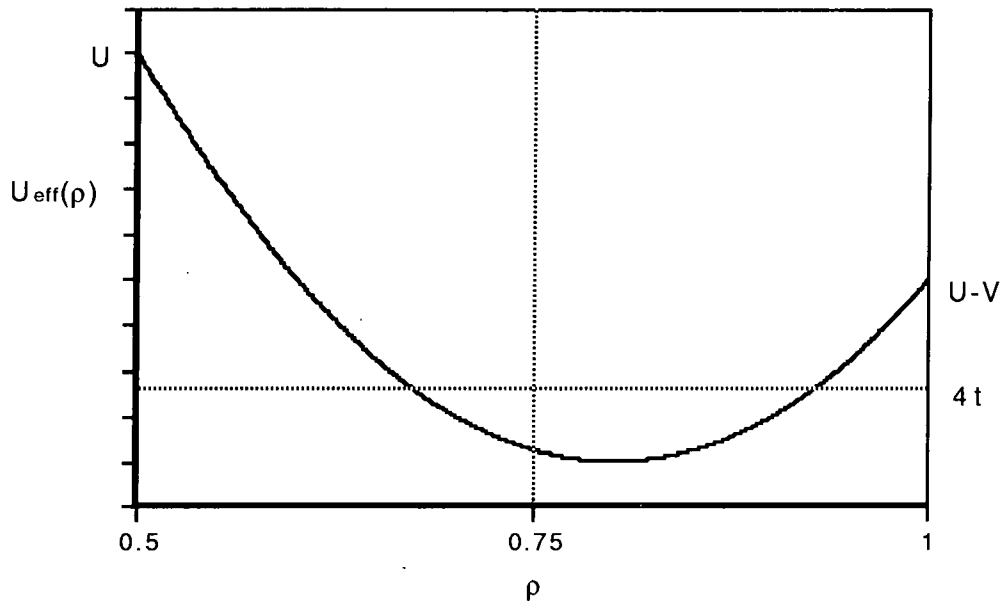

Figure 3.3 Schematic behaviour of Ueff versus ρ for a single TCNQ chain, (Mazumdar and Bloch, 1983)

For ρ=1 there is on average 1 electron on each TCNQ site. The transfer of an electron from one $(TCNQ)^-$ to another requires an energy $U_{eff}=U-V$. If however an electron is eliminated from site i, the transition from i+2 to i+1 will involve a lower energy U-2V. As ρ decreases, (corresponding to electrons being removed from further TCNQ sites), the

relative weight of such lower energy transitions increases, until at ρ=0.75 the value of U_{eff} reaches a minimum. The relative weight of these transitions now decreases until it vanishes at ρ=0.5 where only second neighbour sites are occupied and U_{eff} = U, see figure 3.3.

The Hubbard model (Hubbard 1965) has had considerable success in describing one-dimensional electron systems where electron/electron correlations are significant. The key parameters in the model are the on-site Coulomb repulsion U, the transfer integral t and the number of conduction electrons per TCNQ molecule, ρ. Owing to screening mechanisms such as polarisation of the environment, which reduces the effect of long range Coulomb interactions, only repulsions between electrons on the same site are normally included. The model can be extended to include Coulomb interaction between electrons on nearest neighbour sites leading to the extended Hubbard model.

The Hubbard Hamiltonian can be written as, (Hubbard 1964):

$$H_H = -t\sum_{n,\sigma}\left(a^{\dagger}_{n,\sigma}\, a_{n+1,\sigma} + a^{\dagger}_{n+1,\sigma}\, a_{n,\sigma}\right) + U\sum_{n} n_{n\sigma}\, n_{n\sigma'} \qquad (3.6)$$

where $a_{n,\sigma}$ and $a^{\dagger}_{n,\sigma}$ are operators that annihilate and create an electron with spin σ, at site n respectively and $n_{n\sigma}$ is given by

$$n_{n\sigma} = a^{\dagger}_{n,\sigma} a_{n,\sigma} \qquad (3.7)$$

The first term in 3.6 represents the band motion of the electrons, the second term represents the energy due to the Coulomb interaction.

The extended Hamiltonian which includes nearest neighbour interactions can be written as, (Hubbard 1964).

$$H_{EH} = H_H + V\sum_{n,\sigma,\sigma'} n_{n,\sigma} n_{n+1,\sigma'} \qquad (3.8)$$

where V is the Coulomb repulsion between electrons on nearest-neighbour sites and $n_{n\sigma}$ is given by equation 3.7.

The effect of the correlation terms on the electronic properties of a one-dimensional system depends on their relative strength. In particular, the relative size of the Coulomb repulsion energies in comparison to the bandwidth 4t is of fundamental importance. To illustrate this, two cases are considered below. The first represents the extreme case where Coulomb correlations are so large that in comparison, the bandwidth, 4t is negligible. The second case considered, (which is applicable to the alkali metal TCNQ salts), is one where U and V remain large, but where 4t is of significant size.

Case (i): $U,V > 0, t = 0$

In this case, the zero value of t leads to the electrons behaving like classical particles, being localisable with no increase in energy. A distribution termed the generalised Wigner lattice is assumed by the electrons which minimises the Coulomb repulsion energy of the electrons. The form of the Wigner lattice depends on the average number of electrons ρ, per TCNQ site. The problem is the one-dimensional analogue of determining the configuration taken up by a low density electron gas (Wigner 1938). The problem is essentially how to distribute ρN electrons over 2N orbitals along a chain consisting of N TCNQ molecules, so as to minimise the total energy.

For $\rho < 1$, double occupancy can be avoided and the problem reduces to minimising

$$H = \sum_{i \neq j} V_{i-j} n_i n_j \qquad (3.9)$$

subject to the constraint

$$\rho N = \sum_i n_i \qquad (3.10)$$

where n_i is the occupancy of site i, with $n_i = 0$ or 1, and V_{i-j} is the Coulomb repulsion

between electrons on sites i and j.

No solution is known for arbitrary V_X, but for V_X satisfying

$$V_x \to 0 \qquad \text{as} \qquad n \to \infty \tag{3.11}$$

and

$$V_{x+1} + V_{x-1} \geq 2V_x \qquad \text{for all} \qquad n > 1 \tag{3.12}$$

exact solutions can be found. The distributions calculated using this approach are ground state distributions. At finite temperature, total long range order is not allowed. A typical configuration has regions of the appropriate Wigner lattice separated by faults.

For instance, with a value of ρ=0.6, the distribution shown in figure 3.4 is predicted, where single TCNQ- ions (monomers) and pairs of $(TCNQ)^-$ ions (dimers) surround neutral TCNQ molecules, Hubbard(1978).

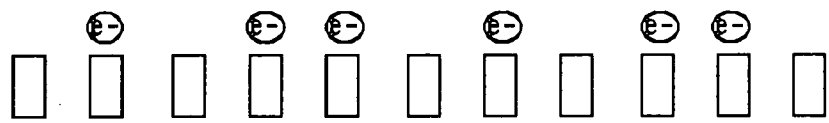

Figure 3.4 Wigner Lattice for $\rho = 0.6$

In general, the resulting electron arrangement within a period is non-uniform giving rise to electric fields capable of distorting the lattice due to repulsion of electrons on neighbouring sites.

Inclusion of small, but finite t in the model, introduces the effect of band motion into the system. This gives rise to so called virtual states where electrons are able to undergo transitions which lead to configurations other than the minimum energy configurations calculated assuming t=0. This makes the terms neutral, monomer, and dimer redundant as transitions in which say a dimer site changes into a monomer site are so fast that it destroys the distinction between them.

Case (ii) : $U>>4t > 0$

In the case where $U>>4t$ but where 4t is non-zero, a one-dimensional conduction band is formed as described in section 3.2. However in contrast to the uncorrelated electron case, no two electrons can reside on the same TCNQ site, regardless of spin due to the large Coulomb repulsion energy which would result. In the ground state each particle must go into a different spatial state. The conduction band splits into a band of singly occupied states at lower energy, and a band of doubly occupied states separated at k=0 by an energy of approximately U (Ovchinnikov 1970, Musurkin 1970), (see figure 3.5). This shifts the Fermi wave vector to twice its value for the independent electron case i.e. to the Brillouin zone edge. Thus in salts with a single electron per TCNQ site, the presence of a strong Coulomb interaction is expected to make such materials semiconductors, both above and below the Peierls phase transition (Conwell 1988). In this state the Peierls instability occurs for a wavenumber $4k_f$, where k_f is the Fermi wave-vector for the uncorrelated electron case.

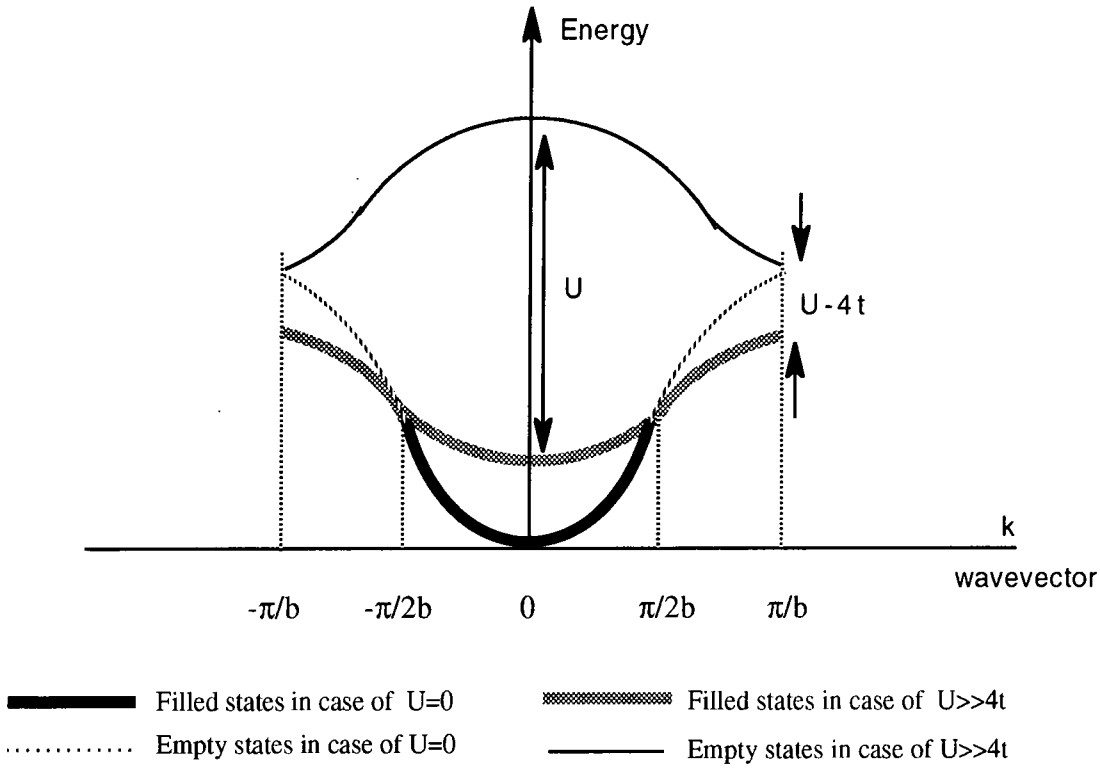

Figure 3.5 Band structures for U=0, and for large U

Various experimental and theoretical approaches have been used to determine ρ, 4t, U and V in the TCNQ salts. In the case of the alkali metal salts ρ has been determined to be 1, using infra-red absorption spectroscopy (Chappell 1981); values for the bandwidth 4t, in the alkali metal salts have been determined from magnetic susceptibility data (Vegter 1971) to be in the range 0.2-0.35 eV; an upper limit to U has been determined by Jonkman et al (1972), using molecular orbital calculations to determine the energy change for the transition

$$TCNQ^{-} + TCNQ^{-} \longrightarrow TCNQ^{0} + TCNQ^{2-}. \qquad (3.13)$$

Their calculations yield a value of U = 3.5 eV. Similar calculations by Tanaka (1976)

yielded unscreened values of U = 3.95 eV and V = 2.29 eV.

The Coulomb repulsion energy U, has also been estimated by Torrance (1979) through

$$U = \frac{e^2}{4\pi\varepsilon_0 d} \tag{3.14}$$

where d is the on-site charge separation estimated as 3-4 Å giving a value of U=3-4 eV. For two electrons on neighbouring TCNQ molecules, separated by an interplanar distance 3.3 Å the relevant value of d is 9 Å leading to a value of V=1.6 eV .

Due to the screening effects of other electrons in the solid state, the actual values of U and V are expected to be substantially smaller than this. Nevertheless measurements of the dielectric function in the optical region (Khanna et al 1974), suggest that in these materials a strong electron-electron Coulomb interaction is present. Yakushi (1979) used optical reflectivity measurements to determine screened values of U (1.4 eV), V (0.3 eV) and 4t (0.3 eV) in K(TCNQ). Thus in the alkali metal salts, the split band model, (case (ii) in the discussion above), is expected to apply. This explains why the alkali metal salts are semiconductors both above and below the Peierls phase transition.

3.4 Optical properties of TCNQ salts

Of great interest to the present work are the optical properties of the TCNQ salts. In the visible wavelength region they exhibit local excitation bands associated with promotion of electrons to higher energy levels on the same TCNQ molecule, and charge transfer excitations associated with transfer of electrons between neighbouring TCNQ molecules within a stack. The anisotropy of these salts is reflected in the optical properties they

exhibit which are strongly polarisation dependent. As in the case of conduction properties, the key parameters in determining the optical properties of the TCNQ salts associated with charge transfer excitations are the on-site and off- site Coulomb repulsion energies, U and V, the degree of charge transfer, ρ and the transfer integral, t.

3.4.1 Optical properties of a system of isolated dimers

A number of theoretical approaches have been used to analyse the optical properties of the TCNQ salts. Insight into the properties of large assemblies of molecules such as are found in a real crystal can be obtained by considering the simpler system of a dimer (Bozio and Pecile 1991). For a system of dimers, with one-electron per dimer (and hence no need to consider electron correlations), a single charge transfer transition is predicted with frequency given by equation 3.15

$$\omega_{CT} = \frac{2t}{\hbar} \tag{3.15}$$

and with oscillator strength

$$f_{CT} = \frac{m_e t b^2}{\hbar^2} \tag{3.16}$$

where, m_e is the electron effective mass and, as before, t is the overlap integral and b is the separation of the two molecules.

For the case where there are two electrons per dimer, it is necessary to include in the Hamiltonian a term proportional to the on-site Coulomb potential. Harris and Lange (1967) developed such a model which is effectively the Hubbard model for dimers. The energy

level diagram which is derived from this model is shown in figure 3.6.

The only allowed transition from the ground state is that indicated, with predicted transition frequency given by equation 3.17.

$$\omega_{CT} = \frac{1}{2\hbar}\left[U + \left(U^2 + 16t^2\right)^{\frac{1}{2}}\right] \tag{3.17}$$

and oscillator strength given by

$$f_{CT} = \frac{m_e t b^2}{\hbar^2\left[1 + \left(\frac{U}{4t}\right)^2\right]^{1/2}} \tag{3.18}$$

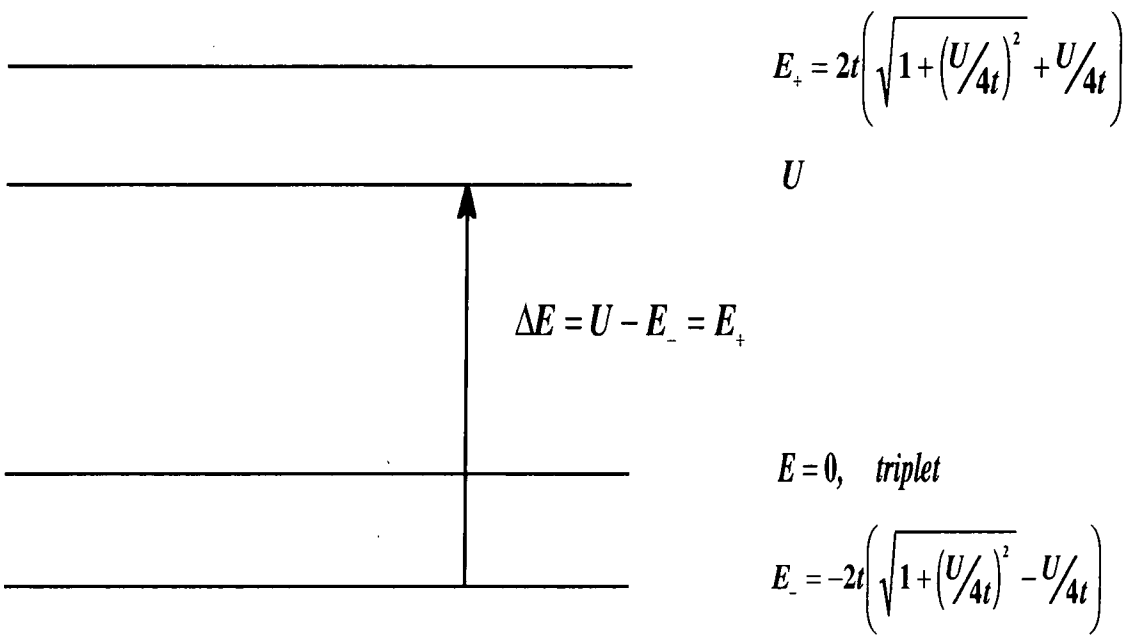

Figure 3.6 Energy level diagram for doubly charged dimer

Clearly according to equations 3.17 and 3.18, as the on-site Coulomb repulsion increases

in comparison to 4t, the charge transfer absorption shifts to *higher energy* , and the oscillator strength is expected to *decrease.*

For certain TCNQ salts the TCNQ molecules arrange themselves as quasi isolated dimers (e.g. Trimethylbenzimidazolium(TCNQ), Goldberg (1977)), and it is possible to fit the above results to experimentally measured absorption spectra, (Rice 1979). When this is not the case the analysis must be extended.

3.4.2 Optical properties of extended one-dimensional systems

When attempts are made to extend the above dimer model to chains of dimers as are encountered in real crystals, the complexity of the problem increases markedly. It is now necessary to adopt the extended Hamiltonian described earlier, which takes into account the nearest neighbour Coulomb interaction. For a half-filled band, (such as occurs in the alkali metal salts), with U much greater than 4t, an energy gap of U-4t is predicted, as shown in figure 3.5, (Ovcinnikov 1970), suggesting the onset of optical absorption at

$$\omega = \frac{(U - 4t)}{\hbar} \qquad (3.19)$$

Lyo and Gallinar (1977), predicted an optical absorption extending between U-4t and U+4t, i.e. over twice the one-electron bandwidth, and an oscillator strength proportional to t^2/U in the small t limit. Again the charge transfer band was predicted to shift to higher energy with higher on-site Coulomb repulsion, (due for example to decreased electron screening) or with reduced degree of electron orbital overlap.

The models described so far have included only the lowest lying orbital of the unpaired electron associated with $(TCNQ)^-$. Such models are able to describe the charge transfer transition between TCNQ sites only. They cannot however describe the higher energy electronic transitions which arise mainly from local excitations of the $(TCNQ)^-$ anion. To be able to describe such transitions it is necessary to include some of the higher energy molecular orbitals associated with the $(TCNQ)^-$ anion. Tanaka (1976) used the molecular orbital calculation for the $(TCNQ)^-$ ion (Lowitz 1967) to consider the intermolecular and intramolecular interactions of $(TCNQ)^-$ ions in a stack. A product of the molecular orbitals of $(TCNQ)^-$ was considered in conjunction with an extended Hubbard type Hamiltonian. It was possible to calculate with good agreement to experiment the position and oscillator strengths of the charge transfer band and of the lowest energy local excitation of the $(TCNQ)^-$ ion in the solid state of a number of TCNQ salts.

3.4.3 Experimental studies

Since the work described in the following chapters deals exclusively with the alkali metal salts, only work relating to these materials will be described here. Several studies of the optical properties of the alkali metal TCNQ salts have been performed using dispersions of the salt in KBr discs (Torrance 1975). Such studies enable determination of the positions of absorption bands. More sophisticated measurements such as near-normal incidence reflectance measurements Iida (1968) and Oohashi (1973), or single crystal transmission measurements such as those of Tanaka (1976), allow in addition, determination of the oscillator strength of the absorption, and polarisation dependence.

Common to all of the alkali metal salts are three absorption bands. The two higher energy

bands are assigned to local excitations confined to $(TCNQ)^-$ ions in which an electron is promoted to a higher level on the same molecule. The higher energy band is labelled LE2 (generally around 360 nm) the lower energy band is labelled LE1 (around 610 nm). In addition a lower energy absorption band which generally occurs around 1100 nm, is also observed. It is found that this low energy band is much stronger in absorption spectra measured with the incident light polarised parallel to the TCNQ stacking axis. This band is therefore assigned to a charge transfer process between neighbouring $(TCNQ)^-$ ions, within a stack (Hiroma 1971).

The dimerised structure of the TCNQ stacks in the alkali metal salts, suggests that their absorption spectra should bear some resemblance to that of $(TCNQ)^-$ dimers in solution. This spectrum was measured by Boyd (1965). The two spectra are indeed very similar though the LE bands in the dimer are at slightly higher energy whilst the CT band is at slightly lower energy. This latter effect may be due to increased screening in the crystal state, (Jacobsen 1988).

Iida (1977), applied Hubbard theory to the charge transfer absorption spectra of K(TCNQ). The analysis predicted that the charge transfer peak would occur at energy U, the effective on-site Coulomb repulsion energy. Further, the shape of this peak was predicted to be asymmetric with very little absorption on the low energy side of the peak. This however was found not to be the case. The charge transfer peak was in fact symmetrical. The discrepancies were thought to be due, in part, to neglect of vibronic effects of the TCNQ molecules.

Tanner (1977) noted a splitting of the CT band in K(TCNQ) into a strong, long wavelength feature and a much weaker absorption at slightly higher energy. The two bands become more distinct at low energies. The origin of this higher energy band remains controversial

and has been variously assigned to a monomer transition by Tanner himself, to a transition between dimers as opposed to within a dimer by Jacobsen (1988) and to a splitting of the CT band due to near neighbour interaction by Yakushi (1979)

Oohashi (1973), investigated the optical properties of the alkali metal salts in compressed pellet form using reflection measurements. The position of the absorption peaks and the oscillator strengths for each transition are given in table 3.1.

Cation	Peak Position (eV)			Oscillator strength		
	CT1	LE1	LE2	CT1	LE1	LE2
Li	1.22	2.01	3.30	0.26	0.25	0.56
Na	1.36	2.05	3.43	0.25	0.41	1.0
K	1.18	1.98	3.43	0.36	0.27	0.62
Rb-I	1.22	1.95	3.36	0.31	0.23	0.56
Rb-II	0.88	2.07	3.48	0.39	0.33	1.5

Table 3.1 Peak position and oscillator strength of alkali metal salt absorption bands (Y. Oohashi 1973)

It is apparent that both the CT band and the LE bands are sensitive to cation type. The difference in the strength of CT band in Phase 1 Rb(TCNQ) and Phase II Rb(TCNQ) was interpreted as being due to the regular TCNQ stack, present in Phase II Rb(TCNQ), producing significant overlap of electron orbitals associated with two near neighbour TCNQ molecules. In the case of Phase I Rb(TCNQ) the dimerised structure leads to a significant reduction in orbital overlap with the more distant neighbour. The reduced degree of electron delocalisation in the dimerised structure of Phase 1 Rb(TCNQ) is thought to

lead to the high energy position of the CT band in this salt. The reason for the greatly enhanced value of the oscillator strength of the LE2 band in Phase II Rb(TCNQ) is not known

Chapter 4

Formation of Composite Films

4.1 Basic technique of composite formation

This chapter describes the methods used to form composite films consisting of microcrystals of the alkali metal salts of TCNQ within a host polymer matrix. When forming composite films, the aim is to produce an homogeneous distribution of microcrystals of as uniform a size and shape as possible. The methods employed in the present work involve inducing microcrystal formation, in-situ, within a film initially containing the salt ionically dispersed as a solid solution. The following sections outline the three key stages in composite formation

4.2 Solution formation

The polymer and salt of which the composite is to be made are dissolved in a common solvent. The host polymer chosen, poly(methyl methacrylate), (PMMA) is soluble in a wide range of solvents whereas the salts of TCNQ tend to have fewer good solvents. Thus it is the salt solubility which determines which solvents are used in forming the initial solution. For the alkali metal salts dimethylformamide, (DMF), was found to be the best solvent. DMF is non-volatile (boiling point 152 C), and consequently the spin coating

method (see appendix 2) is the most suitable for film formation with this solvent. The alkali metal salts are also moderately soluble in acetone and acetonitrile. Being more volatile, withdrawal from solution (see appendix 2), must be used to form films when using these solvents.

It is desirable to maximise the weight fraction, W of salt in the final polymer film. This is obviously limited by the solubility of the salt, which imposes a maximum concentration of salt $[C_S]_{max}$, that can be achieved in the solvent (e.g. 10 mg/cm^3 for K(TCNQ) in DMF). W also depends indirectly on the required thickness of the final film as, for any required film thickness T, a minimum polymer concentration, $[C_p]_{min}$, is necessary to produce sufficient viscosity in the parent solution, to enable this thickness to be attained. $[C_p]_{min}$ depends on the method of film formation employed (either withdrawal or spin coating). The ratio $[C_S]_{max}/[C_p]_{min}$ gives an upper limit to the weight fraction of salt which can be achieved for a film of a thickness T. In practise this doping level cannot usually be attained, since for high salt concentrations approaching $[C_S]_{max}$, premature phase separation occurs as the film dries, (see below), and control over the microcrystal morphology is lost. Methods of avoiding this are given in the next section.

4.3 Film formation

A film of the solution (typically 10 μm in thickness), is deposited onto a suitable substrate by either a spin coating or substrate withdrawal method, (see appendix 2). The film consists of three phases: polymer, salt and solvent. As solvent evaporation proceeds, the

concentrations of salt and polymer increase. The increasing polymer concentration leads to an increasing film viscosity which inhibits salt crystallisation. The increasing salt concentration leads to solution saturation which encourages crystallisation. Thus a competition exists between these two tendencies. If the required microcrystal free, solid solution is to be obtained, it is important that crystallisation is prevented in the drying film. Should this occur, the treatment conditions must be adjusted to further inhibit the crystallisation process during the drying of the film. This can be achieved by adding more polymer to the solution, thus increasing the solution viscosity, (also however reducing the weight fraction of salt in the final film). Alternatively one can promote rapid drying using reduced pressure and/or heating the drying film. This accelerates drying, reducing the time period during which the components of the salt in the film are mobile, hence inhibiting premature crystallisation.

4.4 Film treatment

The salt in the dried film is in a supersaturated, non-equilibrium state. However the lack of mobility of the salt ions in the film prevents crystallisation. A treatment is now applied which re-introduces mobility to the ions within the film. Application of heat, or vapour swelling may be used. If high mobility is maintained for long enough, it allows diffusion of the salt ions to take place and following their association microcrystal formation occurs. The nature and conditions of treatment can be varied to control the size of the crystallites in the final film.

4.4.1 Vapour treatment

This involves exposure of a film containing molecularly dispersed salt to the vapour of a solvent of the host polymer, under controlled conditions. During vapour treatment, vapour is absorbed by the film, which swells and softens. The presence of the infused solvent gives the salt ions the necessary mobility to induce salt crystallisation (Jeszka 1985).

The treatment is carried out in a vessel shown in figure 4.1. It consists of two chambers connected by a valve. Each chamber can be separately evacuated. One chamber contains the solvent with which the film is to be treated, the other chamber holds the sample. The vapour pressure in chamber B is monitored using a pressure gauge.

In a typical treatment, with valve C closed the solvent chamber is first connected to a rotary vacuum pump until the air has been expelled from the chamber. Valve A is then closed.

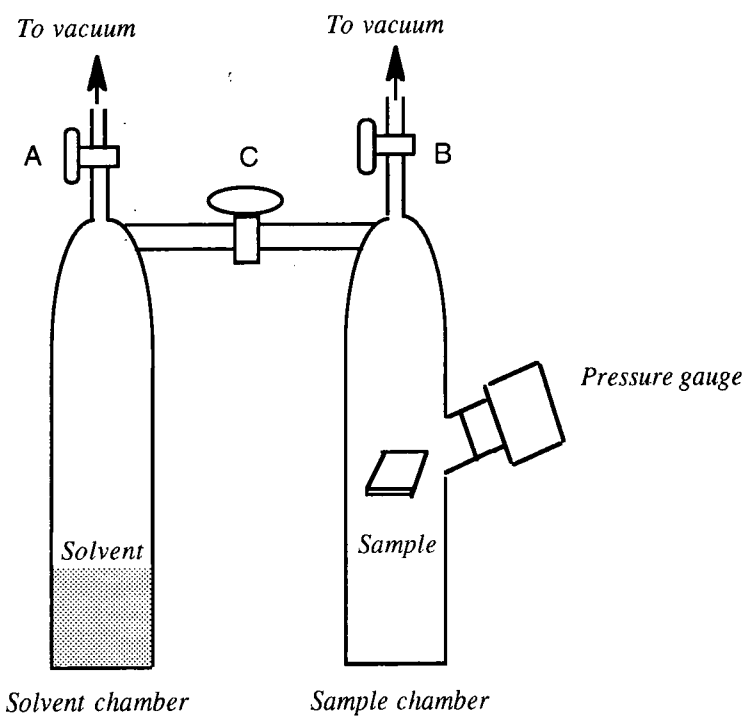

Figure 4.1 Vapour treatment vessel

With valve C still closed, the sample chamber is evacuated to around 1mb. Valve B is then closed. Valve C is now opened, allowing solvent to enter the sample chamber until the vapour pressure inside it reaches the chosen value. Valve C is then closed. Conversion begins and is allowed to proceed until it is complete. The period required to attain the maximum degree of conversion can be determined by measuring the visible absorption spectrum following various treatment periods. When full conversion is attained spectral features typical of TCNQ- ions present in the untreated film are no longer present (see chapter 5). The sample is then removed.

The key factors affecting the size and shape of crystallites in the vapour treated film were found to be:

i) Choice of solvent vapour:

For conversion to occur, the polymer component of the film must be soluble in the solvent vapour used in the treatment. The solvent vapour can then infuse the film and cause it to soften. It is however possible to choose to what extent the treatment solvent is an effective solvent of the salt .

For treatment solvents in which the salt is insoluble, (e.g. dichloromethane in the case of the alkali metal TCNQ salts), conversion from a molecularly dispersed to microcrystalline phase is very efficient and can be 100%, (see chapter 5, section 5.1.1). Depending on other treatment conditions, a range of crystallite sizes is obtainable with largest dimension ranging from 100 μm to sub-optical (i.e. certainly less than 0.5 μm). In films where the microcrystals are of sufficient size to be visible under an optical microscope, they are of fairly uniform size and homogeneously dispersed throughout the film, see figure 4.4

For solvents in which the salt has intermediate solubility (e.g. acetone in the case of the alkali metal TCNQ salts), conversion tends to be less efficient. Crystals produced tend to be of a larger size than those produced under similar conditions using poorer solvents of the salt as treatment vapour.

For solvents in which the salts have high solubility, (e.g. acetonitrile or DMF) conversion tends to be incomplete and crystals formed tend to be of larger dimension. Figure 4.2 shows an optical micrograph of a Li(TCNQ) doped film which had been thoroughly dried and treated with acetonitrile. It contains predominantly needle shaped crystals of around 5 μm in length.

ii) Degree of pre-vapour treatment drying:

After a film has been formed, but prior to vapour treatment, the film is dried under vacuum to expel solvent. It is found that if films are dried for a short period of time, (1-2 minutes), so that a significant amount of solvent from the original solution remains in the film, subsequent vapour treatment of the film leads to crystals of a large size (>10 μm diameter). If drying is prolonged for a number of hours much smaller crystals are obtained following vapour treatment.

Figure 4.3 shows an optical micrograph of a K(TCNQ) doped film which had been dried under vacuum at 40 C for three minutes and which thus retained a significant amount of the solvent used in the parent solution (DMF). It was treated with dichloromethane at a pressure of 300 mb for 1 minute. It contains mainly large (approximately 5 μm diameter) crystals of fairly uniform shape.

iii) Vapour Pressure:

The vapour pressure of the solvent in the treatment vessel is an important parameter in the

control of crystal size. Varying this parameter as a means of controlling crystallite size has the advantage that it is a continuously variable parameter in contrast to, for example, the solubility of the salt in the solvent used during vapour treatment. This presents the possibility of a finer control over the treatment conditions and thus crystallite size. Four distinct pressure regimes can be identified according to the resulting crystallite size. With dichloromethane vapour, at low pressures (<150 mb), conversion either does not occur at all or at best is partial and takes place very slowly (tens of hours). At slightly higher pressures (150-250 mb) conversion takes place on a scale of a few tens of minutes

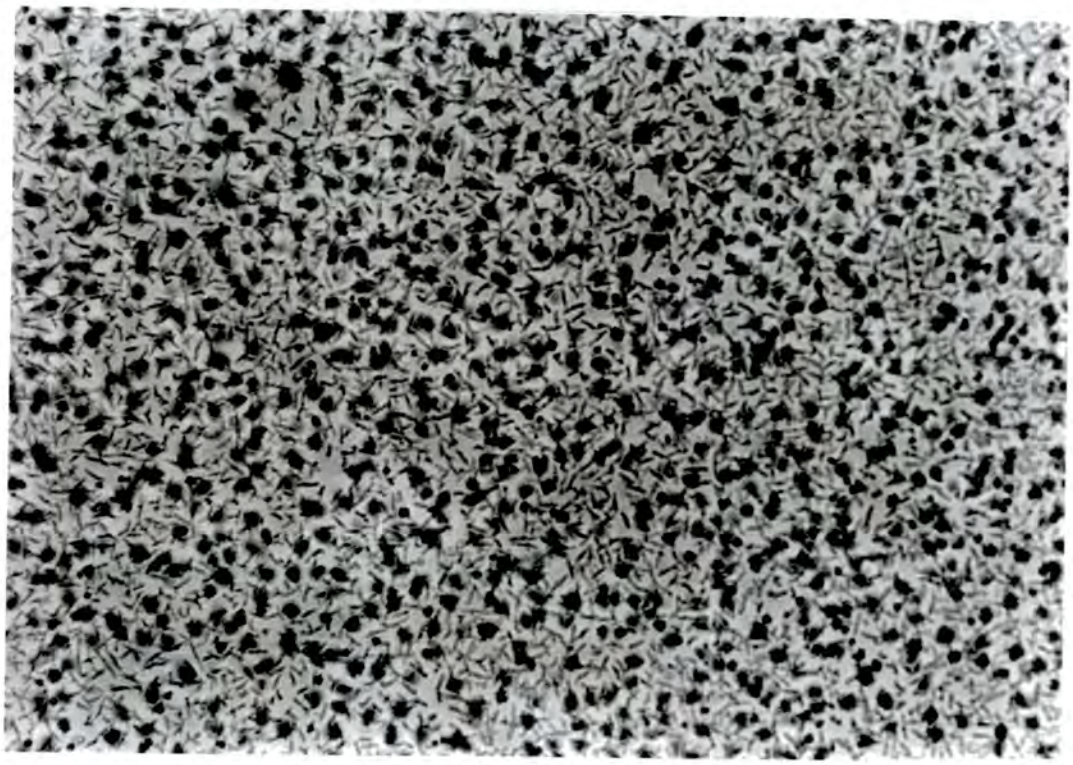

Figure 4.2 Optical micrograph of Li(TCNQ) doped film following vapour treatment with acetonitrile (Dried 1 hr ; 200 mb, 5 mins)

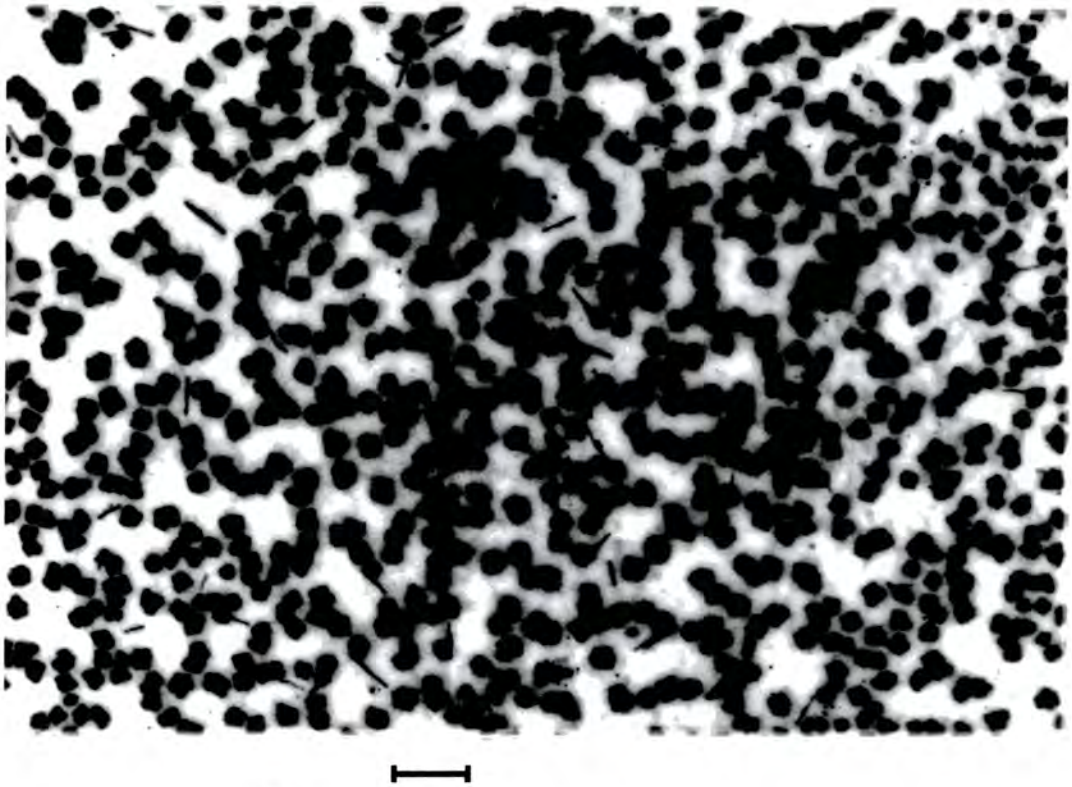

Figure 4.3 Optical micrograph of K(TCNQ) doped film following vapour treatment with dichloromethane. (Dried 3 mins; 300 mb, 1 min.)

and leads to larger crystals. At moderate pressures (250-350 mb), crystallite size reaches a minimum and conversion times decrease, (typically < 1 minute). At high pressures (>400 mb), larger crystals are again obtained as in treatments at low pressures although conversion is more rapid (a few seconds) .

Figure 4.4 shows an optical micrograph of a K(TCNQ) doped film which had been thoroughly dried and treated with dichloromethane at a pressure of 185 mb for 5 minutes. Crystals of around 1-2 μm diameter and which seemed to possess a cross-like shape were produced. Treatment of a similar film with dichloromethane vapour at a pressure 300 mb for 1minute resulted in a film containing suboptical crystals. Figure 4.5 shows an optical micrograph of a K(TCNQ) doped film which had been thoroughly dried and treated with dichloromethane at a pressure of 450 mb for twenty seconds. Crystalline phase is visible but is of indeterminate shape.

iv) Period of post-conversion vapour exposure :

Once a film has been fully converted it is usually removed immediately. However, if a film containing sub-optical crystals is left exposed to solvent vapour for a prolonged period, after conversion has been completed, large crystals of micron dimension are found in the final film. It seems that the distribution of smaller crystallites converts to a distribution of larger crystals i.e. transport of material between the microcrystals takes place so that larger crystals grow at the expense of smaller ones.

Summarising, the smallest crystals are obtained by vapour treating a thoroughly dried film using a non-solvent of the salt and employing moderate vapour pressure, (~300 mb in the case of dichloromethane). The film should removed promptly on completion of conversion. Crystals formed in this way are of a size too small to be visible under an optical microscope (i.e. < 0.5 μm).

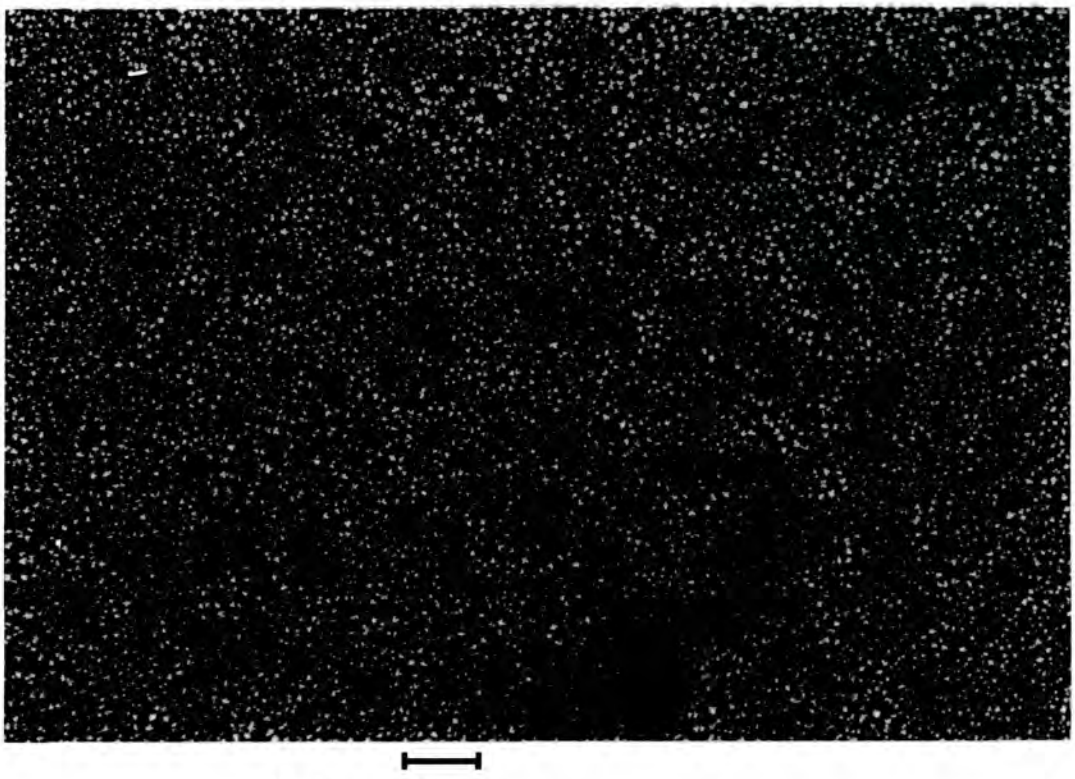

Figure 4.4 Optical micrograph of K(TCNQ) doped film following vapour treatment with dichloromethane (Dried 3 hr ; 185 mb, 5 mins)

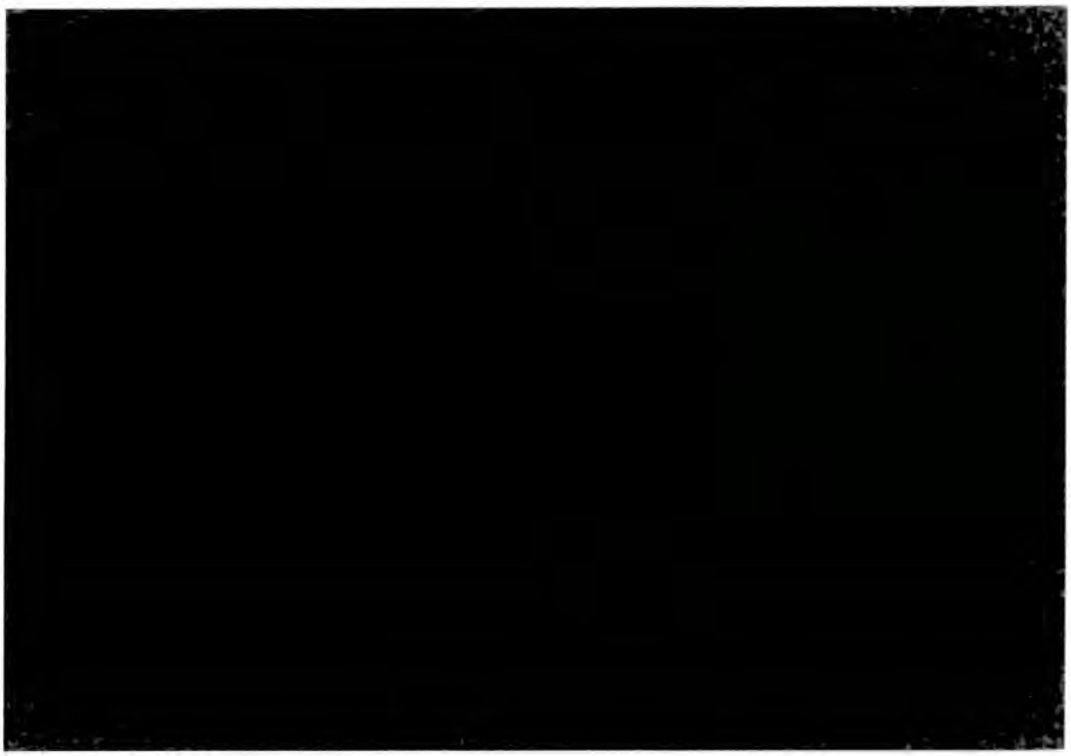

Scale: 10μm

Figure 4.5 Optical micrograph of K(TCNQ) doped film following vapour treatment with dichloromethane. (Dried 3 hrs; 450 mb, 20 s.)

To produce larger crystals one may either reduce the pre-treatment drying period of the film, use a lower vapour pressure (< 200 mb when using dichloromethane), or a greater vapour pressure (> 400 mb when using dichloromethane). Larger crystals can also be produced by using a more effective salt solvent as treatment vapour, however this has the disadvantage that the conversion efficiency of molecularly dispersed salt to microcrystalline form is lower.

4.4.2 Heat treatment

An alternative means of introducing mobility to the salt ions within an unconverted film is application of heat. When a film is heated above the glass transition temperature of the host polymer, it softens leading to enhanced mobility of the dispersed ions. This allows crystallisation to take place. The host polymer, PMMA has a glass transition temperature of

around 100 C (Polymer Handbook, 1989). Temperatures of 100 C to 150 C can be used to bring about crystallisation. Heat treatment is carried out in a vacuum oven to prevent oxidation of the salt ions in the film. Conversion times are shorter when higher temperatures are employed. At 150 C conversion typically takes 10-15 minutes, whereas at a temperature of 110 C conversion takes around 1 hour.

Control of crystallite size is limited with this technique. Generally crystallite size is larger when high temperatures are used although even with low temperatures crystallite size tends to be greater than 1 μm. The microcrystals tend to form a interlocking network of dendritic crystals. Figure 4.6 shows an optical micrograph of a K(TCNQ) doped film which had been thoroughly dried, then heat treated at 120 C under vacuum for 40 minutes and which exhibits such a crystalline network.

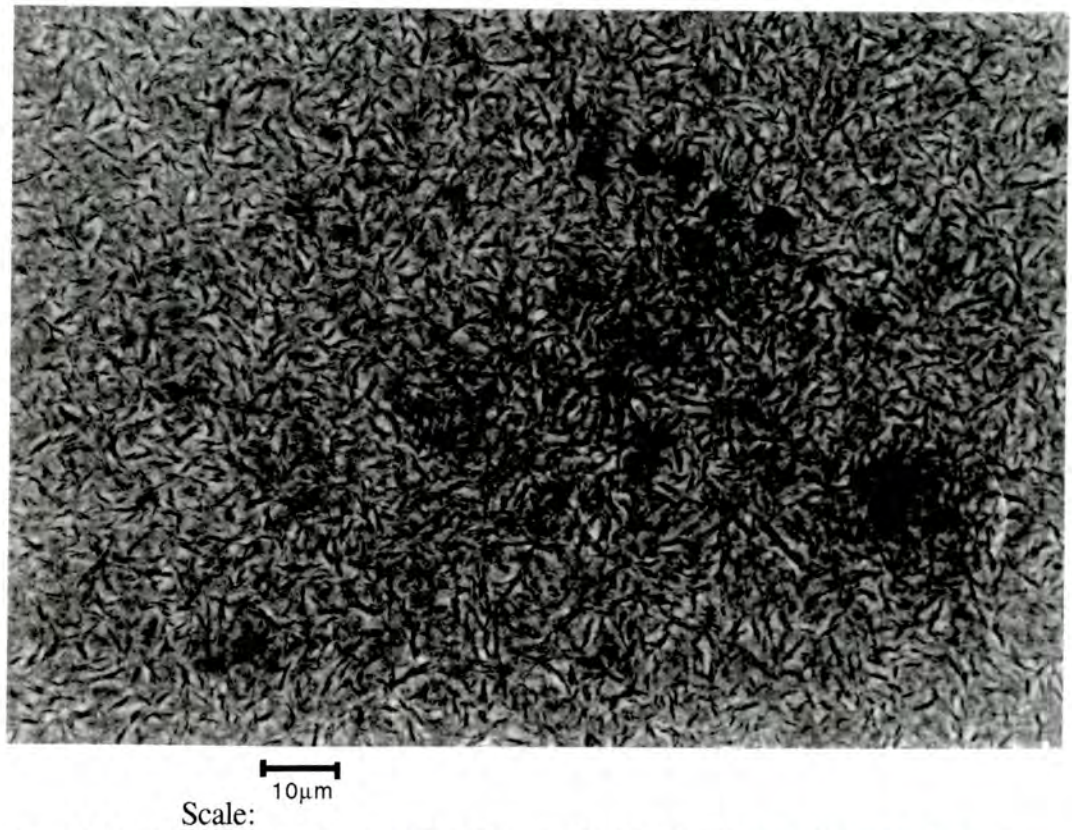

Figure 4.6 Optical micrograph of a K(TCNQ) doped PMMA film heat-treated under vacuum (120 C, 40 mins.)

4.5 Discussion

It seems that a number of macroscopic parameters can influence the conversion process. It would be useful to know how these parameters influence the underlying microscopic mechanisms which govern crystallisation. A critical factor in determining the crystallite size in the final film is the mobility of the salt ions during the conversion process. One would expect that the greater the salt mobility the greater the ease with which salt ions are able to move under the influence of concentration gradients set up as phase separation begins. Thus once a crystallite has begun to grow it is able to draw salt ions from a relatively large surrounding volume leading to large crystallites. If the mobility is low however, diffusion is limited and crystallites are only able to attract salt ions from their immediate vicinity leading to smaller crystallites.

The mobility of the salt ions is influenced by two main factors:

i) The viscosity of the film during the treatment process
ii) The solubility of the salt in the solvent present in the film during conversion.

The viscosity of the film during conversion depends on the total amount of solvent present in the film. The solvent in the film is made up of two components: that which remains in the film from the parent solution and that which infuses during the vapour treatment. The greater the amount of the solvent present the lower the viscosity and the higher the salt ions' mobility. The presence of efficient solvents of the salt in the film during conversion, whether because some of the solvent from the parent solution of the film has been allowed to remain in the film, or because the vapour used in treatment is an efficient solvent of the salt, will greatly enhance the mobility of the salt ions. The production of large crystals, when using good salt solvents as treatment vapour, or in films which have undergone short

drying periods, can be explained in terms of this enhancement in mobility.

When one considers the effect of vapour pressure on resulting crystal size the simple trend of lower viscosity and therefore higher mobility environments leading to larger crystallite size is not followed:

Consider the case of thoroughly dried films, vapour treated with non-solvents of the dopant salt. Viscosity in such cases is governed solely by the amount of infused solvent within the film. This in turn is determined by vapour pressure in the treatment vessel during conversion - the greater the vapour pressure the greater the amount of infused solvent. The tendency for larger crystals to form when high vapour pressures are used during conversion could be explained as being due to the increased ability of vapour to infuse the films at these high pressures leading to more solvent being present in the film and hence lower viscosities. At intermediate vapour pressures, less vapour infuses the film so viscosity is higher and resulting crystals are smaller. However the fact that below a certain vapour pressure large crystals are again obtained does not follow the expected trend. It seems to suggest that some other factor is important in determining crystal size.

One factor to bear in mind is that crystallite distributions are subject to change particularly in low viscosity environments i.e. transfer of material between already formed crystals is possible whereby large crystals grow by drawing material from their smaller neighbours. We might imagine that at intermediate and high vapour pressures, the low prevailing viscosity results in the rapid formation of an initial distribution of very small suboptical crystals on treatment. At intermediate pressures this distribution endures for a sufficiently long period to allow one to halt the treatment and remove the film maintaining the suboptical crystallite size distribution. At high pressures however the lower viscosity results in a more rapid conversion from the initial small crystal distribution to one

containing larger crystals by the process described above. Thus it is not possible to remove the film from the treatment vessel quickly enough to halt this process, and a final film containing larger crystals results. This conclusion is supported by the fact that at intermediate pressures, prolonging vapour exposure after full conversion has occurred, results in large crystals as opposed to the sub-optical ones found in films removed promptly following full conversion, i.e. the distribution of sub-optical crystals converts to one containing crystals of a larger size.

At lower vapour pressures it is noticeable that conversion takes significantly longer than at higher pressures. Due to the high viscosity the initial rapid precipitation stage resulting in small crystals may be avoided and hence a gradual growth of crystals occurs in which those formed first, inhibit the growth of further crystallites. This would result in fewer, but larger crystals in the final film, as observed.

Some evidence that low viscosities lead to a fast nucleation, of a large number of very small crystallites whereas high viscosity environments lead to slow nucleation, of fewer but larger crystals, comes from recent work by Yao (1992). This work dealt with formation of CuBr microcrystalline dispersions in PMMA using a heat treatment process. Film viscosity during crystallisation was determined by the temperature employed. Films containing ionically dispersed CuBr when heated to high temperatures (145 C) for short periods (20 s) were found to contain large numbers of small crystals (6 nm in diameter). Identical films treated at lower temperatures (75 C), took longer to convert, (5 mins) and were found to contain larger crystals (15 nm in diameter).

4.6 Determination of crystallite size

Apart from the use of optical microscopy a number of techniques have been employed in an attempt to determine crystallite size in the composite films. In particular it was hoped a means might be found to determine crystallite dimension in films containing suboptical crystals - crystals too small to be visible under an optical microscope i.e. less than around 0.5 μm.

The first technique attempted was scanning electron microscopy. In this technique a film coated in a thin layer of gold to prevent charge accumulation, is viewed under the electron microscope. It was hoped that crystallites protruding above the surface would become visible at sufficiently high magnifications. However this was not the case - the surface appeared smooth. Attempts were then made to view a cut film along the severed edge. However images obtained were indistinct with the film edge exhibiting complicated surface patterns. No clearly identifiable crystallites were visible. In addition the polymer film suffered severe damage (melting), before high magnifications were reached.

The second technique investigated was transmission electron microscopy (TEM). This technique required very thin samples to allow transmission of the electron beam - < 0.1 μm . Such films are hard to form directly and instead the preferred approach is to cut very thin sections from a much thicker films. To do this a method widely used in biological science was employed. The film in question is introduced into a liquid resin, to which a hardening agent is added causing the resin to set. The hardened resin is then cut so as to expose the film's edge. A microtome is then used to cut, with a diamond blade, thin sections containing samples of the film. In theory sections as thin as a few nanometers can be prepared using this method. Unfortunately most widely used commercial resins dissolved both the films and the crystallites they contained. The resins which did not dissolve the

films were of a type not suited for forming the necessary very thin sections. The sections which were obtained, when viewed using TEM, revealed no clearly identifiable crystals. Once again damage caused by the electron beam even at moderate magnifications, caused great difficulty when viewing the images.

It has been suggested that one reason for the difficulty in imaging the crystallites within the film is the low contrast between the crystalline material and surrounding host polymer (PMMA), due to similarity in electron density of the elements making up the two media. One technique which is sometimes employed for overcoming such difficulties is use of dyes containing heavy metals such as osmium, to stain certain regions of the section and hence improve contrast. It is hoped this may be attempted in the future.

The final technique which has been attempted is that of small angle X-ray scattering. Such measurements have been carried out at BICC Research Laboratories in Wrexham. The angular intensity profile of X-rays scattered at small angles contains information relating to the features in a sample such as microscopic inhomogeneity which are of larger scale than revealed by X-rays diffracted through larger angles which relate to much smaller structural features such as lattice spacings, (Glatter 1982). The presence of dispersed microcrystals should therefore be detectable using this method. In fact this technique is widely used in the study of semiconductor doped glasses described in chapter 1. When using the technique the problem is not in preparing thin samples as required for TEM measurements, but rather in preparing sufficiently thick samples to produce a measurable effect on the X-ray diffraction pattern. The as prepared films are of around 10 μm. Such a film produced no detectable small angle scattering. Further attempts were made using several folded films producing a combined thickness of 0.3 mm however once again the results did not enable determination of crystallite dimension. The scattered X-ray intensity at small angles is proportional to $(p_2-p_1)^2$, (p_1 = electron density of solute - the dispersed crystallites, p_2 =

electron density of solvent, in this case PMMA, (Glatter 1982)). Obtaining useful data requires a sufficiently high electron density contrast. Thus the difficulties encountered with this technique may be due to an insufficient electron density difference, p_2-p_1, of the two components of the films.

Chapter 5

Linear Optical Properties of Composites

5.1 Visible absorption spectra

The linear absorption spectra described in this section are the results of measurements made using a Perkin Elmer UV/VIS/NIR Lambda 19 spectrometer using unpolarised light. The use of undoped PMMA films in background measurements compensated for losses due to the host polymer and glass substrate, as well as the reflection from the interfaces of the sample.

5.1.1 Dichloromethane vapour treated films

Measurement of linear absorption spectra can be used to determine the efficiency of conversion from molecularly dispersed phase to microcrystalline phase. The absorption spectrum of an untreated K(TCNQ) doped film is shown in figure 5.1. The ordinate shows the molar absorption coefficient as defined in equation 5.2. The spectrum is typical of the monomer $(TCNQ)^-$ as obtained from solution spectra measurements, (Boyd 1965), with strong absorption at 3.1 eV and 1.46 eV with peak height ratio of 0.6. Shown in the same figure is the absorption spectrum of a K(TCNQ) doped film, vapour treated with dichloromethane at 300 mb to induce crystallisation, (see chapter 4). The crystallites present in the film were of sub-optical size. The absorption spectrum of K(TCNQ) crystals, grown from solution, ground and dispersed in a KBr disc is also shown for

comparison.

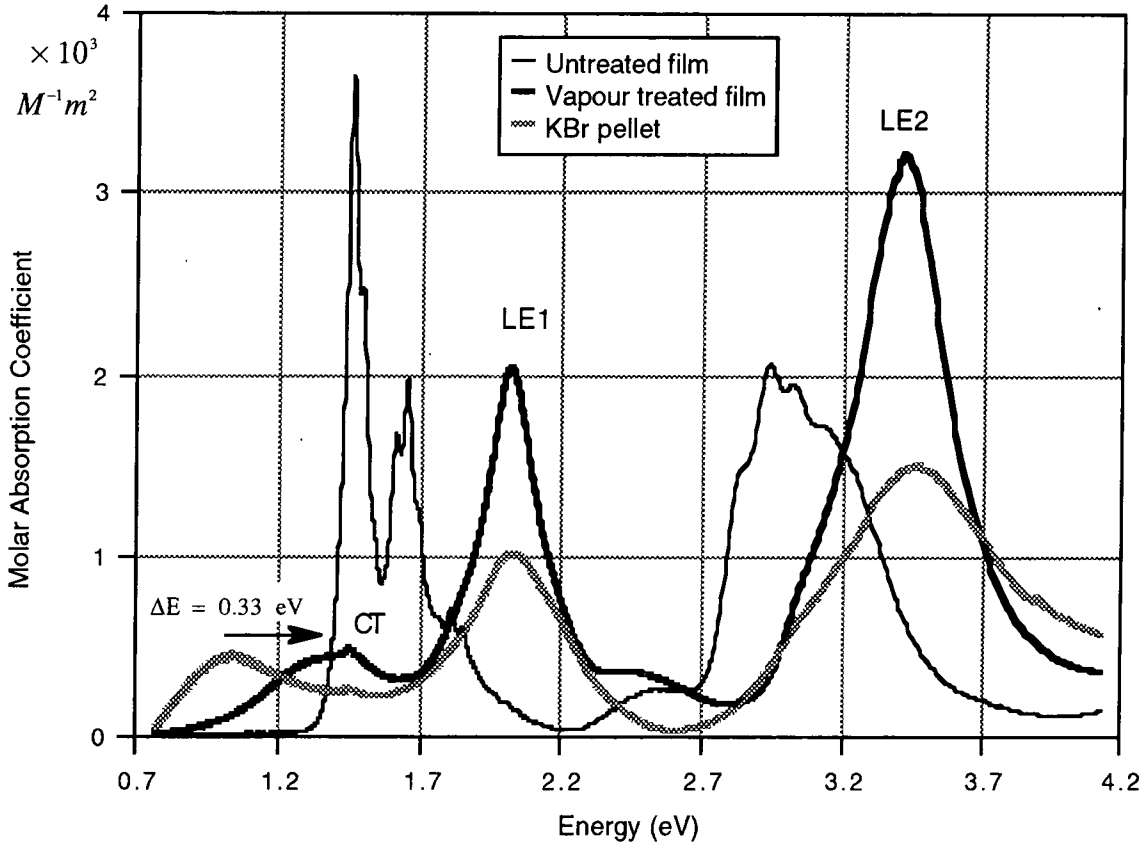

Figure 5.1 Absorption spectra of K(TCNQ) dispersions

NB: ΔE = energy shift of CT peak between KBr disc dispersion and thin film dispersion

The absorption spectrum of the vapour treated film containing K(TCNQ), possesses the three characteristic peaks typical of the absorption spectra of the alkali metal salts (see chapter 3 section 3.5). Only a small residual absorption due to the presence of $TCNQ^-$ ions is apparent, indicating the near 100% conversion to microcrystalline phase. The minor absorption feature around 2.5 eV is due to the formation of α,α-dicyano-p-toluoylcyanide following reaction of $TCNQ^-$ ions with water, when in solution (Mizoguchi 1978). The excellent conversion efficiency associated with dichloromethane vapour treatment led to its choice as preferred treatment vapour. It can be seen that the low energy charge transfer peak (CT) is significantly shifted to higher energy in the case of the treated film compared to the KBr disc dispersion.

Figures 5.2, 5.3 and 5.4 show the absorption spectra of Na(TCNQ), Rb(TCNQ) and Li(TCNQ) doped films respectively, treated with dichloromethane vapour at 300 mb.

Again the crystallites in these films are of sub-optical size. Also shown in each figure is the absorption spectra of a KBr disc containing the same TCNQ salt as is in the film.

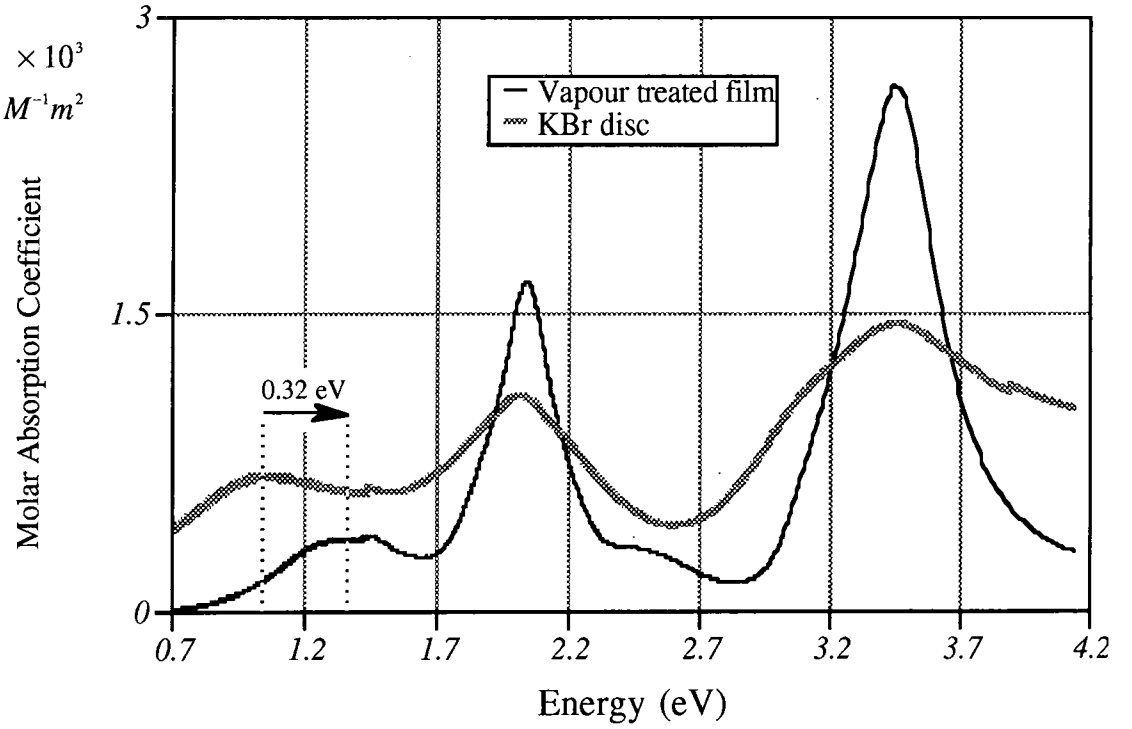

Figure 5.2 Absorption spectra of Na(TCNQ) dispersions

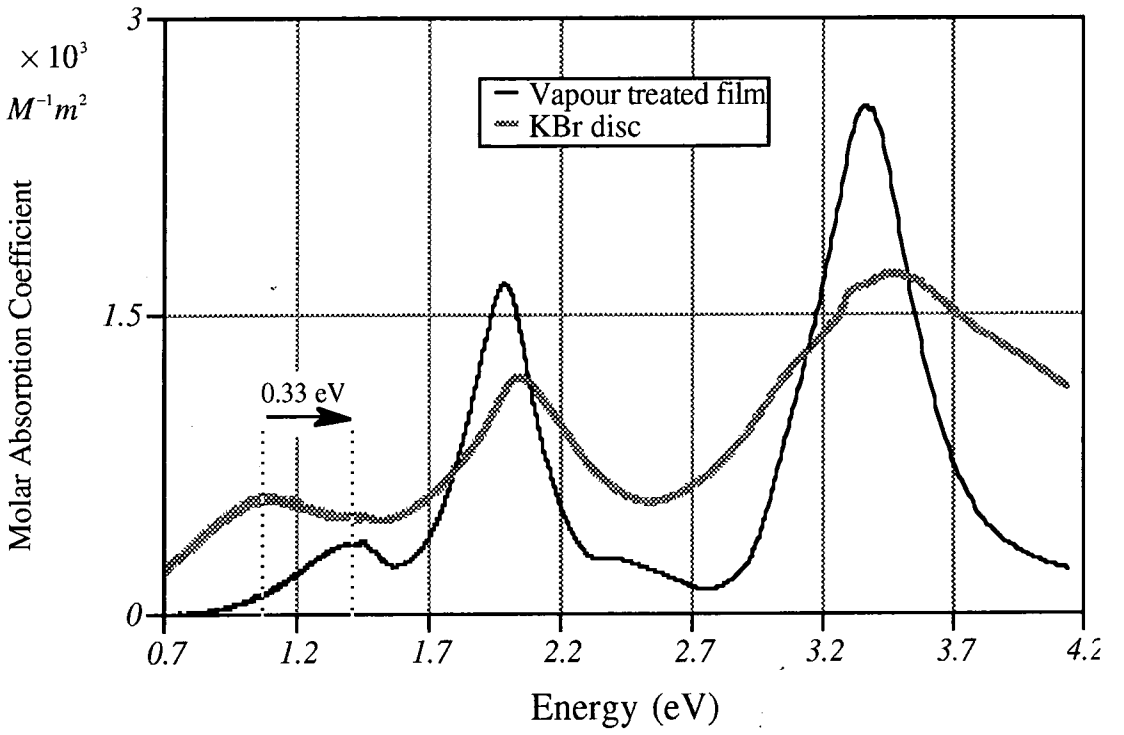

Figure 5.3 Absorption spectra of Rb(TCNQ) dispersions

3

lm2

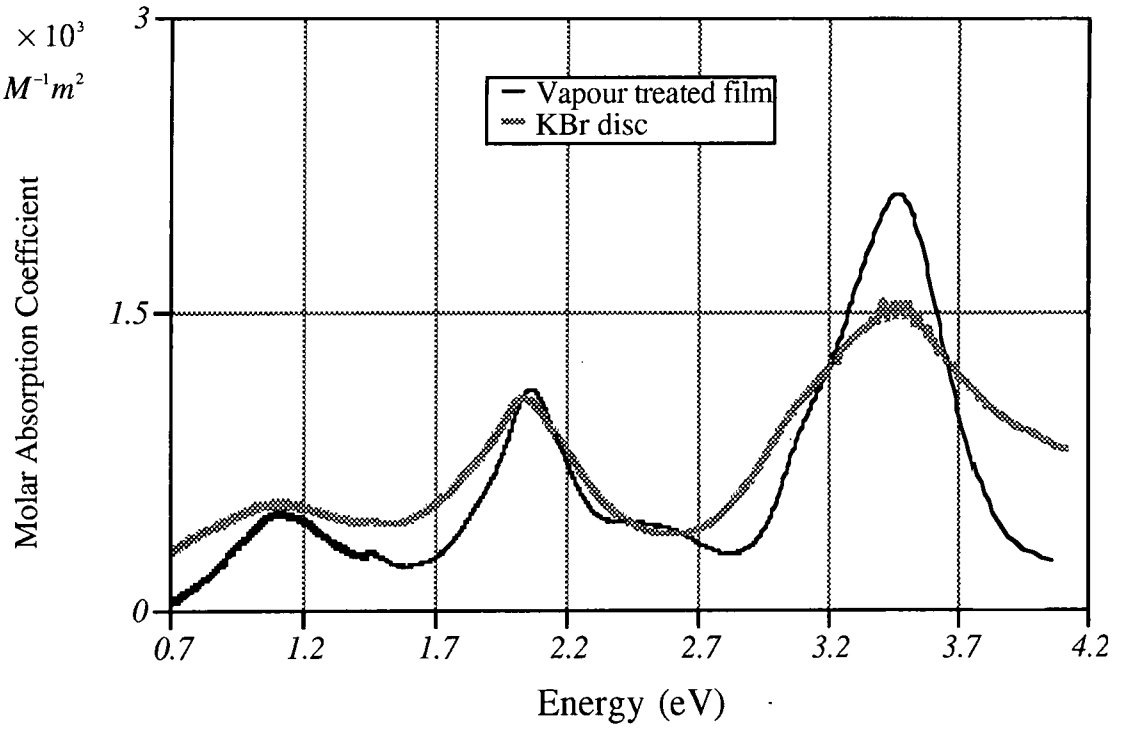

Figure 5.4 Absorption spectra of Li(TCNQ) dispersions

As with K(TCNQ), the CT band of thin film dispersions containing Na(TCNQ) and Rb(TCNQ) is shifted to higher energies compared to its position in KBr disc dispersions of the same salt. Such shifts have been observed before in suspensions of microcrystals of these salts in liquids (Papavassiliou 1977, 1978) and have been attributed to differences in the shape of microcrystals in the dispersions (see below).

In contrast, no shift is seen in the CT band of the Li(TCNQ) doped film compared to that of the KBr disc containing this salt.

5.1.2 Acetone, acetonitrile treated films

The spectrum of a K(TCNQ) doped film, treated with acetone vapour is shown in figure 5.5. This spectrum contains significant residual absorption typical of $TCNQ^-$, indicative of incomplete conversion from molecularly dispersed phase to microcrystalline phase.

Crystallites in this film were of around 5 μm diameter. The CT band is again shifted to higher energy compared to its position in the KBr disc spectrum, (also shown in figure 5.5), although the band does extend further into the low energy region than in the case of the dichloromethane treated film (figure 5.1). Similar results are obtained in the case of Rb(TCNQ) and Na(TCNQ) doped films treated with acetone. Treatment of K, Rb and Na(TCNQ) doped films with acetonitrile leads to very poor conversion efficiency and the absorption spectrum remains dominated by the remaining $TCNQ^-$ ions

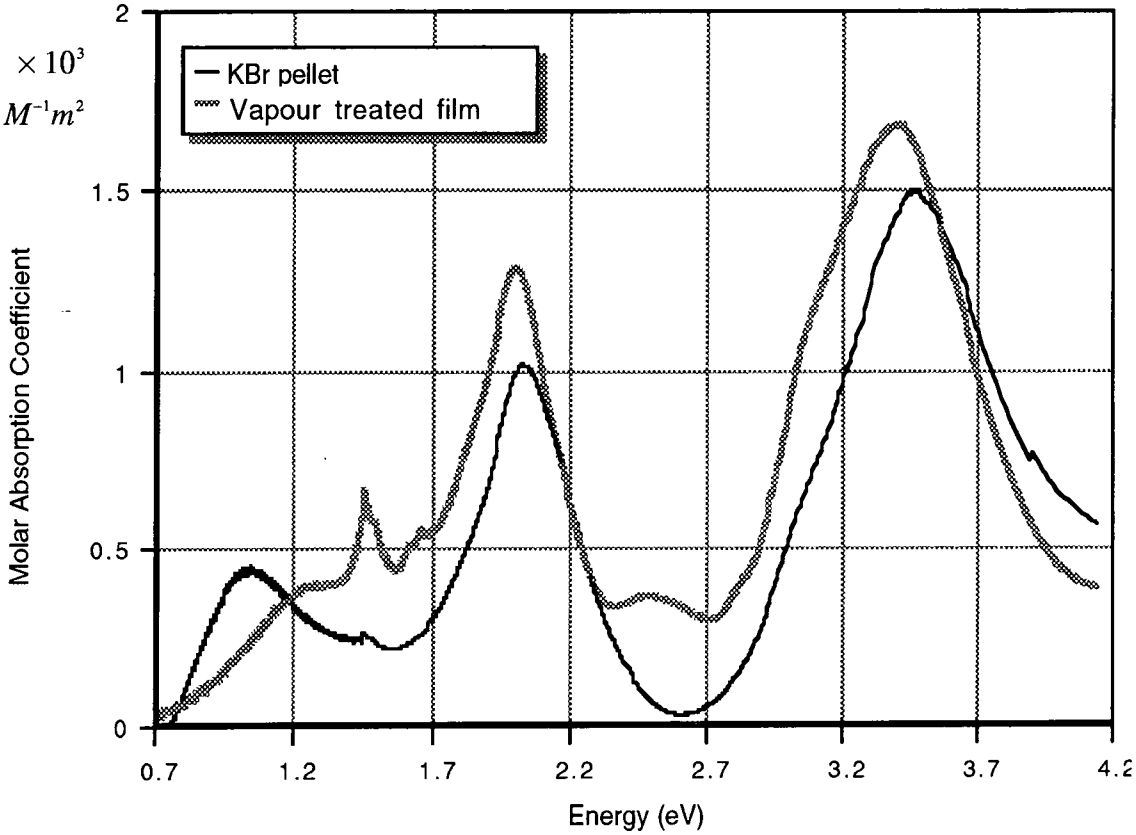

Figure 5.5 Absorption spectrum of K(TCNQ) doped, acetone vapour treated film

The spectrum of a Li(TCNQ) doped film treated with acetonitrile vapour is shown in figure 5.6. This spectrum contains significant residual absorption typical of $(TCNQ)^-$, indicative of incomplete conversion from molecularly dispersed salt to microcrystalline phase. Crystallites in this film are of various sizes. Visible crystals take the form of needles of 1-2

μm in length (see figure 4.2). However extensive regions also exist where crystals are of sub-optical size. In contrast to Na(TCNQ), K(TCNQ) and Rb(TCNQ) the CT band is shifted to lower energy compared to its position in both the Li(TCNQ)/KBr disc spectrum and in the dichloromethane vapour treated film (shown in figure 5.4). Similar spectra are obtained if acetone is used as treatment vapour.

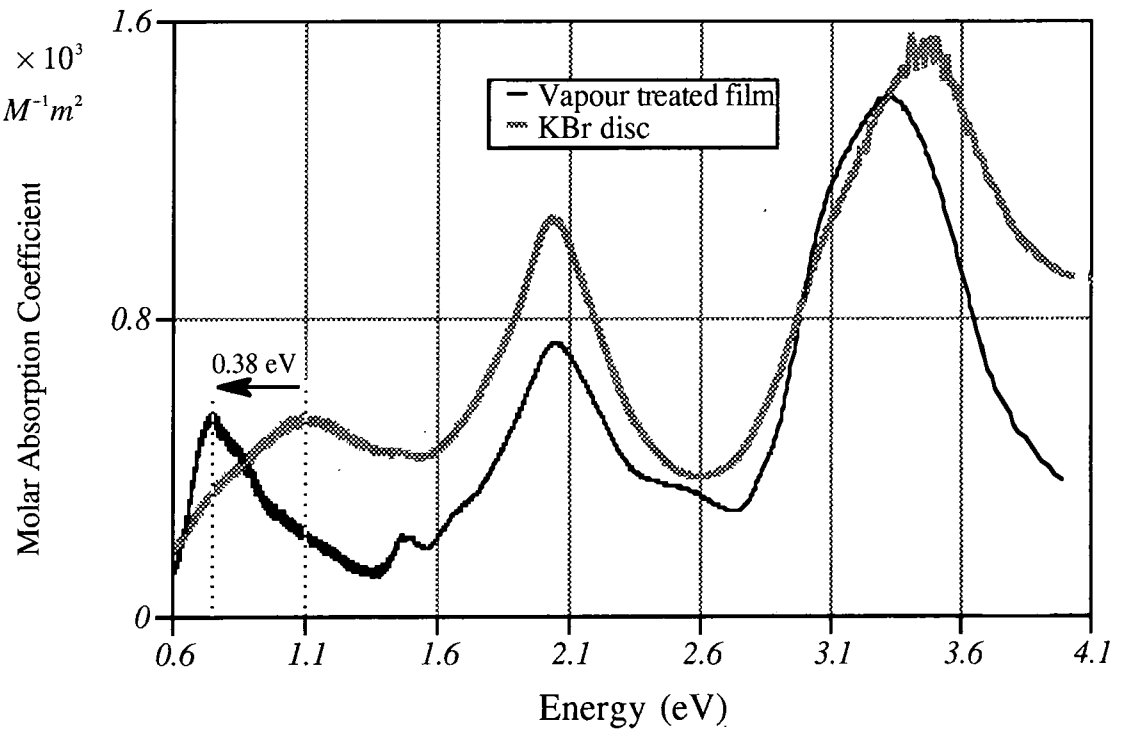

Figure 5.6 Absorption spectrum of Li(TCNQ) doped, acetonitrile vapour treated film

5.2 Calculation of oscillator strength of optical transitions

The oscillator strength of the transitions giving rise to the absorption bands in the visible spectrum can be calculated using, (Atkins 1990).

$$f_{nm} = \left(\frac{4\varepsilon_0 m_e c^2 \ln 10}{N_A e^2} \right) \int_{v1}^{v2} \varepsilon(\nu) d\nu \qquad (5.1)$$

Where: N_A= Avogadro's constant, m_e = electron mass, ε_0 = permittivity of free space and $\varepsilon(\nu)$ is the molar absorption coefficient which is given by

$$\varepsilon(\nu) = \frac{\log_{10}\left(I_\circ / I\right)}{\ell C} \qquad (5.2)$$

where Io = incident light intensity , I = transmitted light intensity, ℓ = film thickness C = salt concentration and, υ = wavenumber

This equation is only strictly valid for homogeneous systems. For the composites studied here it is also valid provided the size of crystallites is smaller than the wavelength of light used. The results of oscillator strength calculations for films where this is the case are given in table 5.1. No corrections for losses due to scattered light are made in the data analysis.

Salt	Absorption band	Peak position		Oscillator Strength
		nm	eV	
Li(TCNQ)	LE2	354	3.40	0.54
	LE1	591	2.10	0.21
	CT1	1128	1.10	0.07
Na(TCNQ)	LE2	356	3.48	0.46
	LE1	606	2.04	0.20
	CT1	890	1.39	0.09
K(TCNQ)	LE2	360	3.44	0.59
	LE1	610	2.03	0.24
	CT1	890	1.39	0.08
Rb(TCNQ)	LE2	360	3.44	0.46
	LE1	610	2.03	0.20
	CT1	890	1.39	0.06

Table 5.1 Oscillator strengths of absorption bands in thin film dispersions containing the alkali metal TCNQ salts, (neglecting scatter)

For the LE bands the integral in equation 5.1 is evaluated between the minima on either side of the respective peak. For the CT band the integral is evaluated between the peak wavelength and the wavelength at which the absorption coefficient first falls to zero. This value is then doubled to yield the required total integral. These results can be compared to the data of Oohashi in table 3.1. There is seen to be good agreement in the position of the LE bands with Oohashi's data for bulk grown material and for the thin film dispersions. However the CT band is seen to be shifted to higher energy in thin film dispersions of Na, Rb and K salts reported here. The oscillator strengths measured for thin film dispersions are substantially smaller for all three bands in the case of Na(TCNQ), although in the case of Rb(TCNQ), K(TCNQ) and Li(TCNQ) only the strength of the CT band is substantially reduced.

5.3 Effects of crystallite shape on the absorption spectra of composites

The results of the preceding sections indicate differences in the position of the CT band of TCNQ salt dispersions in KBr pellets compared to its position in vapour treated film absorption spectra. A possible explanation for this is the difference in crystallite shape within the two systems. Normally measurements of optical absorption are carried out on bulk samples which are many orders of magnitude larger than the exciting wavelength. In the case of microcrystalline dispersions of a material however this is not the case. The observed absorption spectra of dispersions are found to be dependent on the shape of the crystallites forming the dispersion. Mie, (1908), investigated this dependence and obtained a rigorous solution of absorption and scattering of light from an homogeneous sphere. This analysis was then extended to a collection of spheres. The approach is valid providing;

i) the distance between the spheres is large enough that they scatter independently,

ii) the spheres are randomly located to avoid interference effects,

iii) the optical density is small enough that essentially the same irradiance strikes each sphere.

In 1912 Gans (Gans 1912), extended Mie's theory of absorption and scattering of submicroscopic *spherical* particles to submicroscopic *non-spherical* particles. According to Gans, the energy removed from an incident beam by both light scattering and true absorption can be expressed in terms of the extinction coefficient γ, defined by:

$$T = \frac{I}{I_0} = e^{-\gamma x} \tag{5.3}$$

where Io is the intensity of the unpolarised incident beam, I is the intensity of the transmitted beam and γ, for a randomly oriented distribution of crystallites is given by:

$$\frac{\gamma}{NV} = \frac{2\pi\varepsilon_\alpha^{\frac{3}{2}}}{3\lambda} \sum_j \frac{\left(\frac{1}{P_j^2}\right)\varepsilon_{2j}}{\left(\varepsilon_{1j} + \frac{1-P_j}{P_j}\varepsilon_\alpha\right)^2 + \varepsilon_{2j}^{\,2}} \tag{5.4}$$

in which NV is the volume fraction of microcrystals within the composite medium, ε_α is the dielectric constant of the host medium, ε_{1j} and ε_{2j} are the j components of the real and imaginary part of the bulk crystalline dielectric function respectively with j = x,y,z and Pj is depolarisation factor for the j-axis.

Pj depends on the shape of the microcrystals. For example for elongated ellipsoids with dimensions in the principal directions X, Y and Z (see figure 5.7)

$$P_x = \frac{1-e^2}{e^2}\left[\frac{1}{2e}\ln\left(\frac{1+e}{1-e}\right) - 1\right] \quad ; \quad P_y = P_z = \frac{1-P_x}{2} \tag{5.5}$$

where $$e = \left(\frac{X^2 - Y^2}{X^2} \right)^{\frac{1}{2}} \qquad (5.6)$$

X > Z = Y

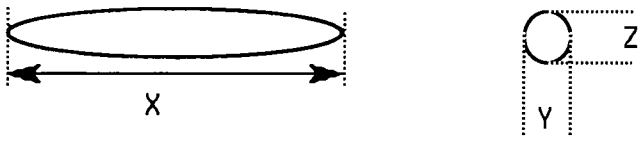

Figure 5.7 Elongated ellipsoids

Whilst for flattened ellipsoids, (see figure 5.8)

$$P_x = \frac{1}{e^2}\left[1 - \left(\frac{1-e^2}{e^2} \right)^{\frac{1}{2}} \sin^{-1}(e) \right] \quad ; \quad P_y = P_z = \frac{1 - P_x}{2} \qquad (5.7)$$

and where $$e = \left(\frac{Y^2 - X^2}{Y^2} \right)^{\frac{1}{2}} \qquad (5.8)$$

Y = Z > X

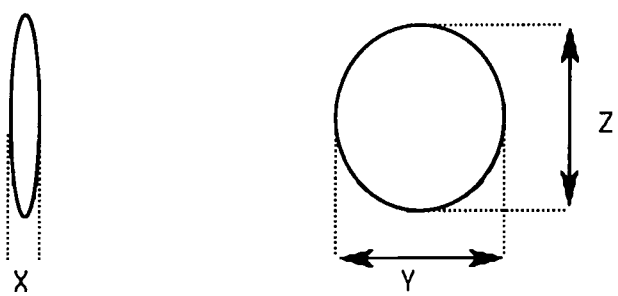

Figure 5.8 Flattened ellipsoids.

The dielectric properties of the alkali metal TCNQ salts are anisotropic. The dielectric function has essentially the same value in all directions perpendicular to the stacking axis, which is different to that parallel to it. Thus taking the x-axis to be the TCNQ stacking axis, $\varepsilon_y = \varepsilon_z \neq \varepsilon_x$ and the sum in equation 5.4 becomes

$$\frac{\gamma}{NV} = \frac{2\pi\varepsilon_\alpha^{\frac{3}{2}}}{3\lambda}\left[\frac{\left(\frac{1}{P_x^2}\right)\varepsilon_{2x}}{\left(\varepsilon_{1x}+\frac{1-P_x}{P_x}\varepsilon_\alpha\right)^2+\varepsilon_{2x}^{\,2}}+\frac{2\left(\frac{1}{P_y^2}\right)\varepsilon_{2y}}{\left(\varepsilon_{1y}+\frac{1-P_y}{P_y}\varepsilon_\alpha\right)^2+\varepsilon_{2y}^{\,2}}\right] \qquad (5.9)$$

Equation 5.9 holds for a random distribution of crystallites. For dispersions of anisotropic materials such as the TCNQ salts, and where some degree of crystallite orientation exists, it is necessary to use a weighted sum of each of the components in 5.9. Equation 5.9 then becomes:

$$\frac{\gamma}{NV} = \frac{2\pi\varepsilon_\alpha^{\frac{3}{2}}}{3\lambda}\left[\frac{a\left(\frac{1}{P_x^2}\right)\varepsilon_{2x}}{\left(\varepsilon_{1x}+\frac{1-P_x}{P_x}\varepsilon_\alpha\right)^2+\varepsilon_{2x}^{\,2}}+\frac{2b\left(\frac{1}{P_y^2}\right)\varepsilon_{2y}}{\left(\varepsilon_{1y}+\frac{1-P_y}{P_y}\varepsilon_\alpha\right)^2+\varepsilon_{2y}^{\,2}}\right] \qquad (5.10)$$

The factors a and b depend on the nature of the alignment of the crystallites, and polarisation of the incident light.

For instance, consider crystallites shaped as discs all orientated so that the Y and Z axes are perpendicular to the direction of propagation of an unpolarised, probe beam which is along the TCNQ axis (x-axis) as shown in figure 5.9.

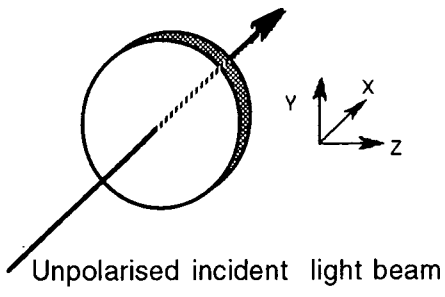

Figure 5.9 Disc, aligned with TCNQ axis parallel to propagation direction

Equation 5.10 can be used if the discs are treated as flattened ellipsoids. The optical field has no component along the x-axis and so does not induce polarisation parallel to the

TCNQ axis. Thus ε_x does not contribute to γ/NV in equation 5.10. The following values are then defined for a and b : a=0, 2b=3

Alternatively for needles (approximated as elongated ellipsoids), oriented so that the TCNQ axes (x-axis) of all the crystals are perpendicular to the propagation direction of an unpolarised incident beam (see figure 5.10).

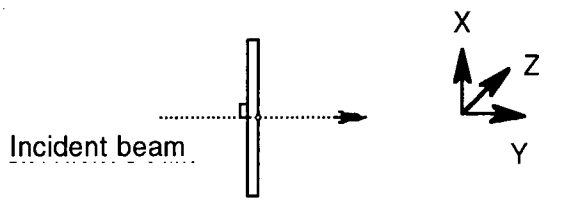

Figure 5.10 Needle, aligned with TCNQ axis perpendicular to propagation direction

the optical field has no component along the z-axis and so ε_z does not contribute to γ/NV in equation 5.10, Hence a=1.5, 2b=1.5.

For cases of partial alignment a and 2b take on intermediate values which can be determined by fitting values of a and b to experimental data.

5.4 Comparison of calculated absorption spectra with experiment

To illustrate the effects of crystallite shape and orientation on the absorption spectra of dispersions of microcrystals, Mie-Gans theory as outlined above, has been applied to several theoretical crystal morphologies.

5.4.1 Effect of microcrystal shape on absorption spectra of randomly oriented crystals

Using values for the dielectric function listed in appendix 3, (calculated by Papavassiliou from Kramers-Kronig analysis of reflectance measurements, (Papavassiliou 1979)) , the absorption spectra of a random distribution of K(TCNQ) crystals having the following shapes have been calculated.

i) Needles with TCNQ (long) axis:short axes ratio 7:1 (figure 5.11)

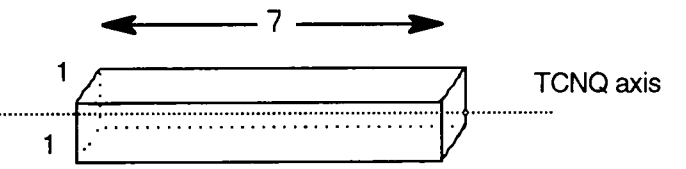

Figure 5.11 Needles

ii) Spheres

iii) Discs with TCNQ(short) axis:long axes ratio 1:7 (figure 5.12)

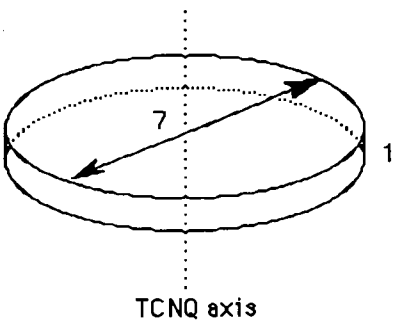

Figure 5.12 Discs

The results are shown in figure 5.13

Figure 5.13 illustrates that the position of the low energy charge transfer (CT) peak is

sensitive to the shape of the crystallites forming the distribution.

In the limit of needles with TCNQ/short axis ratio = ∞, the CT peak achieves its minimum energy position of 0.9 eV. In the limit of discs with TCNQ/long axis ratio = 0, the CT peak achieves its maximum energy position of 1.5 eV. The CT peak shifts monotonically between these two extremes as shape changes from needles to discs, (spheres are predicted to produce a CT peak at around 1.15 eV). This shift of the CT band to higher energy is accompanied by an increase in the extinction coefficient of both the CT and LE1 bands.

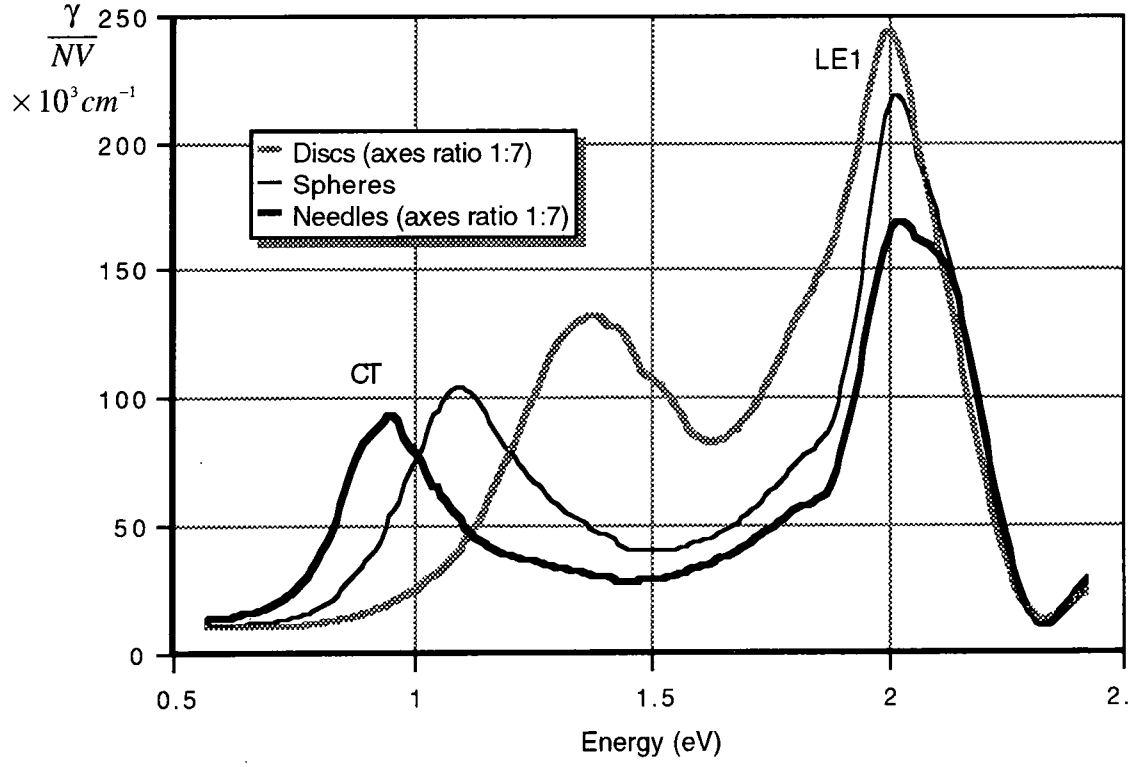

Figure 5.13 Calculated dependence of absorption spectra of K(TCNQ) microcrystals on crystallite shape

5.4.2 Case of oriented crystallites

In the case of oriented crystallites the position of the absorption peaks is found not to alter

with varying degrees of alignment, remaining dependent only on crystallite shape. However the relative strength of the absorption peaks is found to be dependent on the degree of orientation. This dependence has its origin in the factors 'a' and '2b' in equation 5.10.

To illustrate the effect of crystallite orientation on the absorption spectrum of a dispersion of crystallites, the absorption spectra of thin discs with TCNQ, (short) axis/long axes ratio =1:7 have been calculated. The calculations assume an unpolarised incident light beam. The following orientations of crystallites are considered:

i) a=1, 2b=2 This corresponds to random orientation of crystallites, (see figure 5.14)

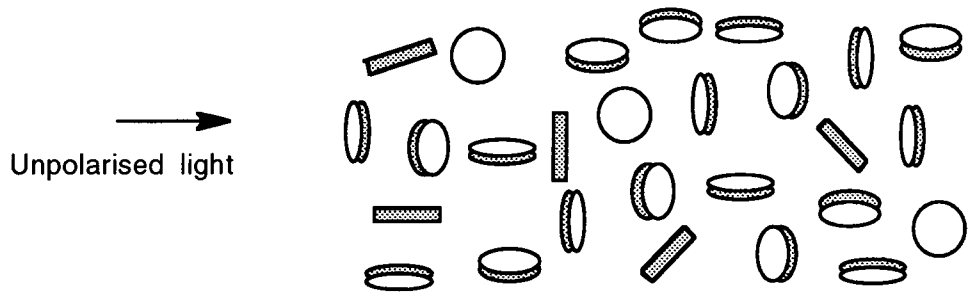

N.B. TCNQ stacking axis
parallel to short axis of disc

Figure 5.14 Random orientation of discs

ii) a=0, 2b=3 This corresponds to a case in which the TCNQ axes of all crystals are parallel to the direction of propagation of incident light, (see figure 5.15).

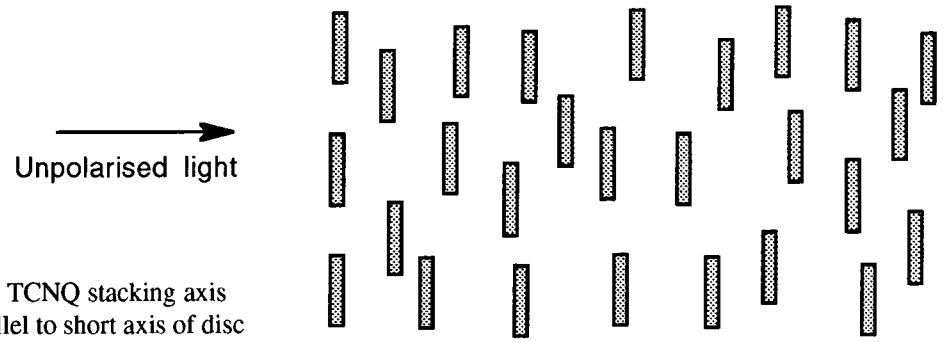

N.B. TCNQ stacking axis
parallel to short axis of disc

Figure 5.15 Complete alignment, TCNQ stacking axis parallel to propagation direction

iii) a=0.6, 2b=2.4 This corresponds to a dispersion containing discs preferentially aligned with their TCNQ axis parallel to the direction of propagation of incident light, but where alignment is incomplete, (see figure 5.16).

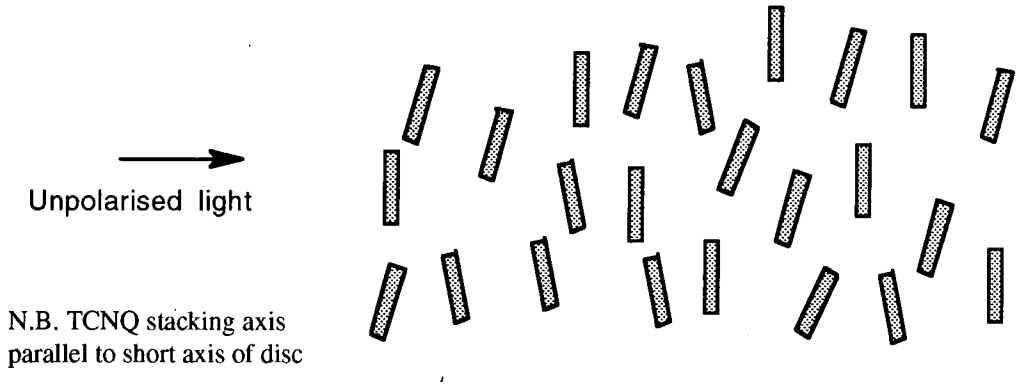

Figure 5.16 Partial alignment, TCNQ stacking axis parallel to propagation direction

iv) a=1.5, 2b=1.5 This corresponds to a dispersion where the TCNQ axis of all the crystals are perpendicular to the direction of propagation of the incident light, as in figure 5.17

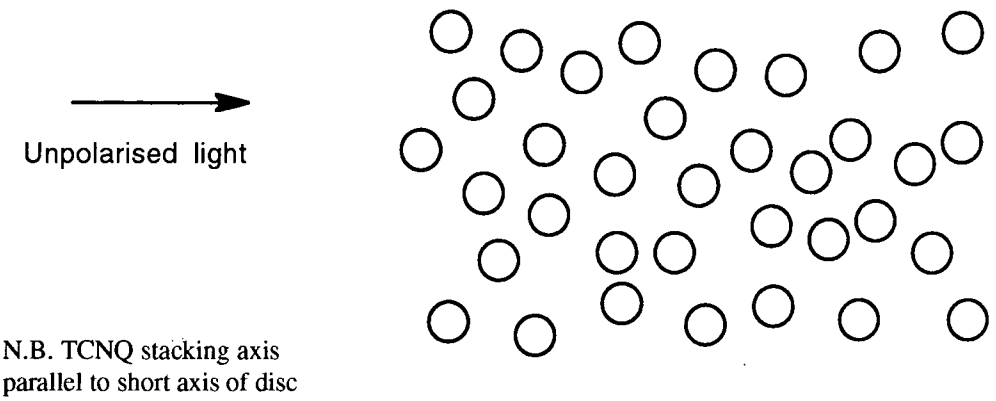

Figure 5.17 Complete alignment, TCNQ stacking axis perpendicular to propagation direction

The results are shown in figure 5.18. Clearly as the parameter 'a' decreases (corresponding to increasing tendency of discs to align with their TCNQ stacking axis parallel to the direction of propagation of light), the CT band decreases in strength and the LE1 band increases in strength. The position of the respective bands however remains essentially unaffected. These general trends are also

exhibited by oriented distributions of other crystal shapes, such as needles.

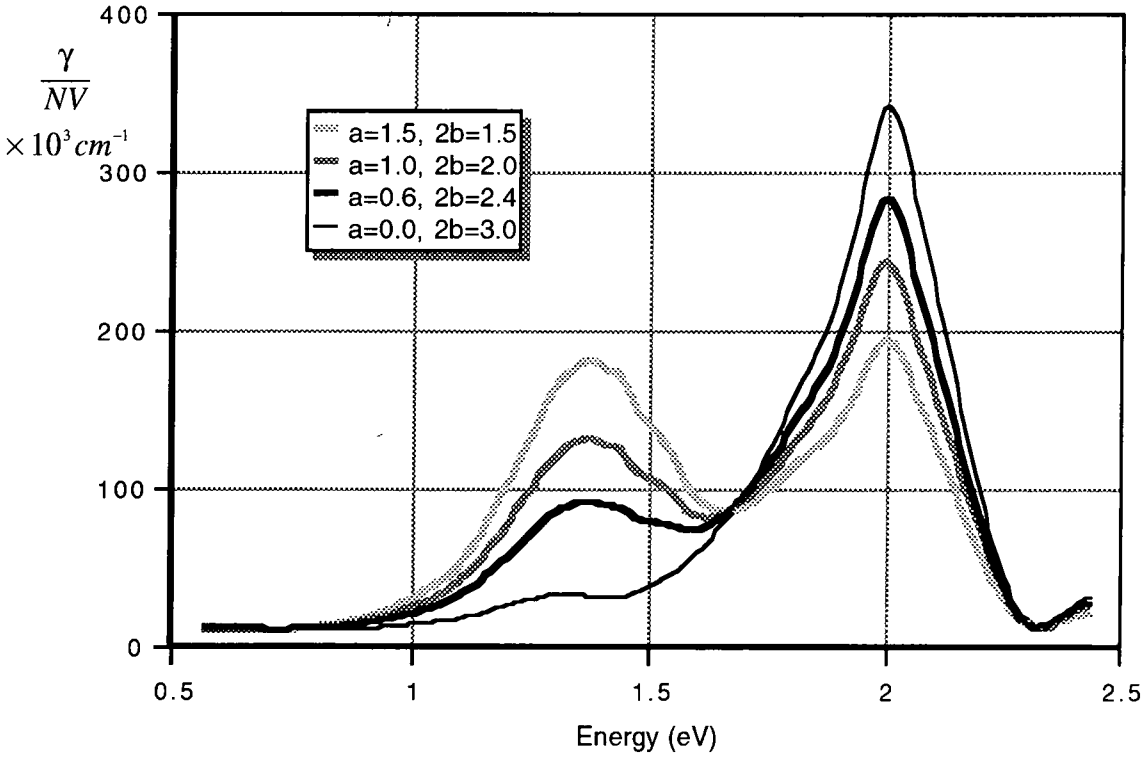

Figure 5.18 Effect of crystallite orientation on the absorption spectrum of K(TCNQ) discs (axes ratio 1:7)

In summary Mie-Gans theory predicts that the shape of the crystallites affects the position of the CT band, and influences the strength of the absorption peak. Degree of orientation effects the strength of the absorption peaks only.

5.4.3 Comparison with experiment

The first experimental work investigating the effect of microcrystal shape on the absorption spectra of K(TCNQ) dispersions was that of Papavassiliou (1977). There, suspensions of disc shaped K(TCNQ) microcrystals were obtained by introducing a few drops of a solution of K(TCNQ) in acetonitrile, into chloroform. Other techniques were used to produce needle shape crystals and spherical shaped crystals. The absorption spectra of the three types of dispersions fitted well the predictions of Mie-Gans theory with discs

producing the highest energy charge transfer band, and needles the lowest energy charge transfer band. The absorption spectrum of a dispersion of Na(TCNQ) formed by the method of Papavassiliou for producing discs is shown in figure 5.19. The high energy position of the charge transfer band confirms the results of Papavassiliou.

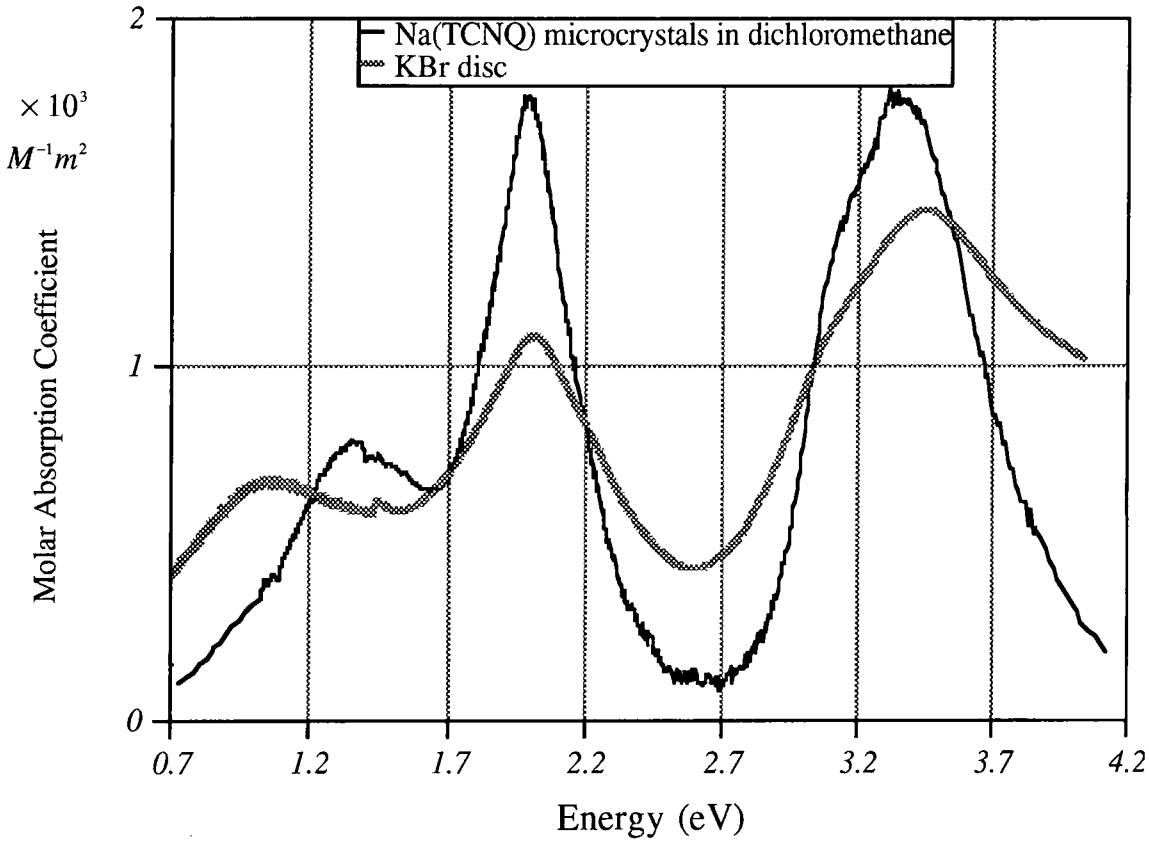

Figure 5.19 Absorption spectrum of Na(TCNQ) in DCM and KBr discs

Mie-Gans theory is now applied to the absorption spectra of K(TCNQ) doped PMMA films.

In figure 5.20, the absorption spectrum of a K(TCNQ) doped PMMA film containing sub -optical crystallites is shown. The film was treated with dichloromethane vapour at a pressure of 320 mb. The film took 1 minute to convert. The high energy position of the CT band is such that Mie-Gans theory predicts the crystallites in the film are disc shaped. The strength of the CT band is less than would be predicted for a random distribution of such discs whereas the LE1 band is stronger. Also shown in figure 5.20 is a calculated

absorption spectrum for a dispersion of K(TCNQ) crystallites in the form of discs, with axial ratio 1:7 and with a = 0.2 and 2b = 2.8, (see equation 5.10) which provided the best fit to the data. These values of a and 2b imply preferentially alignment of crystallites with their TCNQ stacking axes (short axes in the case of discs), parallel to the direction of propagation of the incident beam i.e. perpendicular to the plane of the film.

In figure 5.21 the absorption spectrum of a K(TCNQ) doped PMMA film containing crystallites of approximately 1 μm diameter is shown. The film was treated with dichloromethane vapour at a pressure 460 mb. The film took 30 seconds to convert. Also shown is a calculated absorption spectrum for a dispersion of K(TCNQ) crystallites in the form of discs with axial ratio 1:12 and with a=0.5 and 2b =2.5, (see equation 5.10) which provided the best fit to the data. These values of a and 2b correspond to discs, preferentially aligned with their TCNQ axes parallel to the direction of propagation of incident light, although the alignment is less complete than in the case illustrated in figure 5.20.

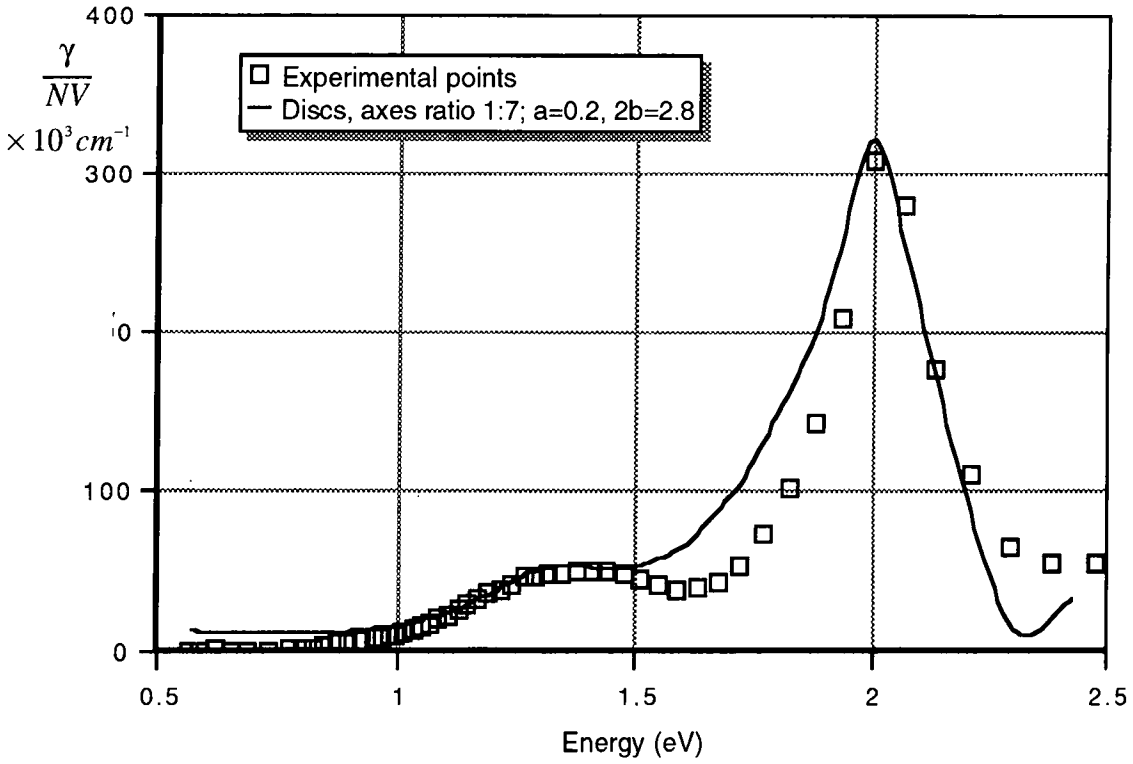

Figure 5.20 Absorption in K(TCNQ)/PMMA film

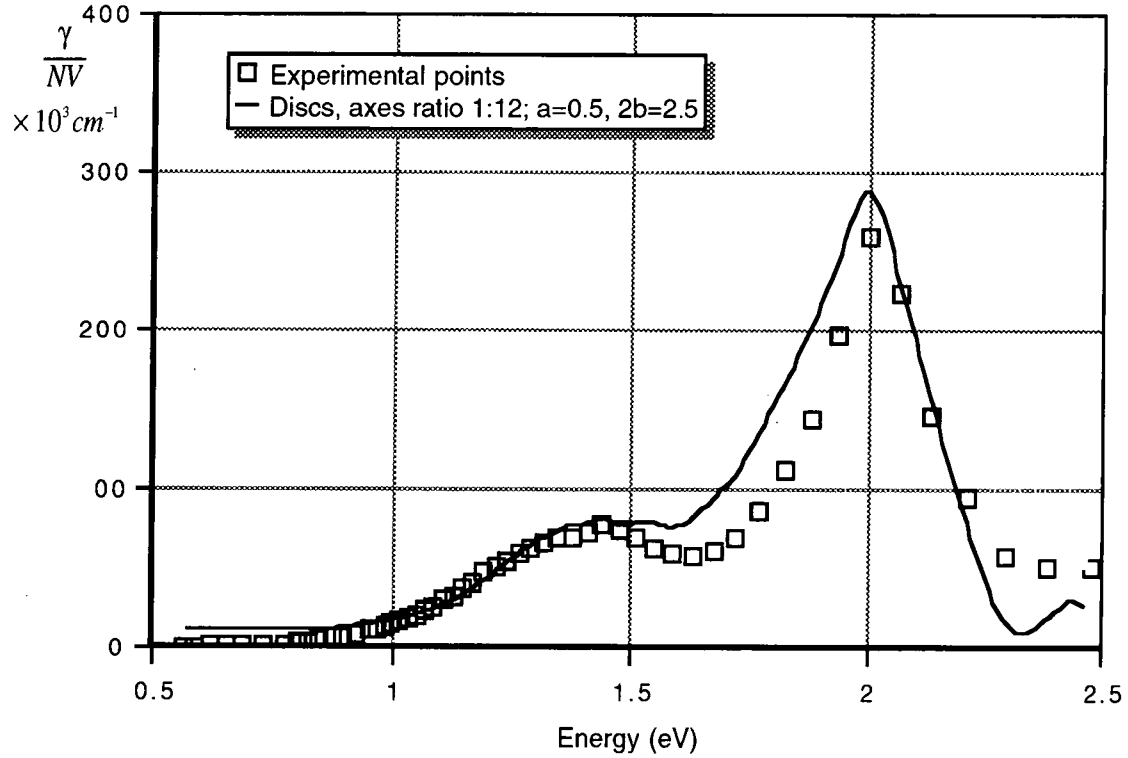

Figure 5.21 Absorption in K(TCNQ)/PMMA film

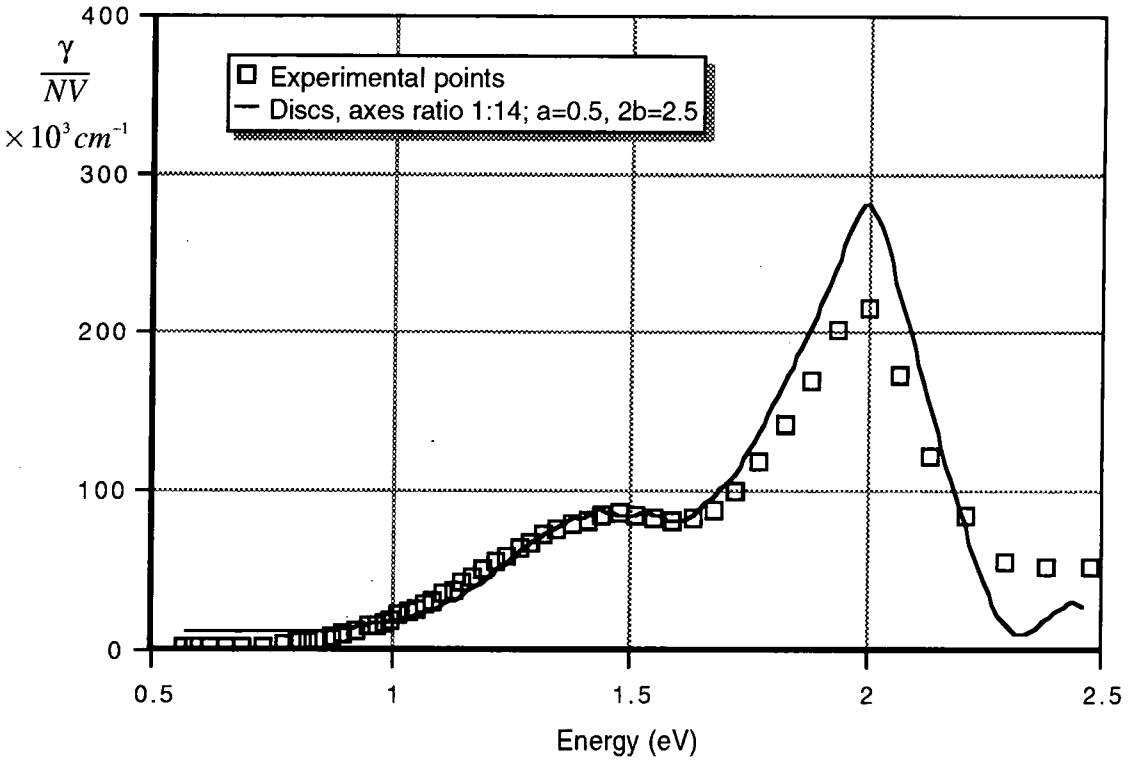

Figure 5.22 Absorption in K(TCNQ)/PMMA film

In figure 5.22 the absorption spectrum of a K(TCNQ) doped PMMA film containing

approximately 1 μm diameter crystallites is shown. This film was treated with dichloromethane vapour at a pressure 522 mb. Conversion took 10 seconds. Also shown in figure 5.22, is a calculated absorption spectrum for a dispersion of K(TCNQ) crystallites in the form of discs with axial ratio 1:14 and with a=0.5 and 2b=2.5, (see equation 5.10). These values of a and 2b correspond to discs, preferentially aligned with their TCNQ axes parallel to the direction of propagation of incident light.

Thus on the basis of Gans theory the high energy position of the CT band suggests that the crystallites in the dichloromethane vapour treated films are disc shaped. The strength of the CT band is significantly weaker than would be expected for randomly oriented discs whilst the LE1 band is stronger than expected for a random distribution. This can be explained by assuming preferential alignment of discs with their TCNQ chain axes parallel to the direction of incident light i.e. perpendicular to the plane of the film. With the values of a and 2b chosen as described above reasonable fits to the experimental data are obtained. The differences in the fitted values of crystallite axial ratios and of a and 2b, for films treated using different vapour pressures, suggests that crystallite shape and degree of alignment is sensitive to this parameter.

An alternative explanation for the low strength of the CT band is the effect of aggregation. Papavassiliou (1977) suggested that reductions in the strength of absorption bands could be explained as being due to spread of particle size and aggregation of particles in the sample, however aggregation should reduce the intensity of the LE1 band as well as the CT band whereas in this work the LE1 band is enhanced in intensity over what would be expected for a non-aggregated, random distribution of crystals.

The particle size in many of the films described above is around 1 μm which is larger than allows strict quantitative application of Mie-Gans theory, this could account for the discrepancies between theory and experiment in the strength of charge transfer band.

However even in the case of the film containing sub-optical crystals where Mie-Gans theory is quantitatively applicable, the CT band is of reduced intensity compared to the calculated spectrum based on the assumption of a random crystallite distribution.

Unfortunately it is not possible to test the Mie-Gans prediction of crystal shape and alignment directly since as described in the previous chapter it has not proved possible to observe the shape of crystallites within the films which produced the above spectra. Very thick films of over 100 μm, when treated with dichloromethane in the same way as thinner films described above, do produce distributions of crystals large enough for their shape to be determined using optical microscopy. They are found to contain complex shaped crystals, consisting of many branched, tree like structures (see figure 5.23). This obviously contrasts with the disc-like shapes predicted by Mie-Gans described earlier and suggests that the same treatment conditions applied to thick films produce crystals with different morphologies to those formed in thinner films.

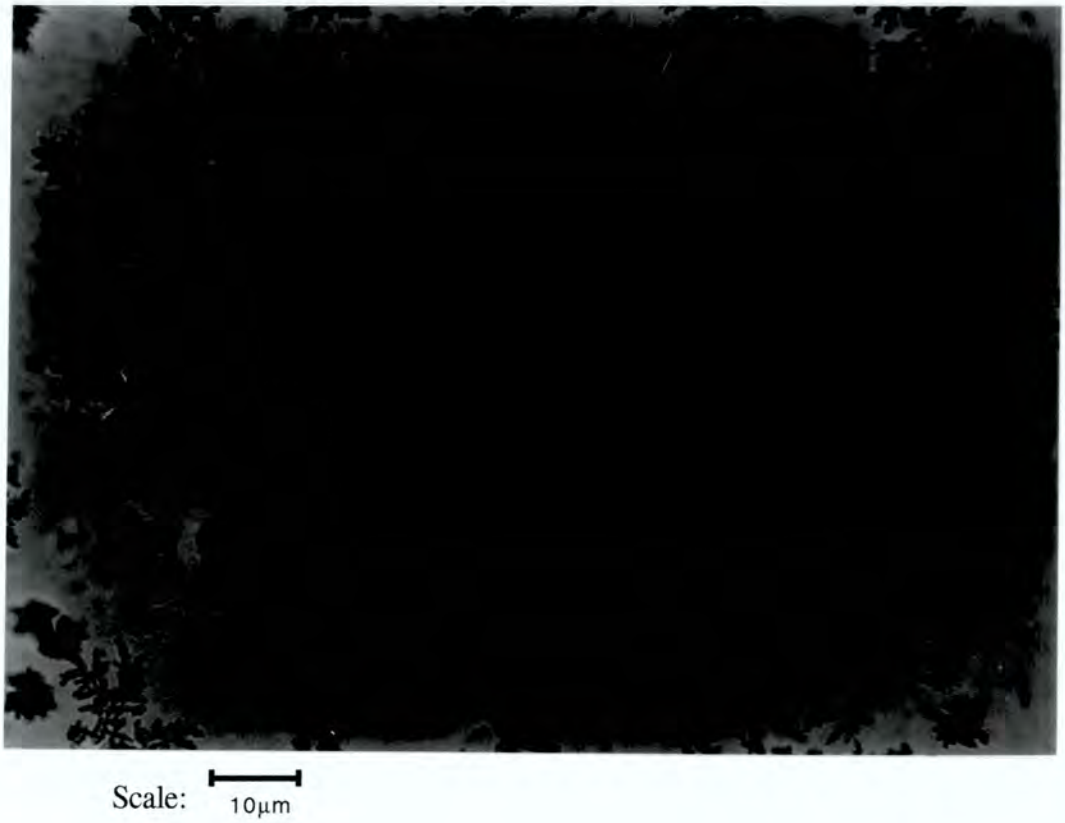

Figure 5.23 Optical micrograph of a thick (~100 μm) film of K(TCNQ) doped PMMA film treated with dichloromethane (300 mb, 2 min)

In the case of the vapour treated Li(TCNQ) films discussed in sections 5.1.1 and 5.1.2, the position of the CT band in the dichloromethane vapour treated film suggests that in contrast to the case of Rb, Na and K salts the film contains approximately spherical shaped crystals as in the case of the KBr disc spectra. Treatment with acetonitrile vapour treatment seems to lead to needle shaped crystals as indicated by the very low energy position of the CT peak.

5.5 Effect of screening on CT band

Recently an alternative mechanism capable of producing shifts in the position of the CT peak of the alkali metal TCNQ salt absorption spectrum was proposed by Papavassiliou (1992). Shifts of the CT band to higher energy were noted as the size of microcrystals decreased. Different sizes of crystallites were produced using mechanical grinding of salt crystals. Applying the Hubbard model (see Chapter 3), to a cluster of four molecules with four electrons demonstrated that such shifts could be attributed to the increase of the on-site Coulomb repulsion due to less effective screening in smaller crystallites. Assuming an overlap integral t=0.2 eV, a shift of the CT band from 1.1 eV to 1.5 eV was predicted as the on-site Coulomb repulsion, U was varied from 1.15 eV (assumed typical for normal bulk material) to 1.5 eV. Whilst these shifts are of the same order as observed in the vapour treated films described in the present work, the fact that the shifts are seen even for films containing relatively large (1 μm) microcrystals imply that this mechanism for U enhancement cannot apply here. A crystallite size of less than 25 nm is required to produce such shifts in the energy of the CT peak. It is however possible that the 1 μm crystals observed in the films described above could in fact consist of clusters of much smaller basic units. Once again better observation techniques need to be found to visualise the crystallites to determine if this is the case.

5.6 Heat treated films

Films which have undergone heat treatment to induce crystallisation produce interesting absorption spectra. Furthermore the crystallites produced are of a size (see Figure 4.6) which allow determination of their shape. The absorption spectrum of a K(TCNQ) doped PMMA film following heat treatment at 120 C is shown in figure 5.24.

The CT absorption peak occurs at a relatively high energy of 1.5 eV. The crystallites in the film are of too large a size to allow quantitative application of Mie-Gans theory. However qualitatively one might expect that the basically branched needle-like structure of the crystals in the film would produce a longer wavelength CT absorption than that actually observed. This suggests some other mechanism is responsible for the high energy position of the CT band in these films.

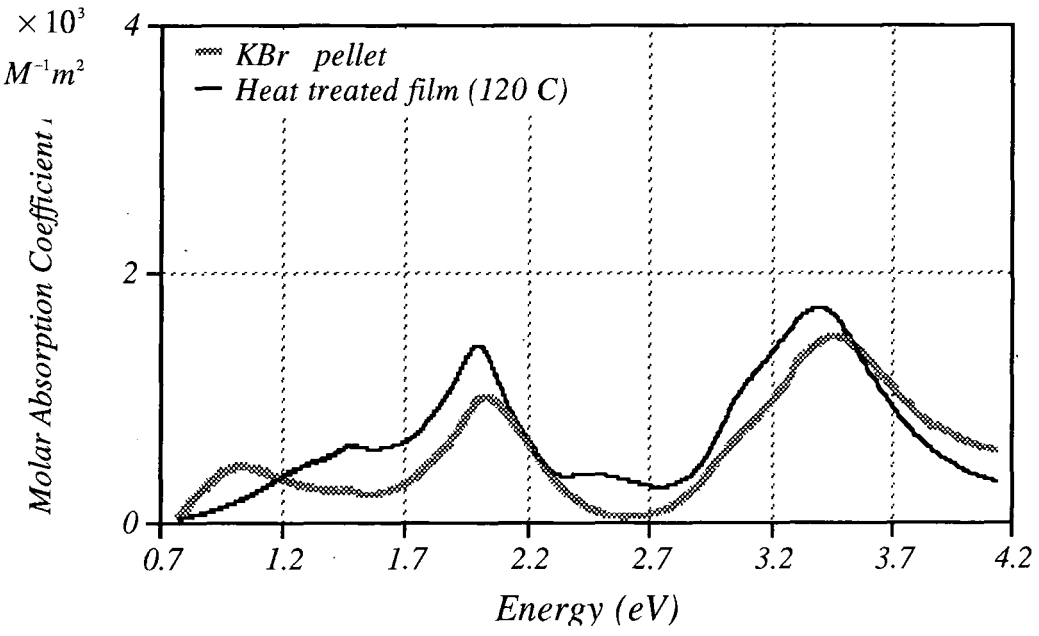

Figure 5.24 Absorption spectra of K(TCNQ) dispersion (heat treated)

The relatively large size of microcrystals within the film rule out the small crystal size, U enhancement mechanism of Papavassiliou as an explanation for the high energy position

of the CT band, and the underlying reason for its position remains unresolved.

5.7 Discussion

The two main points of interest arising from linear absorption measurements are firstly the fact that virtually 100% conversion from molecularly dispersed phase to microcrystalline phase is possible using either a vapour or heat treatment technique. Secondly shifts are seen in the position of the CT band in the spectra of thin film dispersions of TCNQ salts compared to both bulk crystal spectra and to dispersions of the salts in KBr discs. In this respect the behaviour of the three salts Na(TCNQ), K(TCNQ), Rb(TCNQ) is different to that of Li(TCNQ): In the case of Na, K and Rb salts thin film dispersions exhibit *shorter* wavelength CT peaks than dispersions of the same salt ground and pressed into a KBr pellet; in the case of Li(TCNQ) thin film dispersions formed following vapour treatment with non-solvents and containing sub-optical crystals, exhibit CT peaks *coincident* with those of dispersions of the salt in KBr discs. Films containing larger Li(TCNQ) crystals, following treatment with moderate salt solvents such as acetonitrile actually exhibit a CT peak shifted to *longer* wavelength

Three mechanisms have been put forward which could be responsible for the observed shifts in the position of the CT peak. The first and perhaps most plausible is that the shifts in the CT band are related to the shape of crystallites within the dispersions according to Mie-Gans theory. The theory predicts that for films containing disc shaped crystallites the CT band has a short wavelength position, that needle-like crystals produce a longer wavelength CT band whilst spherical crystals give rise to a CT band of intermediate position. If this is the correct explanation of the shifts seen in this work we must propose first of all the existence of approximately spherical crystals in KBr disc dispersions. Secondly we must propose that vapour treatment with non-salt-solvents results in different crystal shapes when applied to films containing Rb, K and Na salts (discs) as opposed to films containing Li(TCNQ) (spheres). Further, the long wavelength position of the CT

band in Li(TCNQ) films, vapour treated with moderate-salt-solvents such as acetonitrile could be explained as being due to the predominance of needle shaped crystals. It is certainly possible that the grinding applied to salt crystals prior to dispersal in KBr pellets should result in crystals with average spherical shape and indeed Li(TCNQ) doped films exhibiting a long wavelength CT band do contain a large proportion of needle-like crystals. However, in the case of the films containing dispersions of Rb, K and Na salts with short wavelength CT bands, failure to determine the shape of the crystallites via TEM and X-ray methods means it is not possible confirm the presence of disc shaped crystals.

Whilst the effect of crystal shape can explain the position of the CT band, problems do arise when using Mie-Gans theory to predict the strength of the absorption bands: Detailed calculations were only carried out for dispersions of K(TCNQ) in PMMA as the required values of dielectric function was only available for this salt. The weakness of the CT band and strength of the LE1 bands are such that one needs to assume a high degree of alignment of microcrystals with their TCNQ stacking axes, (the short axis in disc shaped crystals), perpendicular to the plane of the film, in order to produce reasonable quantitative fits. There can be no ready explanation for such a preferential alignment. Indeed, such alignment is not supported by refractive index measurements (see Chapter 6) which suggest homogeneous distribution of crystals within the treated films. Thus, although the spectra of Na, K and Rb salts can be explained by assumption of disc shaped crystals with a high degree of alignment, as yet, no supporting evidence of either shape or alignment has been found.

The second mechanism that has been suggested for giving rise to shifts in the position of the CT band is a reduction in the degree of screening of the Coulombic interaction between electrons giving rise to an increase in the on-site Coulomb repulsion U. This would simultaneously raise the transition energy associated with the CT band and reduce the oscillator strength of the transition, as described in chapter 3. In this work such shifts are observed even for films containing crystals of micron scale. Thus if one is to adopt the

enhanced U mechanism to explain the spectral shifts one must either assume that the micron scale structures observed in certain films are in fact made up of clusters of much smaller crystals, or one must seek some mechanism of U enhancement other than the effect of crystal size.

Finally one might seek to explain the shifts in the position of the CT band as being due to differences in crystal structure in the various dispersions. Although there is no direct evidence of such a structural difference, rapid crystallisation in the highly viscous environments prevailing during phase separation has been found to effect the electronic properties of certain charge transfer salts. For example N-propyl-phthalazinium-tetracyanoquinodimethane ($PrPht(TCNQ)_2$), formed in poly(bisphenol-A)carbonate using the reticulate doping method (see chapter 1), was found to have higher conductivity and lower activation energy (smaller band gap) compared to bulk samples of the salt (Tracz 1988), due possibly to differences in the crystalline structure of the two forms. In addition tetrathiotetracene (TTT), and TCNQ in polycarbonate forms dendritic crystals with a 1:1 stoichiometry rather than the 1:2 normally exhibited (Tracz 1986). Bearing these results in mind one could explain the short wavelength position of the CT band in certain films as being due to the microcrystals taking on a structure where the separation of TCNQ molecules within the stack is larger than that in normal bulk material. This would lead to a decrease in the degree of π-orbital overlap, and a reduction in the bandwidth 4t. This would in turn lead to a shift of the CT absorption band to higher energy and to a reduction in its oscillator strength (see chapter 3, section 3.4.2), as was in fact found.

Clearly it is important that means of determining crystallite size, shape and orientation are found if the reasons for the observed spectral shifts are to be clarified.

Chapter 6

Film Refractive Index Measurements

6.1 Introduction

This chapter describes refractive index measurements carried out on composite films and uses them to determine the dielectric constant of the crystals within the film. This method is applied to PMMA films containing crystals of the alkali metal salts of TCNQ. In the case of K(TCNQ) the results are compared to the dielectric function of the bulk material, taken from the literature as determined by Kramers-Kronig analysis of optical reflection data. Attempts are then made to explain the results in terms of the shape and orientation of the crystals within the films.

6.2 Prism coupling technique

The refractive indices of undoped polymer films and composite films can be measured using prism coupled waveguiding techniques. For undoped and therefore low loss films a two prism method can be employed. The set-up (assembled by P.K.Sharma at Durham University), is illustrated in figure 6.1. Details of the theory relating to this method have been given by Tien (1971). Light is coupled into the film via the input prism A and propagates through the film until it reaches the second, output prism B which allows the

light to couple out of the film. The waveguide only 'accepts' light incident at specific angles.

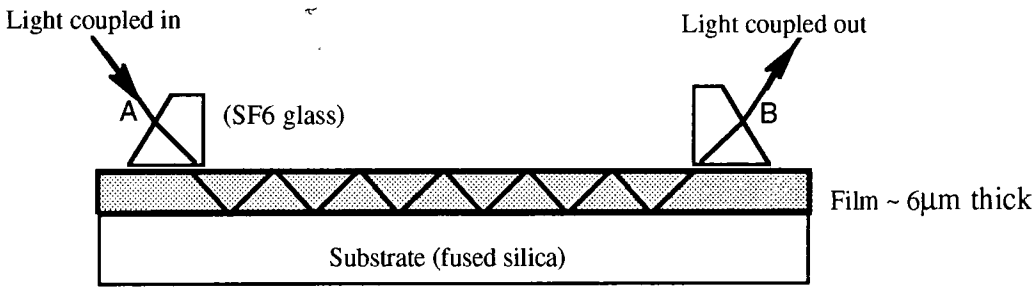

Figure 6.1 Prism coupling method for waveguiding

When light is incident at such an angle it is able to couple into the film and to propagate through it as a guided mode, possessing a characteristic intensity profile and mode velocity, until it emerges at the second prism. Only when the incident light is directed at one of these characteristic angles will an output beam be observed. For other angles, light is not able to propagate through the film and so no output beam emerges from prism B. The angles for which light is accepted by the waveguide depend on film thickness and refractive index, and on the refractive index of the substrate.

The guided modes can be described as either TE or TM depending on whether it is the electric or magnetic field which lies in the plane of the film (see figure 6.2). The experimental technique consists of illuminating the prism/film interface with light polarised so as to excite either TE or TM modes. The angles of incidence, ϕ, (see figure 6.3), which give rise to guided modes and hence a resultant output beam are measured. From these angles, a corresponding mode angle, β , (see figure 6.3), is determined.

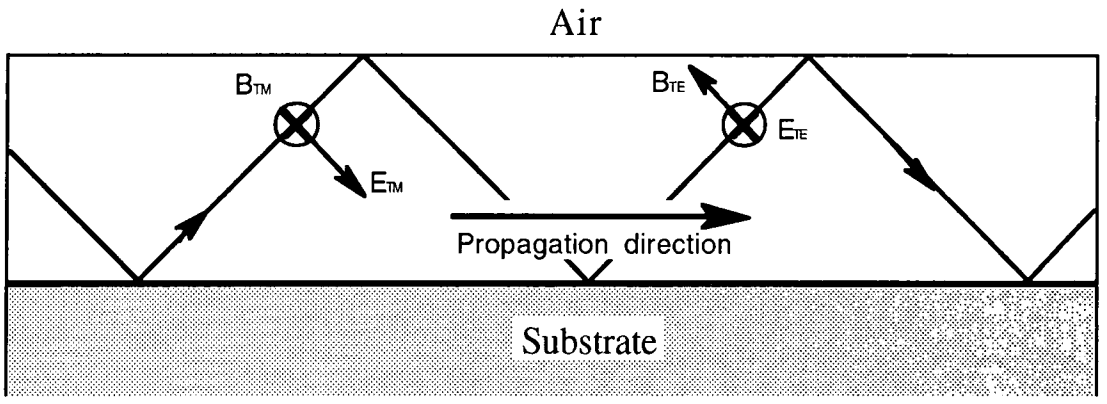

Figure 6.2 TE and TM modes in a waveguide

Having measured the allowed mode angles, it is possible to calculate and plot, which film thickness/refractive index combinations would produce a waveguide capable of supporting such a mode. If three or more mode angles are determined for a particular film and the possible refractive index/thickness values are plotted for each mode, the curves should meet at a point, corresponding to the actual values of these parameters in the film. One such plot is shown in figure 6.4

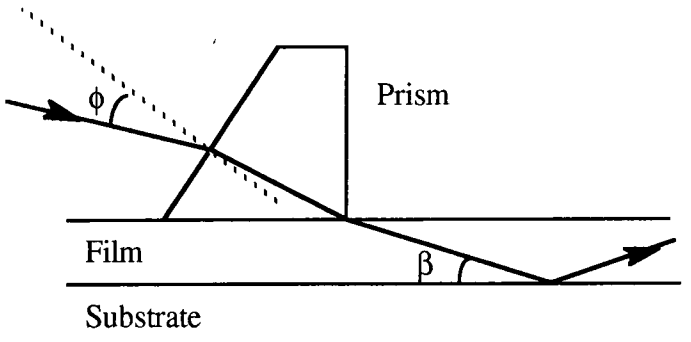

Figure 6.3 Prism coupling of light into a waveguide

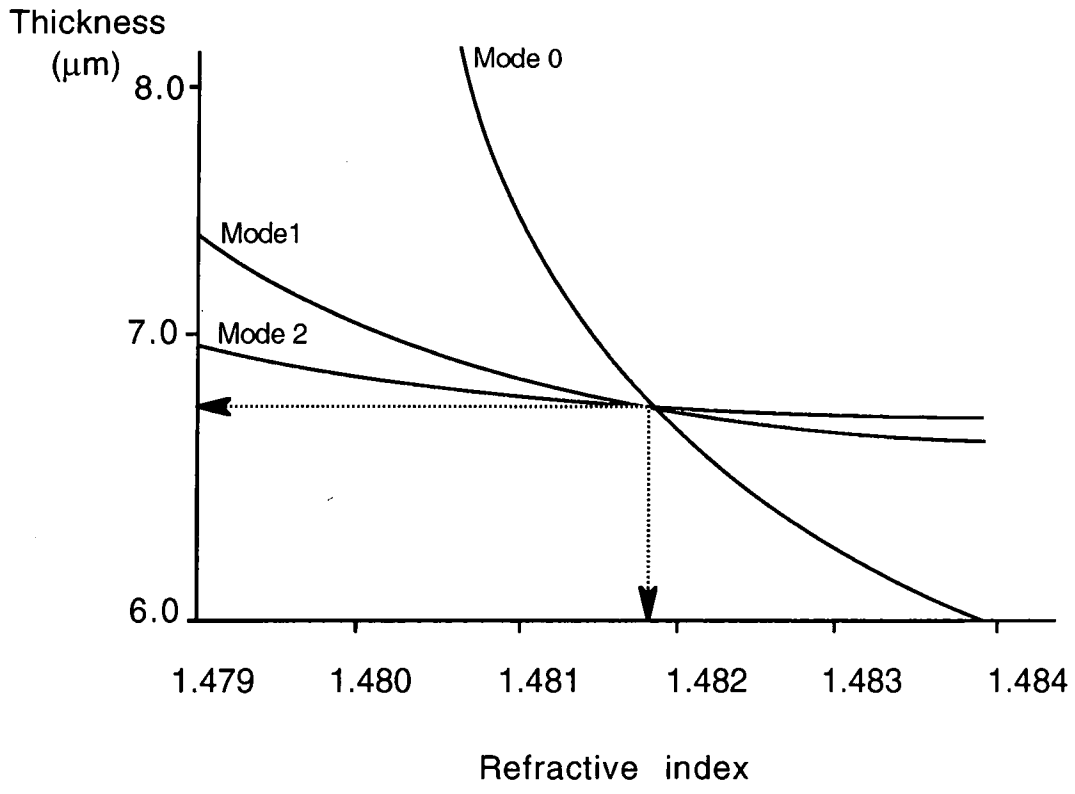

Figure 6.4 Determination of film refractive index and thickness

6.3 M-Line technique

The method described above works well for low loss films where a significant amount of light emerges from the output prism. For lossy films an alternative though essentially very similar technique can be employed (Tien and Ulrich 1970).

The method has become known as the M-Line Technique. The set up is sketched in figure 6.5. Instead of observing the beam after traversing the film and coupling out via a second

prism, the reflected light from the prism/air gap interface is observed. Again the waveguide will only accept light directed at specific incident angles. At other angles the beam is totally reflected by the prism base. When the incident angle corresponds to a mode angle, the intensity of the reflected light drops markedly. These dips in the reflected beam intensity, can be detected and imaged on a screen.

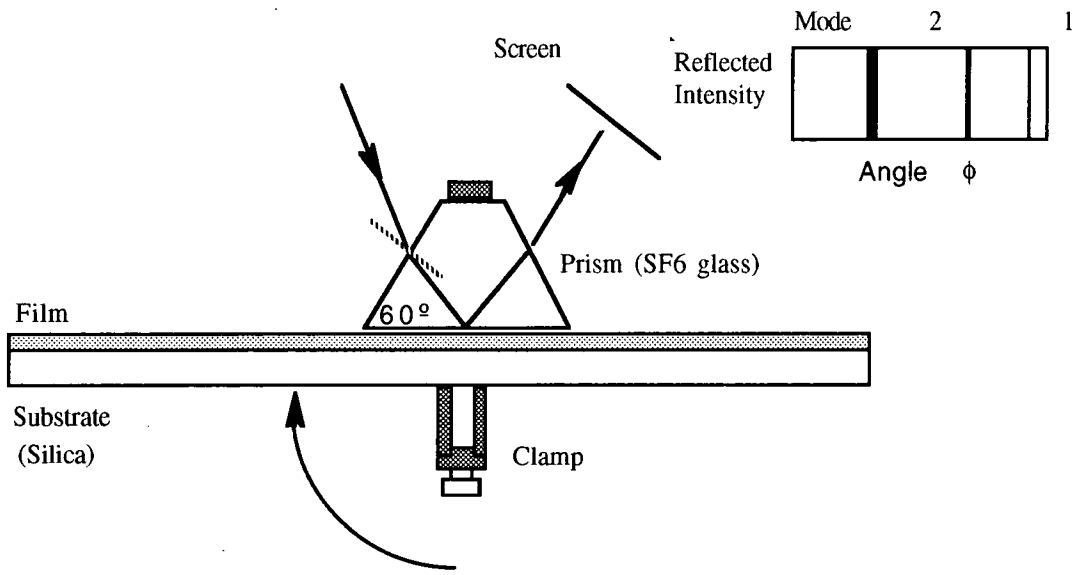

Figure 6.5 Experimental set-up for M-Line technique

The same analysis as in the two prism method is used in determining the film refractive index and film thickness.

6.4 Results

The results of refractive index measurements carried out using a diode laser emitting 1300 nm wavelength radiation, are shown in table 6.1. Measurements carried out on composite films employed the M-Line technique. The measurement on undoped PMMA

films used the two prism method. In both cases an infra-red camera was used to view the beam. Also given in table 6.1 are the absorption coefficients α and extinction coefficients k (see section 6.5), determined from the linear absorption spectra

Salt	Crystallite size	Volume fraction of salt in film %	α_{1300} x10^3m-1	k_{1300} x10-3	refractive index TE	TM
Na(TCNQ)	Sub-optical	1.56	16.5	1.7	1.4930±0.0002	1.491±0.002
Vapour treated	1-2μm	1.56	30.1	3.2	1.487±0.002	1.488±0.004
K(TCNQ)	Sub-optical	1.74	15.1	1.6	1.488±0.0002	1.488±0.002
vapour treated	1-2μm	1.74	25.0	2.6	1.4870±0.0004	1.487±0.003
heat treated	5μm	1.74	20.1	2.2	1.488±0.004	1.486±0.002
Rb(TCNQ)	Sub-optical	1.57	9.90	1.0	1.4890±0.0005	1.486±0.002
vapour treated	1-2μm	1.57	12.6	1.3	1.4870±0.0003	1.488±0.002
Undoped PMMA	-	-	-	-	1.4822±0.0003	1.4824±0.0003

Table 6.1 Results of refractive index measurements at 1300 nm

6.5 Calculation of dielectric constant

Using the information in table 6.1 it is possible to calculate the dielectric constant of the microcrystals within the composite film as described below.

The dielectric constant, ε of a homogeneous isotropic medium can be expressed by

$$\varepsilon = \left(n^2 - k^2\right) + i2nk \tag{6.1}$$

where n is the real part of the refractive index of the medium and k is the extinction coefficient. k is related to the absorption coefficient α at wavelength λ by

$$k = \frac{\lambda\alpha}{4\pi} \tag{6.2}$$

Thus the value of k can be calculated from the linear absorption spectrum. Substitution of the experimental values of k and n into 6.1 yields the effective dielectric constant of the film.

The effective dielectric constant of a composite medium ε^*, can be related to that of its components using the approach of Maxwell-Garnett (1904). It is found that ε^*, depends on the dielectric constants of the host ε_1, that of the dopant ε_d and the volume fraction q, of the dopant. In addition ε^* depends on the morphology of the crystals within the composite. Smith (1977) considered two cases. The first corresponds to a system of isolated crystals within the composite having average spherical shape and which are randomly distributed (see figure 6.4a). In this case the relationship between the dielectric constant of the two components and the effective value measured experimentally is

$$\frac{\varepsilon^* - \varepsilon_1}{\varepsilon^* + 2\varepsilon_1} = q\frac{\varepsilon_d - \varepsilon_1}{\varepsilon_d + 2\varepsilon_1} \tag{6.3}$$

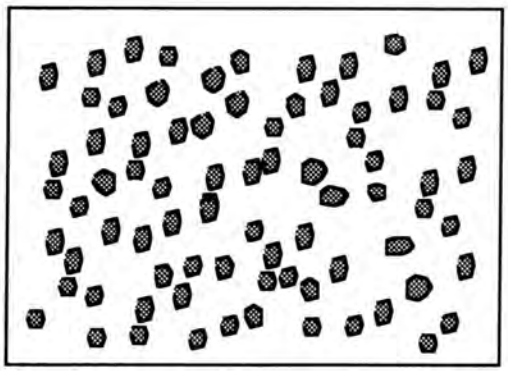

Figure 6.4a
Dispersed crystals with average spherical shape.

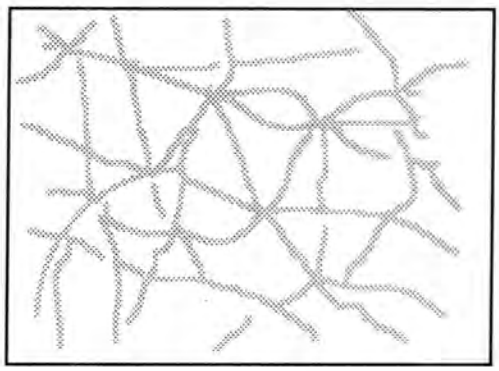

Figure 6.4b
Dispersed crystals forming filamental structure.

The second case treated by Smith is one where the host (in this case the polymer), is broken up, by a filamental crystal network, into islands having on average a spherical shape (see figure 6.4b). In this case the relationship between the dielectric constant of the two components and the effective value measured experimentally is:

$$\varepsilon^{*} = \varepsilon_{d}\left(\frac{3\varepsilon_{1} - 2q(\varepsilon_{1} - \varepsilon_{d})}{3\varepsilon_{d} + q(\varepsilon_{1} - \varepsilon_{d})}\right) \qquad (6.4)$$

Cohen (1973), considered the case of discs aligned with their short axes perpendicular to the electric field. This would correspond to the case where TE modes are used to probe films containing disc shaped crystals, aligned with their short axes perpendicular to the plane of the film (i.e. as suggested by the linear absorption spectra of thin film dispersions of Na, K and Rb(TCNQ) on the basis of Mie-Gans theory, in chapter 5). In this case the equation relating the dielectric constant of a composite medium to that of its components is

given by

$$\frac{\varepsilon^* - \varepsilon_1}{\varepsilon_1} = q\frac{\varepsilon_d - \varepsilon_1}{\varepsilon_1} \qquad (6.5)$$

PMMA exhibits negligible absorption in the 1300 nm region thus k_1 can be neglected and ε_1 can be approximated as n_1^2 where n_1 is the refractive index of the polymer (see equation 6.1). By substituting the measured values of ε_1, ε^* and q, into equations 6.3, 6.4 and 6.5 and in each case, equating the real and imaginary parts of the left and right-hand sides, each model yields two easily soluble simultaneous equations in which the unknowns are the real and imaginary parts of ε_d.

The results obtained on the basis of the three models described above, are given in table 6.2

		Model					
Salt	Crystallite size	spherical crystals		aligned, disc crystals		filamental crystals	
		$Re(\varepsilon_d)$	$Im(\varepsilon_d)$	$Re(\varepsilon_d)$	$Im(\varepsilon_d)$	$Re(\varepsilon_d)$	$Im(\varepsilon_d)$
Na(TCNQ)	Sub-optical	4.4	0.58	4.26	0.33	4.2	0.64
(vapour treated)	1-2μm	3.4	0.87	3.11	0.61	3.4	0.76
K(TCNQ)	Sub-optical	3.3	0.38	3.2	0.27	3.3	0.34
(vapour treated)	1-2μm	3.1	0.57	3.0	0.44	3.1	0.53
K(TCNQ)	5μm	3.3	0.52	3.2	0.38	3.3	0.46
(heat treated)							
Rb(TCNQ)	Sub-optical	3.5	0.27	3.5	0.19	3.4	0.23
(vapour treated)	1-2μm	3.5	0.35	3.1	0.25	3.3	0.27

Table 6.2 Calculated dielectric function of TCNQ salt microcrystals in PMMA films

6.6 Discussion

Within experimental error TE and TM modes yield the same value for ε^*, the effective dielectric constant of the film. All three proposed crystallite morphologies models yield similar values of ε_d, the dielectric constant of the dispersed crystallites. The similarity of the values of ε_d calculated on the basis of three quite different morphologies suggests that in the 1300 nm wavelength region, and at these low doping levels, the dielectric properties of the composite film are fairly insensitive to crystallite shape. $Im(\varepsilon_d)$ is found to be slightly greater in larger crystals than in smaller crystals. This may be due to the measurements of α being over estimated because of the effects of light scattering, in films containing larger crystals. This would lead to k_d and hence $Im(\varepsilon_d)$ being overestimated. In the case of Na(TCNQ) doped films, smaller crystals are found to have a slightly greater value of $Re(\varepsilon d)$ than larger crystals though this does not seem to be the case for K(TCNQ) and Rb(TCNQ).

Data from reflectivity measurements of Papavassiliou (1979), which is given in appendix 3, indicates that at 1300 nm bulk K(TCNQ) has a dielectric function with $Re(\varepsilon_z) = 0.2$ and $Im(\varepsilon_z) = 7.48$ parallel to the TCNQ axis; $Re(\varepsilon_x) = Re(\varepsilon_y) = 3.16$, $Im(\varepsilon_x) = Im(\varepsilon_y) = 0.44$ perpendicular to the TCNQ axis. Thus when considering dispersions of these materials ε_d refers to a weighted average value dependent on the orientation of the crystallites and on whether TE or TM modes are being used in its determination.

The fact that in K(TCNQ) films the refractive index measured by TE modes is the same as that measured by TM modes suggests an isotropic medium. This would require a random orientation of crystallites within the film. In that, case one might expect ε_d to be a simple

average of the dielectric function in the three principal directions:

$$\varepsilon_d = \frac{\varepsilon_x + \varepsilon_y + \varepsilon_z}{3} \qquad (6.6)$$

With the values of dielectric function given above for K(TCNQ), at 1300 nm equation 6.6 yields $Re(\varepsilon_d) = 2.17$, $Im(\varepsilon_d) = 2.79$. This is not in good agreement with the measured value of ε_d in table 6.2. If one is to reconcile these results with a random distribution of crystallites one must assume that the dielectric constant of microcrystalline material is different to that of bulk material. Since the electronic properties of these salts parallel to the TCNQ stacking axis are dominated by charge transfer process, in contrast to those perpendicular to this axis which are dominated by local excitations associated with individual TCNQ ions, (see chapter 3), one might expect ε_z to be most sensitive to crystallite morphology. Assuming that ε_x and ε_y remain unchanged from their bulk values it is possible to use equation 6.2 to calculate the value of ε_z which leads to agreement with the calculated and measured values of ε_d. In the case of the K(TCNQ) film containing sub-optical crystallites (see table 6.2), assumption of spherical crystallite morphology yielded a value of $\varepsilon_d = 3.3 + \mathbf{i}\ 0.38$ Use of equation 6.6 reveals that a value of $\varepsilon_z = 3.6 + \mathbf{i}\ 0.26$, for the microcrystalline material, leads to agreement with the measured value of ε_d. Thus we can explain the measurements on the basis of a random distribution of crystallites, by assuming that the microcrystals have dielectric properties significantly different to that of bulk material, with a much reduced imaginary component and a much enhanced real component.

If instead we assume the bulk values of dielectric constant hold for the microcrystals, we might attempt to explain the measured values of ε_d by assuming the crystals are oriented with their TCNQ axes perpendicular to the plane of the film. In that case, for TE modes, the associated electric field would be directed perpendicular to the TCNQ axis of the

crystallites and ε_d would take on the value of the dielectric constant of the crystals perpendicular to the TCNQ axis i.e. Re(εd) = 3.16, Im(εd) =0.44 (see appendix 3). This gives a much better fit to the experimental values. However on the basis of this distribution one would expect ε_d as determined by use of TM modes to be different to this, due to the electric field component directed along the TCNQ axis, which is associated with them. However no difference was in fact found.

Summarising, measurements with TE and TM modes suggest an isotropic medium. This can only be explained by assuming a random orientation of crystallites. However the actual measured values of dielectric constant are not consistent with this if one assumes the dielectric constant of the microcrystals is equal to that of bulk material. To provide a quantitative fit one requires alignment of TCNQ stacking axes perpendicular to the electric field for both TE and TM modes - an impossible situation. Thus one is led to the conclusion that either a large error has occurred in the experimental measurements or the values of the intrinsic dielectric constant of the crystallites, ε_d is significantly different to those of bulk material as measured by Papavassiliou.

Chapter 7

Intensity Dependent Transmission Measurements

7.1 Introduction

Under intense illumination, the transmission of a material can deviate significantly from that measured at lower intensities. Depending on the underlying absorption processes the transmission can increase (saturable absorption), or it can decrease (reverse saturable absorption), with increasing light intensity. Accurate measurement of the transmission/incident beam intensity relationship allows determination of the imaginary part of the third order susceptibility $\chi^{(3)}$. In the case of saturable absorption, the lifetime of the excited state involved in the absorption process can be calculated by assuming a two level model. This chapter describes how this technique was used to assess the nonlinear optical properties of PMMA films containing dispersions of microcrystals of the alkali metal salts of TCNQ.

7.2 Interaction of radiation with a nonlinear medium

Consider a time varying monochromatic field E(t), of frequency ω given by

$$E(t) = E(\omega)e^{-i\omega t} + E^{*}(\omega)e^{i\omega t} \qquad (7.1)$$

On interacting with a centrosymmetric material, such a field induces a polarisation P(t) having frequency components at the fundamental frequency ω, and at all odd multiples of +/-ω . P(t) is given by, (Boyd 1992).

$$P(t) = P_0 + \varepsilon_0\left(\chi^{(1)}E(t) + \chi^{(3)}E(t).E(t).E(t)+...\right) \qquad (7.2)$$

Where P_0 is the permanent polarisation present in the material in the absence of an optical field, $\chi(1)$ is the linear susceptibility, and $\chi(3)$ is the third order nonlinear susceptibility. Normally terms of higher than third order in E(t) are neglected. Note that in 7.2 and in all subsequent expressions, tensor notation is dropped for clarity and the use of single monochromatic beams is assumed.

Substitution of 7.1 into 7.2, followed by its expansion reveals that the component of P(t) oscillating at frequency ω is given by

$$P(\omega) = \varepsilon_0\left(\chi^{(1)} + 3\chi^{(3)}|E|^2\right)E(\omega) \qquad (7.3)$$

This is the component of interest in the present work since we are to measure changes in the optical properties (in fact the absorption properties), of the medium at the pump frequency only.

Inspection of 7.3 suggest that in analogy to the linear case, it is possible to define an effective dielectric constant by, (Duffin 1980)

$$\varepsilon_{eff} = 1 + \chi^{(1)} + 3\chi^{(3)}|E|^2 \qquad (7.4)$$

Thus the nonlinear term has led to a change in the dielectric constant δε, of the medium given by

$$\delta\varepsilon = 3\chi^{(3)}|E|^2 \qquad (7.5)$$

In contrast to the linear case then, ε_{eff} is intensity dependent because of the term in $|E|^2$

Again in analogy to the linear case the dielectric constant can be expressed in terms of an intensity dependent refractive index n_{eff} and extinction coefficient k_{eff} according to.

$$\varepsilon_{eff} = (n_{eff} + ik_{eff})^2 \qquad (7.6)$$

or alternatively $$\varepsilon_{eff} = \left(n_{eff} + i\frac{c\alpha_{eff}}{2\omega}\right)^2 \qquad (7.7)$$

where α_{eff} is the effective absorption coefficient of the medium. α_{eff} determines the attenuation of a beam of intensity I , with propagation distance z through the nonlinear medium, according to the equation

$$\frac{dI}{dz} = -\alpha_{eff} I \qquad (7.8)$$

In contrast to the linear case α_{eff} is intensity dependent and can be expanded as, (e.g. Wherrett 1982)

$$\alpha_{eff} = \alpha_1 + \alpha_2 I + \alpha_3 I^2 + \ldots \qquad (7.9)$$

where α_1 is the linear absorption coefficient and α_2 and α_3 are nonlinear absorption coefficients which may either positive or negative. In the subsequent analysis only the first two terms in 7.9 are considered as being significant.

In the MKS system of units the field intensity is defined as

$$I = 2n\varepsilon_0 c|E|^2 \qquad (W/m^2) \qquad (7.10)$$

thus by equating 7.7 and 7.4 and substituting for $|E|^2$ using 7.10, we obtain

$$n^2 - \frac{\alpha_{eff}^2 c^2}{4\omega^2} + i\frac{nc}{\omega}(\alpha_1 + \alpha_2 I) = 1 + \chi^{(1)} + 3\chi^{(3)}\frac{I}{2n\varepsilon_o c} \qquad (7.11)$$

where nonlinear refraction has been neglected, allowing n_{eff} to be approximated by the linear refractive index n.

Finally by equating the imaginary terms in I, in 7.11 we obtain.

$$\frac{2\varepsilon_0 n^2 c^2 \alpha_2}{3\omega} = \mathrm{Im}\chi^{(3)} \qquad (7.12)$$

The experimental techniques described below aim to determine α_2, and hence allow calculation of $\mathrm{Im}\chi(3)$. Firstly the case of saturable absorption is considered.

7.3 Saturable absorption

The term saturable absorption describes the decrease in the absorption coefficient (increase in the transmission), of a material as it is subjected to increasing incident light intensities. Saturable absorption has been widely studied. Organic dyes in solution (De Giorgio 1966), inorganic semiconductors (Miller 1981), multiple quantum wells (Miller 1982) and inorganic semiconductor doped polymers (Hilinski 1988) have all been investigated. This work represents the first measurements made on *organic* semiconductor doped polymers.

In addition to the imaginary part of $\chi(3)$, saturable absorption measurements can be used to

determine the lifetime of the excited state populated by the absorption process, as outlined below

7.3.1 Two level model of saturable absorption

This section describes the two level model of saturable absorption and how this can be used to explain the variation of intensity of a beam, traversing the medium described by this model. Absorption saturation is interpreted as being due to depletion of the population of the ground state. This depletion reduces the effective number of absorbers in the lower level leading to an increase in transmission. The intensity at which saturation effects become apparent is found to be governed by the spontaneous lifetime of the excited state. Theoretically, at sufficiently high intensities the transmission can approach unity, however sample damage generally occurs before this situation is reached.

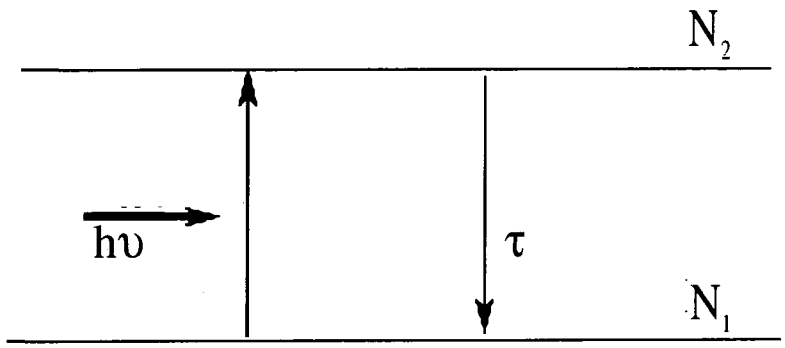

Figure 7.1 Two level system

In the two level model (depicted in figure 7.1), N2 is the population of upper level per unit volume, N1 is the population of the ground state per unit volume, N = N1+ N2, hυ is the

photon energy of incident radiation and τ is the spontaneous lifetime of the excited state.

When a light pulse of intensity I, is incident on such a system, the rate of change of the population of the upper level is equal to difference in the rate at which electrons are promoted from the lower level by induced absorption, and the rate at which the upper level population is depleted, by induced and spontaneous emission (Gires 1966).Thus the rate of change in the population N_2 may be written as

$$\frac{dN_2}{dt} = \frac{\sigma I(N_1 - N_2)}{h\upsilon} - \frac{N_2}{\tau} \tag{7.13}$$

where σ is the absorption cross section.

Provided the temporal width of the pulse is long in comparison to the lifetime of the excited state a pseudo equilibrium is established during the period of the pulse and in this case equation 7.13 can be set to zero. Under such steady-state conditions 7.13 yields

$$N_2 = \frac{N_1 + N_2}{2}\left(\frac{I}{I + I_c}\right) \tag{7.14}$$

where

$$I_c = \frac{h\upsilon}{2\sigma\tau} \tag{7.15}$$

I_C is termed the critical, or saturation intensity and is a measure of the intensity required to induce significant saturation in a material. Determination of I_C allows calculation of τ via equation 7.15.

It will now be shown how Ic can be related to the variation of the beam intensity passing through a material obeying the two level model, and hence can be used to calculate α_2 and $\mathrm{Im}\chi(3)$.

As the beam progresses, photons are continuously removed from the beam by induced absorption, and added to the beam by induced emission and spontaneous emission. However the photons emitted as a result of spontaneous emission are distributed in all directions so only a small fraction propagate in the direction of the incident beam. Hence their contribution to the forward beam can be neglected. Thus the net rate of depletion of the volume density of photons in the beam, ρ_p is given by

$$\frac{d\rho_p}{dt} = -\frac{\sigma I(N_1 - N_2)}{h\upsilon} \tag{7.16}$$

Using $\rho_p = \frac{I}{h\upsilon c}$ and $c = \frac{dz}{dt}$ (7.17)

we obtain:

$$\frac{dI}{dz} = -\sigma I(N_1 - N_2) \tag{7.18}$$

and, using the fact that $N_1 = N - N_2$, equation 7.18 becomes

$$\frac{dI}{dz} = -(N - 2N_2)\sigma I \tag{7.19}$$

Substituting 7.14 into 7.19 and rearranging, we obtain:

$$\frac{dI}{dz} = -\left(\frac{I_c}{I+I_c}\right)\sigma NI = -\left(\frac{I_c}{I+I_c}\right)\alpha_1 I \qquad (7.20)$$

where α_1, ($=\sigma N$), is the absorption coefficient at low intensity. 7.20 is a key equation which describes the attenuation of light passing through a medium obeying the two level model.

If we now write 7.20 in a slightly different algebraic form

$$\frac{dI}{dz} = -\alpha_1 I + \frac{\alpha_1}{I+I_c} I^2 \qquad (7.21)$$

comparison with equation 7.8 and 7.9 suggests that for small incident intensities such that $I_C >> I$ we can write

$$\alpha_2 \approx -\frac{\alpha_1}{I_c} \qquad (7.22)$$

Finally, use of equation 7.12 gives

$$\mathrm{Im}\,\chi^{(3)} = -\frac{2\varepsilon_0 n^2 c^2 \alpha_1}{3\omega I_c} \qquad (7.23)$$

Thus determination of I_C allows calculation of τ through 7.15, α_2 through 7.22 and $\mathrm{Im}\chi(3)$ through 7.23

7.3.2 Determination of Ic

Equation 7.20 expresses the dependence of beam intensity attenuation, on I_c, for a system obeying the two-level model. This relationship can be used to derive an equation (7.28), relating the experimentally measurable, energy transmission of a thin film, to Ic. The approach adopted is to assume a Gaussian incident beam profile, and to use 7.20 to calculate the profile of the emergent beam having traversed the thickness L of the film. It is then possible to use these profiles to calculate both the energy of the incident pulse and of the emergent pulse and hence the transmission of the sample.

For a Gaussian beam, the radial incident intensity distribution, $I_0(r)$ is given by

$$I_o(r) = I_p e^{-\frac{r^2}{w^2}} \qquad (7.24)$$

where I_p is the intensity in the beam centre, r is the distance from the beam centre, and w is the beam radius at which the beam intensity falls to 1/e of the peak intensity.

Substituting 7.24 into 7.20 we obtain an equation for the intensity profile of beam $I_z(r)$, after propagating a distance z into the sample:

$$\frac{dI_z(r)}{dz} = -\left(\frac{I_c}{I_z(r)+I_c}\right)\alpha_1 I_z(r) \qquad (7.25)$$

The intensity profile of the beam, $I_L(r)$, after traversing the entire length L of the film, can be obtained by integrating 7.25 with respect to z over the thickness of the film to give:

$$\frac{I_L(r)-I_0(r)}{I_c}+\ln\frac{I_L(r)}{I_0(r)}=-\alpha_1 L \qquad (7.26)$$

Equation 7.26 is transcendental and cannot be solved analytically. It can however be solved numerically to give $I_L(r)$ as a function of $I_0(r)$, α_1 and I_c, i.e.

$$I_L(r)=F\{I_o(r),I_c,\alpha_1\} \qquad (7.27)$$

In the experimental measurements described below the energy transmission, T, defined as the ratio of transmitted pulse energy to incident pulse energy are made as the intensity of the incident beam is varied. Thus for $I_0(r)$ given by 7.24

$$T=\frac{\Delta t\int_0^\infty 2\pi r I_L(r)dr}{\Delta t\int_0^\infty 2\pi r I_0(r)dr}=\frac{\int_0^\infty 2\pi r F\{I_0(r),I_c,\alpha_1\}dr}{\pi w^2 I_P} \qquad (7.28)$$

Where Δt is the temporal pulse width of the beam which is assumed to remain unchanged in traversing the film. The experimental data can be fitted to 7.28 with I_c the adjustable parameter. The analysis requires experimental determination of five parameters:

Ip and w : These parameters can be determined by measuring the incident beam's, spatial intensity profile, $I_0(r)$.

Δt : This can be measured directly using a photodiode and an oscilloscope with nanosecond resolution.

α_1 : This can be measured from the linear absorption spectrum

T : This is determined by measuring the ratio of the energy of the transmitted pulse to that of the incident pulse.

7.4 Experimental procedure for intensity dependent transmission measurements

7.4.1 Experimental set-up

The experimental set up for nonlinear absorption measurements is shown in figure 7.2. A Spectra Physics Q-switched, Nd:YAG pumped dye laser is used as the source. A KDP crystal converts the fundamental (1.064 μm) to second harmonic at 532 nm, which is used to pump the dye laser. The power incident on the sample is controlled using crossed polarisers and neutral density filters positioned as shown. Care is taken to maintain the polarisation of incident pulse during the measurements. Typical pump energies are 50 mJ at 532 nm, which are converted in the dye laser with around 2% efficiency. Typical temporal pulse widths are of around 5-7ns. To achieve high irradiances the beam is focused onto the sample using a 15 cm focal length lens, to a spot size of around 0.1 mm diameter at the sample.

Measurements were made in the 560 nm to 580 nm region using Exciton Rhodamine 590 dye and in the 750 nm region using Exciton LDS 750 dye.

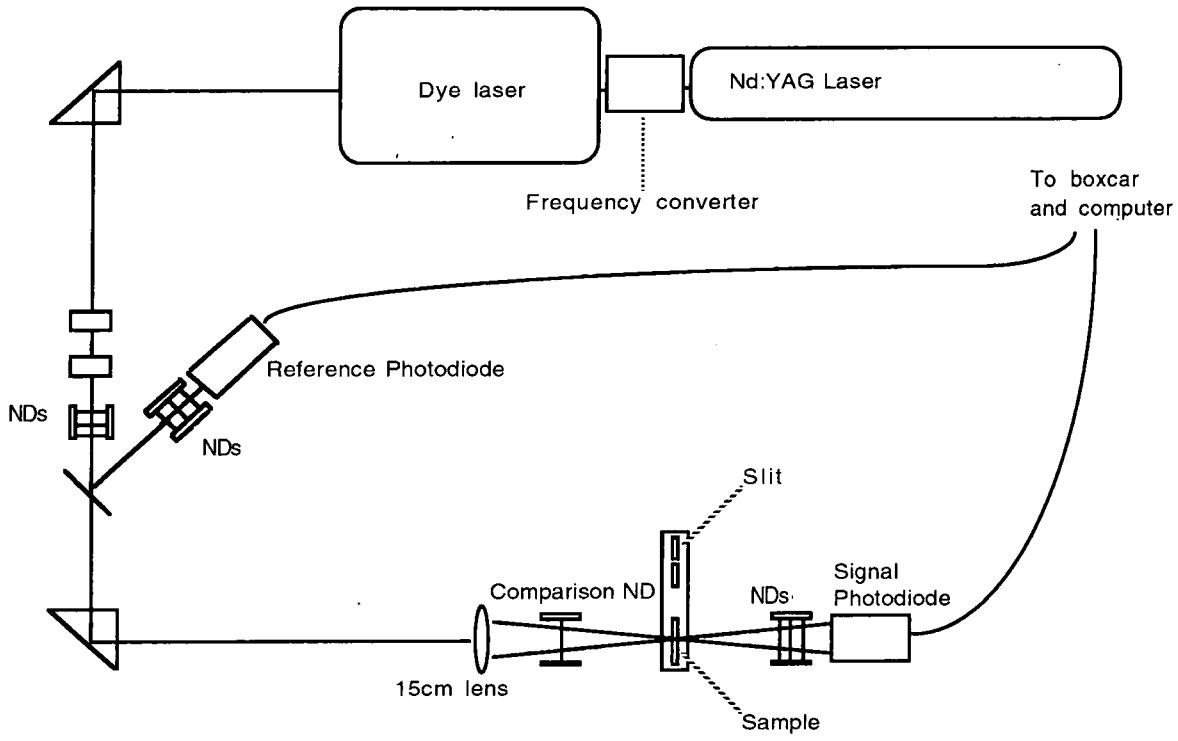

Figure 7.2 Experimental set up for saturable absorption

7.4.2 Measurement of pulse energy

Pulse energy is determined with photodiodes calibrated using a GENTEC thermopile detector. This device, which is itself calibrated by the manufacturers, generates a voltage signal proportional to the total energy of an incident light pulse. This signal can be measured directly on an oscilloscope. By measuring the corresponding signal produced by the photodiode for a large number of pulses, over a range of energies (adjusted using neutral density filters), the relationship between pulse energy and photodiode signal can be determined. The calibration must be carried out for each laser wavelength used as the

response of the photodiodes is wavelength dependent. The results of one such calibration are shown in figure 7.3.

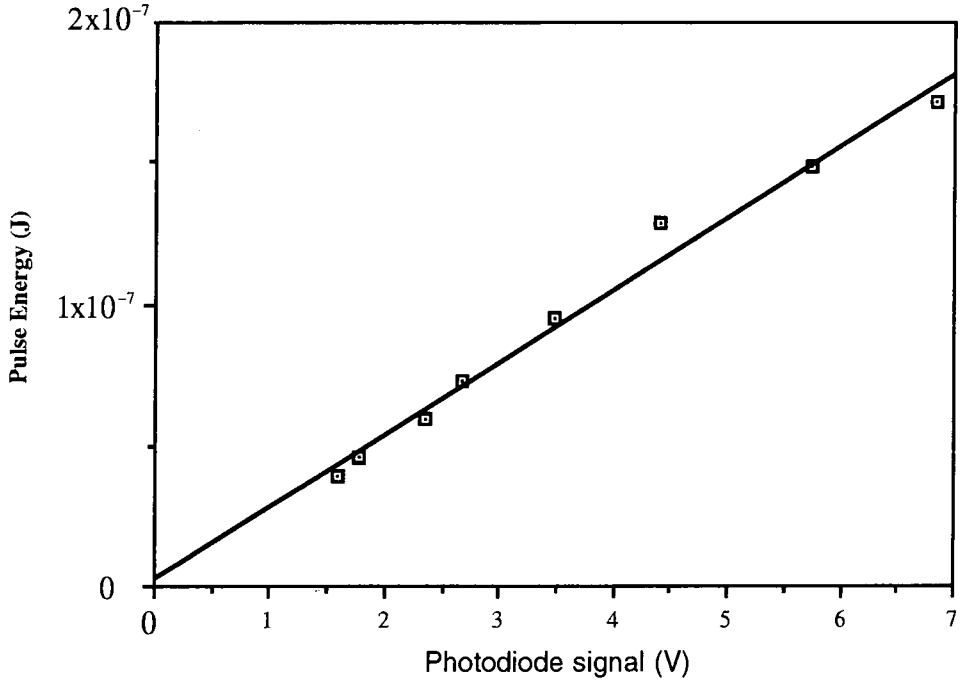

Figure 7.3 Photodiode calibration at 563nm

7.4.3 Measurement of spatial intensity profile of the incident beam

Having calibrated the photodiodes it is now possible to determine the spatial intensity profile of the incident beam, $I_0(r)$. This is done by first measuring the total energy of the pulse ϵ_T using the photodiode calibration curve, then measuring the temporal pulse width Δt. Finally the radius, w of the pulse at the 1/e maximum intensity point is determined. Use of equation 7.30 (see below) then allows determination of the peak intensity Ip.

For a Gaussian incident beam profile as given by 7.24 ϵ_T can be calculated by integrating

the beam profile with respect to space and time i.e.

$$\epsilon_T = \Delta t \int_0^\infty 2\pi r I_p e^{\frac{-r^2}{w^2}} dr \tag{7.29}$$

to give

$$\epsilon_T = \Delta t \pi w^2 I_p \tag{7.30}$$

To measure the temporal pulse width Δt, of the pulse the signal from the photodiode is displayed on a Tektronix 400 MHz analogue oscilloscope. Typically Δt is of the order of 6 ns.

To determine w, the photodiode signal is measured by passing a slit of length l, and of width greater than that of the beam, through the beam from a position where the beam is completely blocked ($-x_1$), to one, (x_2), where the entire beam is allowed to pass through the slit, (see figure 7.4)

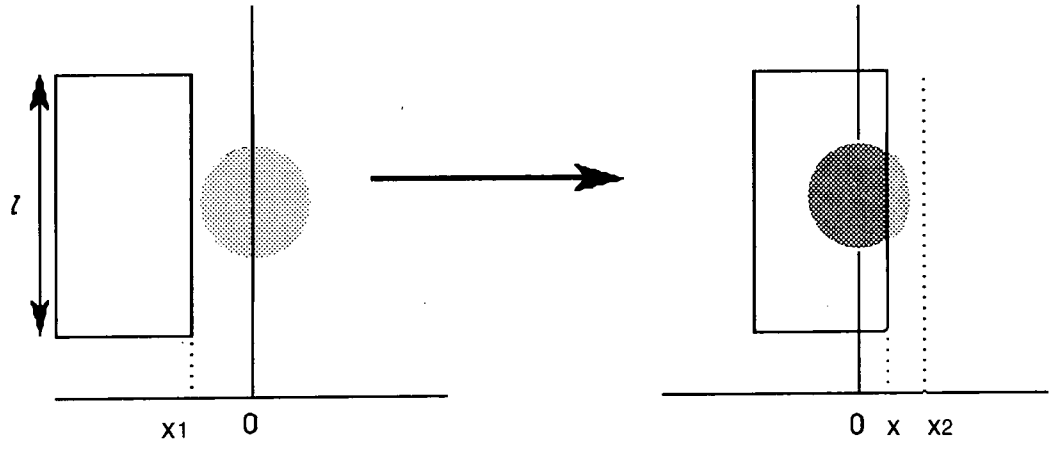

Figure 7.4 Determination of beam profile

The result of a typical measurement is shown in figure 7.5. The signal from the photodiode is converted into an energy value, $\epsilon(x)$, using the calibration curve shown in figure 7.3.

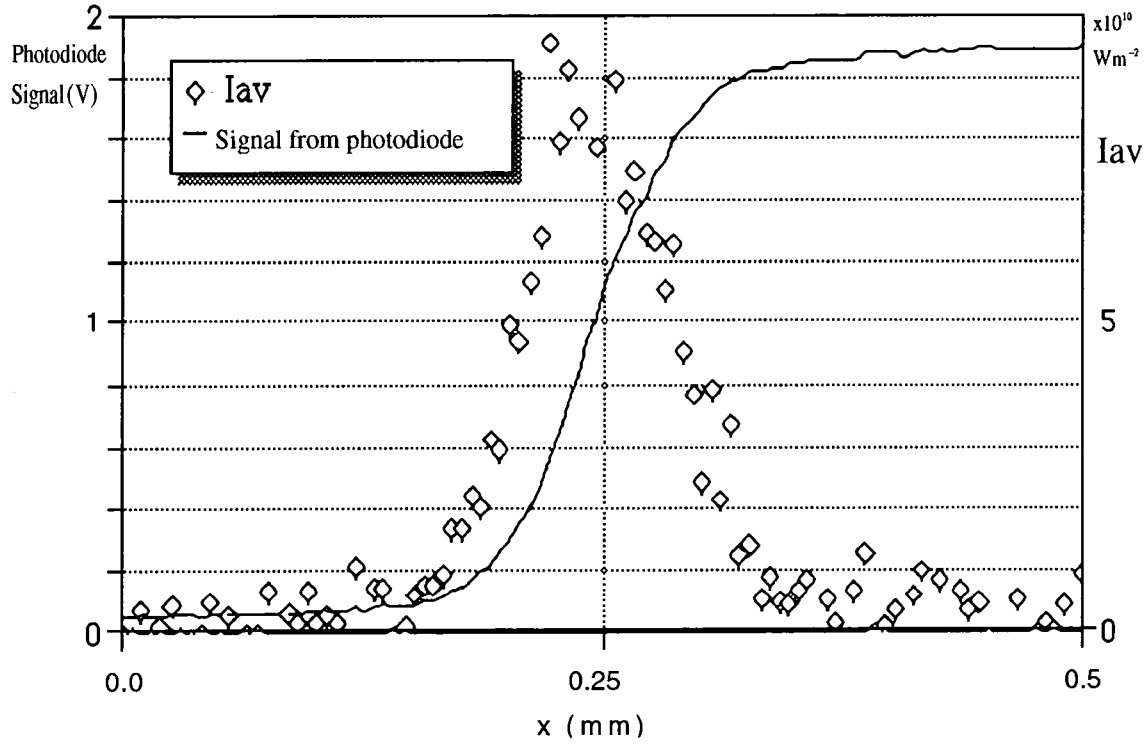

Figure 7.5 Variation of photodiode signal with slit position, and calculated spatial profile of average beam intensity, Iav

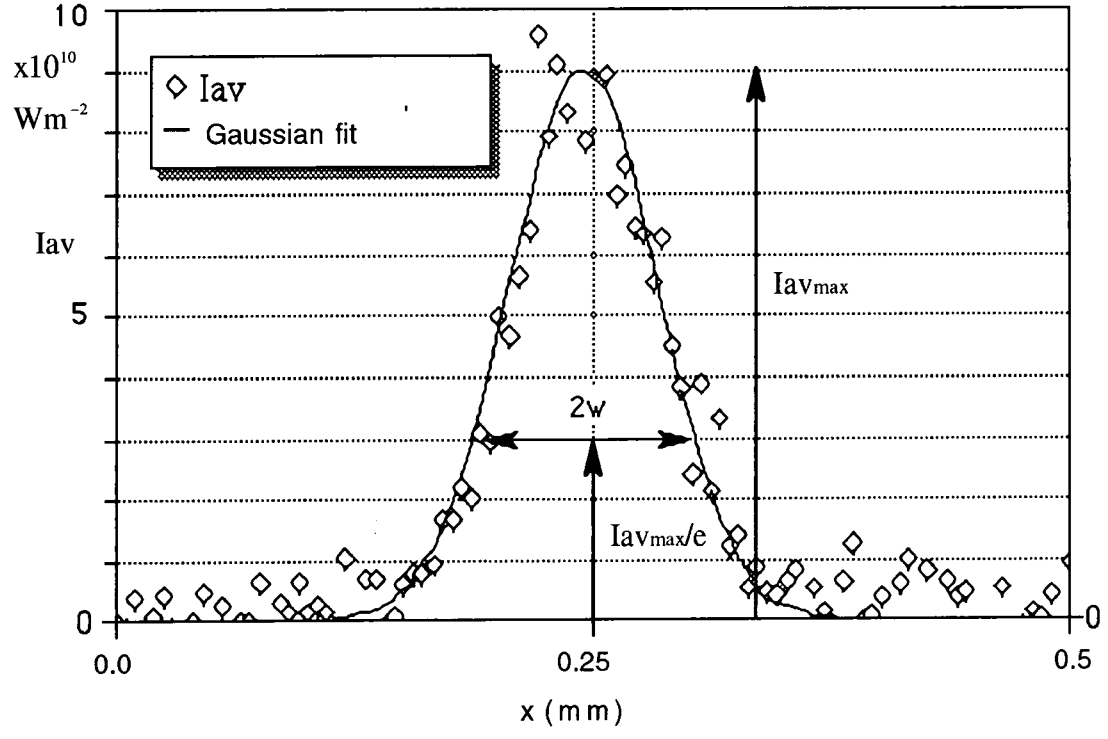

Figure 7.6 Calculated spatial profile of beam intensity and Gaussian fit

$\in(x)$ represents the total energy of the portion of the beam passing through the slit ,when the slit is at position x (see figure 7.4).Thus $\in(x)$ is given by:

$$\in(x) = \Delta t \int_{-x_1}^{x} I_{av}(x) l dx \tag{7.31}$$

Where $I_{av}(x)$ is the average intensity within the area $l.dr$ of the beam.

Thus
$$lI_{av}(x) = \frac{1}{\Delta t}\frac{d\in(x)}{dx} \tag{7.32}$$

Clearly by differentiating $\in(x)$ it is possible to determine the profile of $I_{av}(x)$, (see figure 7.5)

It can be shown (see appendix 5) that the 1/e radius of $I_{av}(x)$, which can be obtained by fitting a Gaussian profile to $I_{av}(x)$ (see figure 7.6), is equal to the 1/e radius w of the incident beam as expressed in 7.24.

Having thus measured $\in_T$, Δt and w, Ip is calculated from 7.30 and the incident beam profile (equation 7.24) can be calculated.

7.4.4 Measurement of sample transmission

For each value of peak incident intensity Ip, the corresponding energy transmission is measured in the following way: The reference normalised signal R_1, (transmission signal/reference photodiode signal), is measured for 100 pulses with the sample in the

beam. Then the same ratio, R_2 with the sample replaced by a calibrated neutral density filter of similar transmission, T_{ND} to the sample, is measured. The film's transmission T, is then calculated from

$$T = \frac{R_1}{R_2} T_{ND} \tag{7.33}$$

In measurement of the intensity dependence of the transmission care must be taken to ensure that the measured changes in the transmission are reversible thus ensuring they are due to the nonlinear properties of the material under scrutiny rather than the result of optical damage. This is best done by measuring the variation of transmission as the incident intensity is increased and then repeating the measurements as the intensity is decreased. If no damage occurs the variation of transmission obtained in each case should coincide. Inspection of films using an optical microscope can also be used to check for damage.

7.5 Analysis of saturable absorption data

The transmission of the sample is plotted as a function of Ip. Equation 7.28 is then fitted to the data with Ic the adjustable parameter. The analysis takes into account the variation in the effective absorption coefficient encountered by the beam as it passes through the sample, (in a nonlinear medium this is clearly a function of propagation distance), and also takes into account the dependence of nonlinear absorption on $I_Z(r)$. It does not take account of diffraction of the beam. This allows each part of the beam to be treated separately and the intensity profile of the emergent beam to be integrated to yield the output power. The fact that the samples are very thin, (<10 μm) in comparison to the diffraction length ($w^2/\lambda \sim 2$ cm) makes this assumption valid.

To illustrate the typical intensity dependence of film transmission, figure 7.7 shows the calculated variation of T with peak incident beam intensity I_p, for a range of I_c values, with $\alpha_1 L = 1.7$.

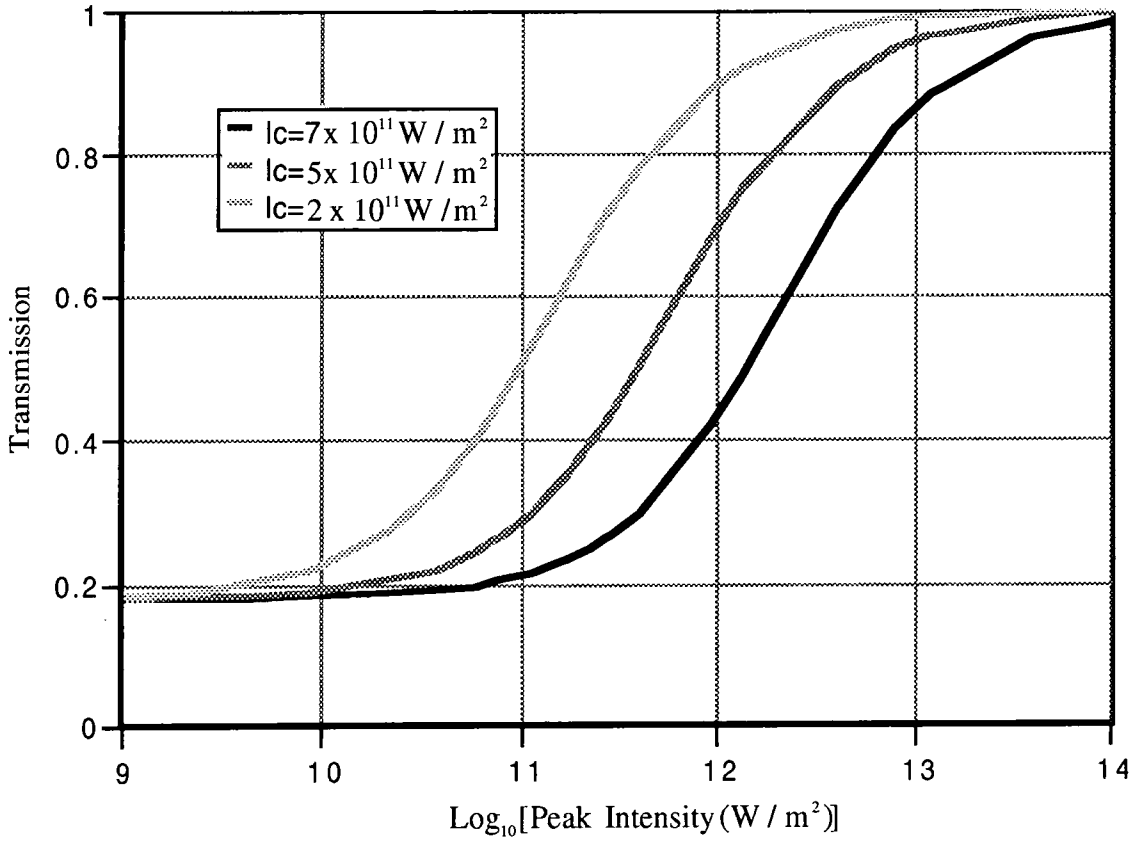

Figure 7.7 Variation of transmission with peak intensity for three values of Ic

7.6 Calculation of excited state lifetime and third order susceptibility

Having determined I_c the lifetime associated with the absorption process can be calculated from 7.15. The absorption cross section σ, of the microcrystals within the film can be determined from

$$\sigma = \ln\left(\frac{T_0}{LN}\right) \tag{7.34}$$

where T_0 is the transmission of the film at low intensity, (as measured on a spectrometer), L is the thickness of the sample and N is the number of absorbers per unit volume in the film.

In the wavelength region where saturable absorption was observed (563-577 nm), the absorption band is associated with a local excitation of the negatively charged TCNQ molecules in the crystallites within the film. Thus N is equal to the number of TCNQ molecules per unit volume in the film, which can be calculated from the concentration of salt in the initial solution from which the film was formed.

Equation 7.23 can be used to calculate $\mathrm{Im}\chi(3)$ of the film as a whole. To determine the value of $\mathrm{Im}\chi(3)$ for the crystallites within the film, one simply divides 7.23 by the volume fraction of salt in the polymer, *V* to give

$$\mathrm{Im}\,\chi^{(3)}_{\text{crystallites}} = -\frac{2\varepsilon_0 n^2 c^2 \alpha_1}{3\omega V I_c} \tag{7.35}$$

7.7 Results

Vapour treated films containing sub-optical crystals, and films containing crystals of 1-2μm diameter of Na(TCNQ), K(TCNQ) and Rb(TCNQ) dispersed in PMMA were studied. These films were formed using the methods described in chapter 4. The treatment vapour used was dichloromethane. Crystallite size was controlled by adjustment of the vapour

pressure used during the conversion process. In addition, heat treated films, containing interlocking networks of dendritic Na(TCNQ), crystals were investigated. Measurements were made using three wavelengths of incident radiation 563 nm, 570 nm and 577 nm i.e. on the high energy side of the LE1 absorption band, (see chapter 5).

Figures 7.8 to 7.10 show the experimentally measured variation of transmission with peak intensity for films containing crystallites of Na(TCNQ), K(TCNQ), Rb(TCNQ) of suboptical size, and for crystals of 1-2 μm diameter. Also shown in each plot are the best fits using equation 7.28 along with the corresponding values of I_c. The data refers to measurements made at 577 nm. Tables 7.1 to 7.4 summarise the results of these measurements.

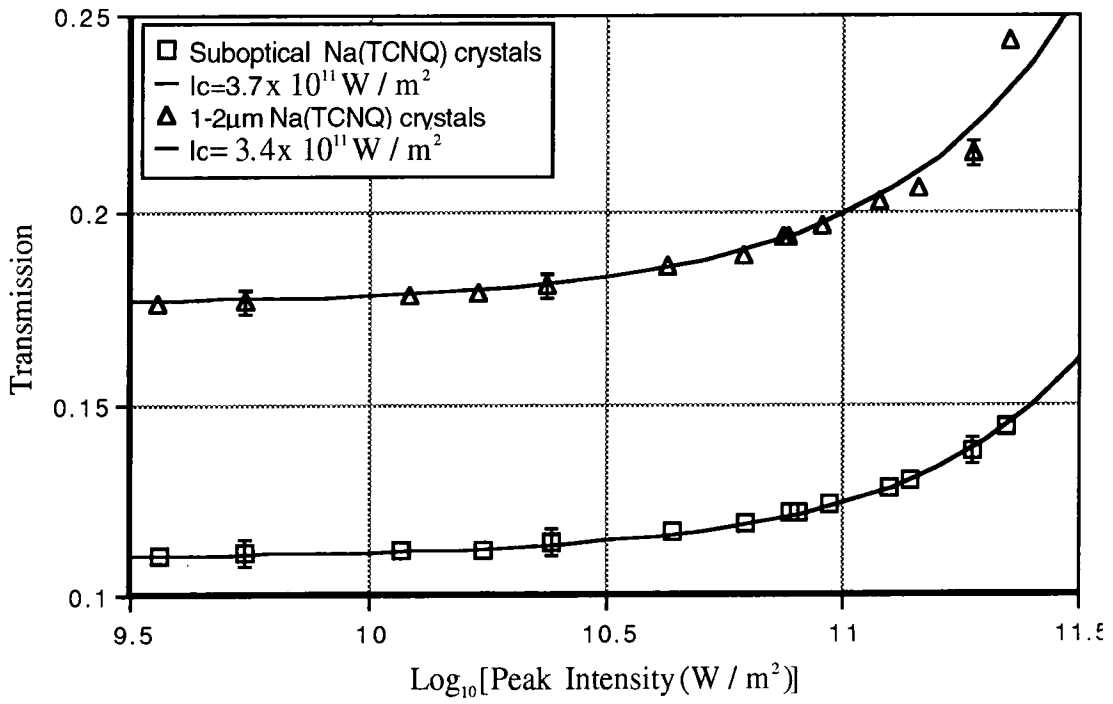

Figure 7.8 Saturation of absorption in Na(TCNQ)/PMMA films

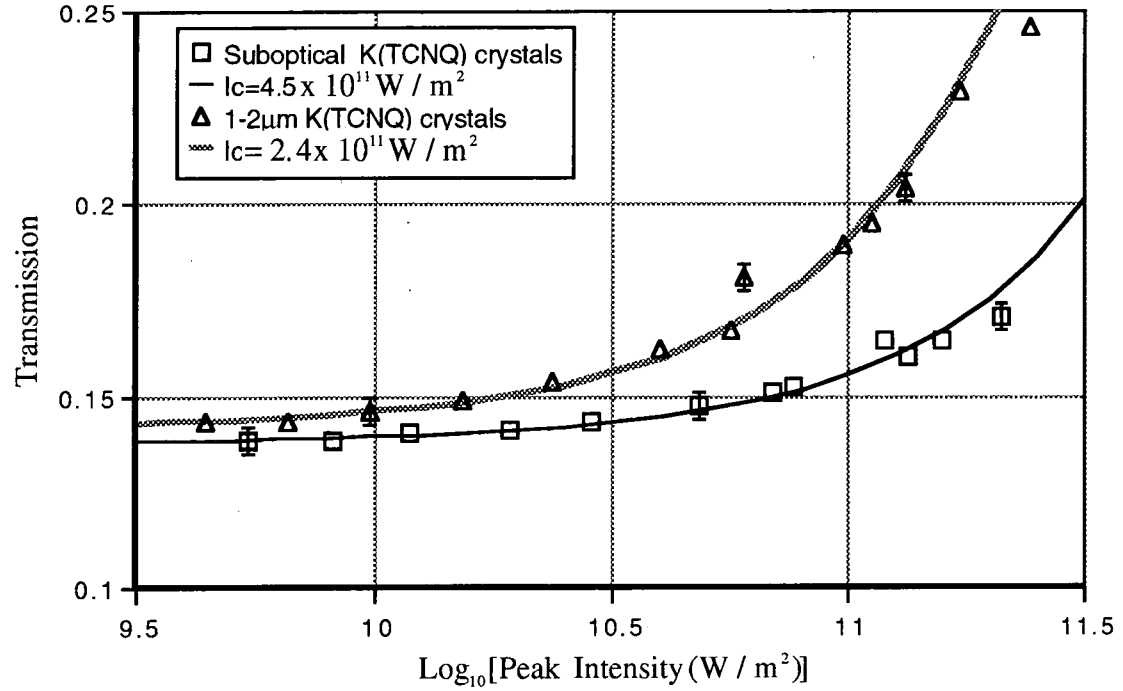

Figure 7.9 Saturation of absorption in K(TCNQ)/PMMA films

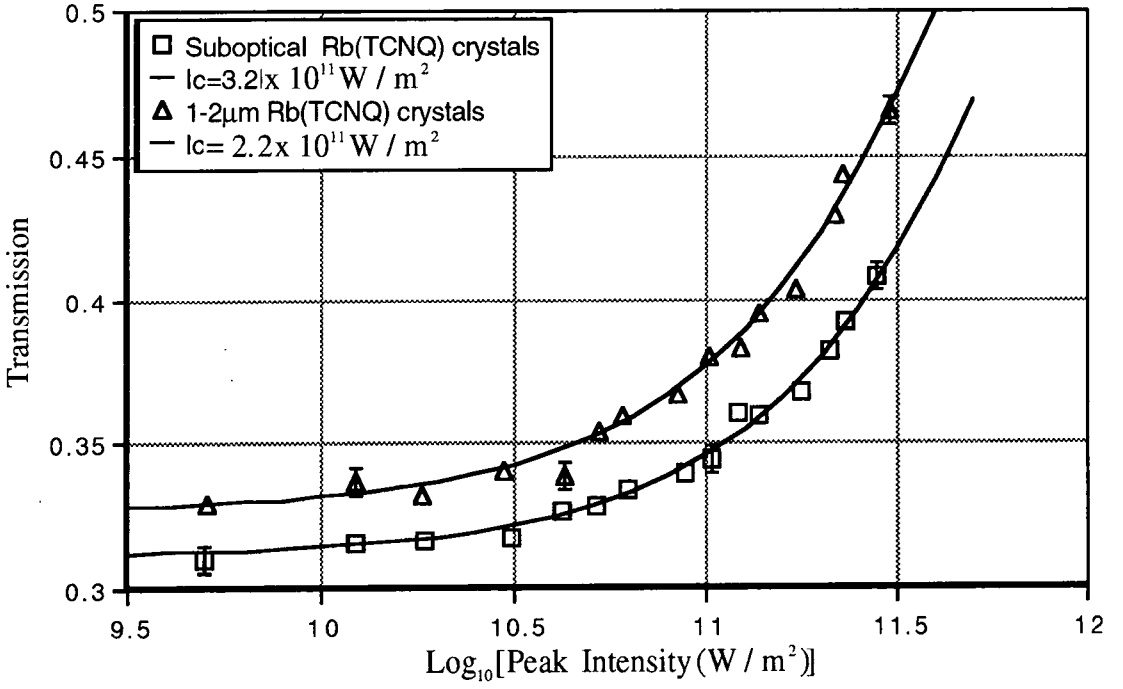

Figure 7.10 Saturation of absorption in Rb(TCNQ)/PMMA films

Values of $\chi(3)$ are quoted in e.s.u.. The relation between $\chi(3)$ in MKS and e.s.u units is $\chi(3)_{e.s.u.} = 7.14 \times 10^7 \chi(3)_{MKS}$, (Boyd 1992)

Crystal size	Wavelength (nm)	Ic $\times 10^{11}$ W/m^2	σ $\times 10^{-21}$ m^2	τ (ns)	Im[$\chi(3)$] $\times 10^{-7}$ e.s.u.	
					Film	Crystallites
S/O	563	6.3	2.7	0.10	-0.21	-12
1-2 μm	563	4.0	2.3	0.19	-0.31	-10
S/O	570	3.9	3.1	0.14	-0.40	-24
1-2 μm	570	3.9	2.6	0.17	-0.37	-22
S/O	577	3.7	3.6	0.13	- 0.49	-21
1-2 μm	577	3.4	3.0	0.17	- 0.50	-29

Table 7.1 Saturable absorption in (NaTCNQ) doped, DCM vapour treated, PMMA films
NB S/O: Sub-optical i.e. < 0.5 μm

Crystal size	Wavelength (nm)	Ic $\times 10^{11}$ W/m^2	σ $\times 10^{-21}$ m^2	τ (ns)	Im[$\chi(3)$] $\times 10^{-7}$ e.s.u.	
					Film	Crystallites
S/O	563	7.9	2.5	0.09	-0.15	-8.0
1-2 μm	563	3.0	2.63	0.26	-0.40	-24
S/O	570	2.7	2.96	0.22	-0.54	-32
1-2 μm	570	1.2	3.03	0.48	-1.1	-65
S/O	577	4.5	3.41	0.11	-0.38	-22
1-2 μm	577	2.4	3.40	0.23	-0.64	-38

Table 7.2 Saturable absorption in K(TCNQ) doped, DCM vapour treated, PMMA films
NB S/O: Sub-optical i.e. < 0.5 μm

Crystal size	Wavelength (nm)	Ic $x10^{11}W/m^2$	σ $x10^{-21}m^2$	τ (ns)	Im[χ(3)] $x10^{-7}$e.s.u.	
					Film	Crystallites
S/O	563	2.0	1.95	0.45	-0.37	-22
1-2μm	563	5.0	2.0	0.18	-0.15	-8.0
S/O	570	5.3	2.3	0.14	-0.16	-9.4
1-2μm	570	4.0	2.1	0.21	-0.20	-12
S/O	577	3.2	2.8	0.19	-0.34	-20
1-2μm	577	2.2	2.5	0.31	-0.44	-26

Table 7.3 Saturable absorption in Rb(TCNQ) doped, DCM vapour treated PMMA films
NB S/O: Sub-optical i.e. < 0.5 μm

Crystal size	Wavelength (nm)	Ic $x10^{11}W/m^2$	σ $x10^{-21}m^2$	τ (ns)	Im[χ(3)] $x10^{-7}$e.s.u.	
					Film	Crystallites
1-2 μm	563	1.6	2.5	0.44	-0.74	-44
1-2 μm	570	3.5	2.9	0.17	-0.39	-23
1-2 μm	577	4.2	3.3	0.12	-0.37	-22

Table 7.4 Saturable absorption in Na(TCNQ) doped, heat treated PMMA films

7.8 Reverse saturable absorption

This section refers to measurements of the dependence of transmission on incident beam intensity, carried out at 750 nm i.e. on the high energy side of the CT band. In this

wavelength region, the transmission of the salt doped films were found to decrease with increasing light intensity. The key parameter determining the nonlinearity in this case is the nonlinear absorption coefficient α_2 given by (see section 7.2)

$$\frac{dI}{dz} = \alpha_1 I - \alpha_2 I^2 \tag{7.36}$$

The ratio of beam intensity after traversing the entire length L of a sample I_L, to incident intensity I_0, can be obtained by solving 7.36 to give

$$\frac{I_L}{I_0} = \frac{\exp(-\alpha_1 L)}{1+\alpha_2 I_0 L_{eff}} \tag{7.37}$$

where

$$L_{eff} = \frac{\left[1-\exp(-\alpha_1 L)\right]}{\alpha_1} \tag{7.38}$$

Again assuming an incident pulse with Gaussian profile, the energy transmission is given by

$$T = \frac{\Delta t \int_0^\infty 2\pi r I_L(r)dr}{\Delta t \int_0^\infty 2\pi r I_0(r)dr} \tag{7.39}$$

Or by substituting for $I_L(r)$ in 7.39 using 7.37:

$$T = \frac{\int_0^\infty 2\pi r \left[\frac{\exp(-\alpha_1 L)}{1+\alpha_2 I_0(r) L_{eff}}\right] I_0(r)dr}{\int_0^\infty 2\pi r I_0(r)dr} \tag{7.40}$$

The experimental technique for measuring the variation of transmission with peak beam intensity Ip, is identical to that described above for saturable absorption measurements. Fitting 7.40 to the experimentally measured variation of transmission with Ip yields α_2. Equation 7.12 can then be used to determine $\chi(3)$

7.8.1 Results

As in the measurements around the LE1 band films containing sub-optical crystals and films containing crystals of 1-2 μm diameter were studied. The results for films containing Li(TCNQ), Na(TCNQ), K(TCNQ) and Rb(TCNQ) are shown in figures 7.11 to 7.14. The results are summarised in table 7.5.

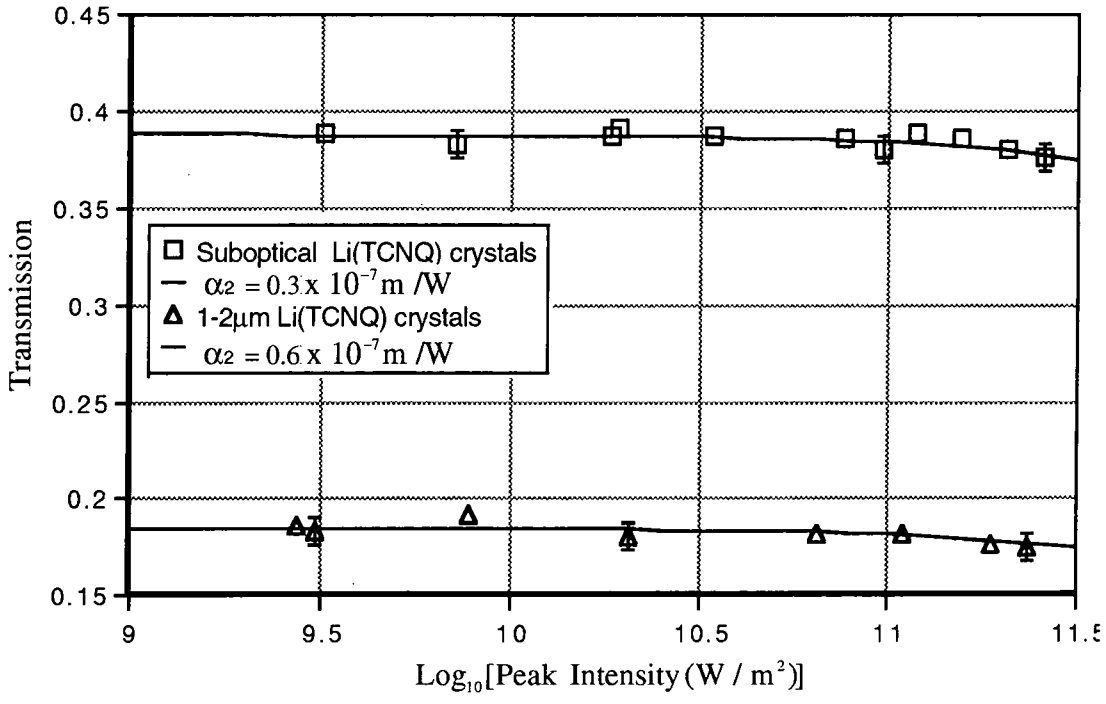

Figure 7.11 Transmission of Li(TCNQ)/PMMA films v Log10 [Peak Intensity]

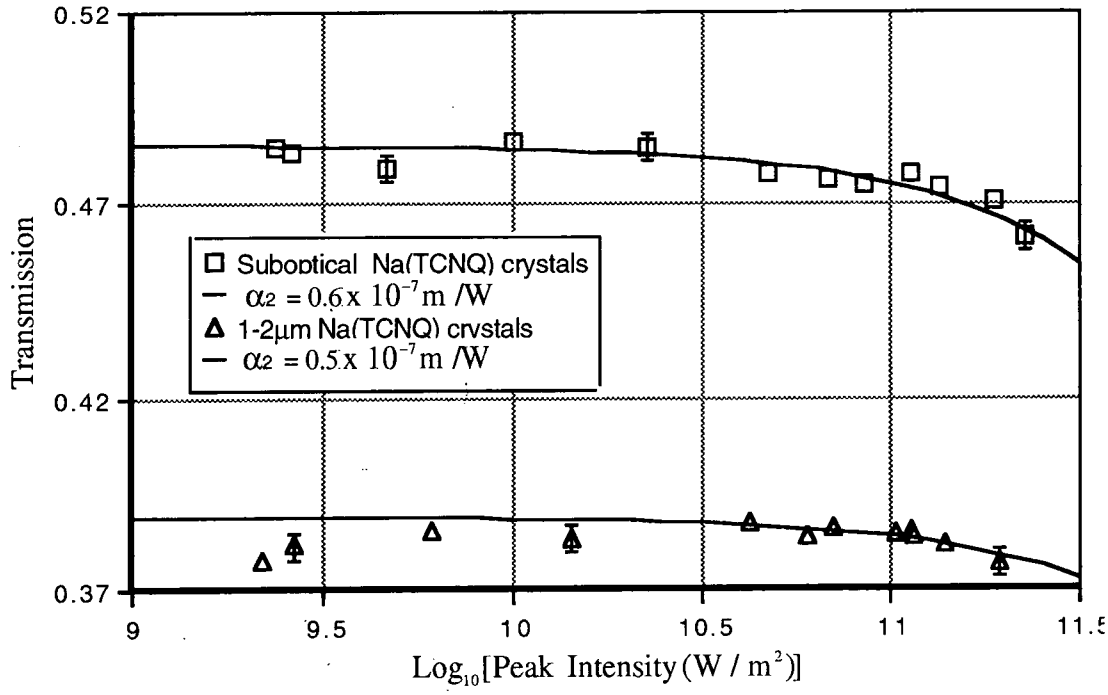

Figure 7.12 Transmission of Na(TCNQ)/PMMA films v Log10 [Peak Intensity]

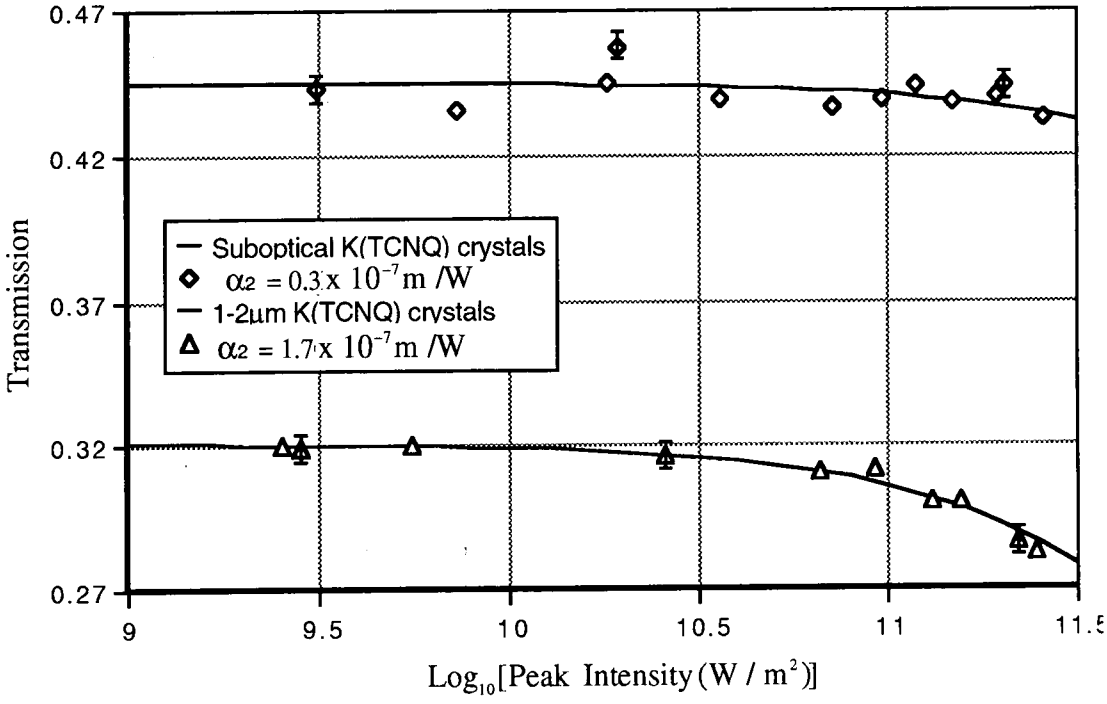

Figure 7.13 Transmission of K(TCNQ)/PMMA films v Log10 [Peak Intensity]

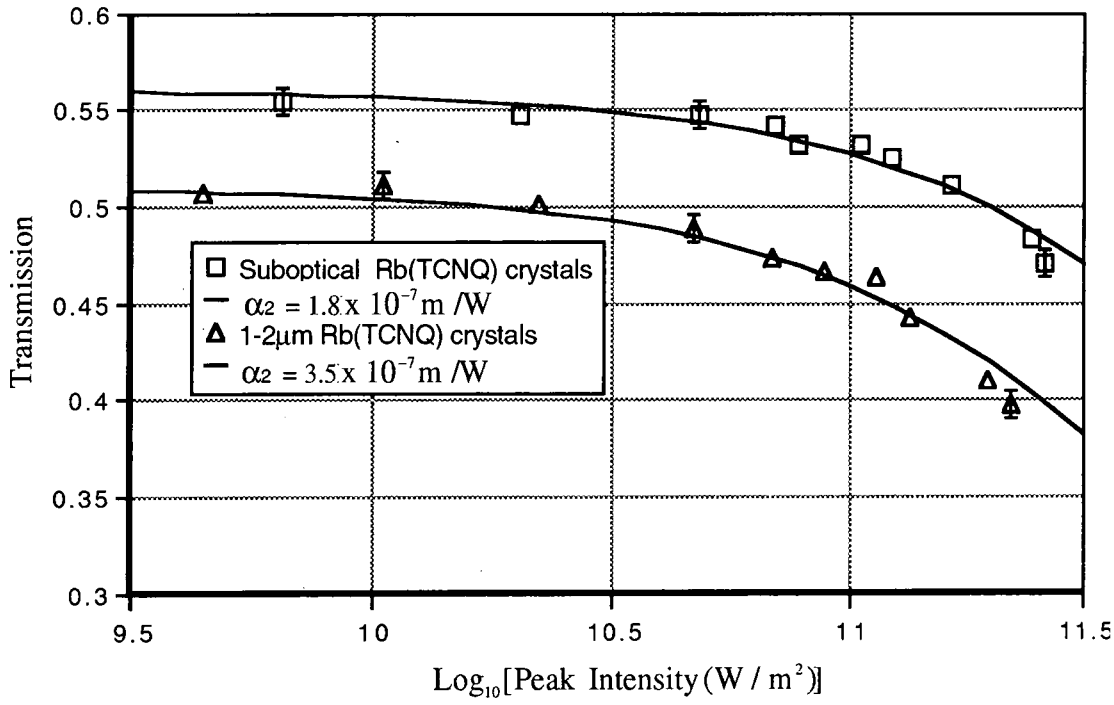

Figure 7.14 Transmission of Rb(TCNQ)/PMMA films v Log10 [Peak Intensity]

Salt	Crystal size	σ x10^{-21}m^2	α_2 x10^{-7}m/W	Im[χ(3)] x10^{-7} e.s.u.	
				Film	Crystallites
Li(TCNQ)	S/O	1.25	0.3	0.19	11
	1-2μm	1.90	0.6	0.38	22
Na(TCNQ)	S/O	1.14	0.6	0.37	22
	1-2μm	1.38	0.5	0.30	18
K(TCNQ)	S/O	1.33	0.3	0.20	12
	1-2μm	1.69	1.7	1.1	65
Rb(TCNQ)	S/O	1.30	1.8	1.1	65
	1-2μm	1.51	3.5	2.2	130

Table 7.5 Reverse saturable absorption in TCNQ salt doped PMMA films at 750nm
NB S/O: Sub-optical i.e. < 0.5 μm

7.9 Discussion

In the measurements carried out close to the LE1 band, all films exhibited negative values of $Im\chi^{(3)}$ corresponding to bleaching of the absorption band. The largest single value of $Im\,\chi^{(3)}$ was exhibited by K(TCNQ) doped films containing crystallites of 1-2 μm diameter, although all salts studied produced films possessing similar nonlinearities, with values of $Im\chi^{(3)}$ between 0.15 x10^{-7} and 1.1 x10^{-7} e.s.u.. Since only three wavelengths were studied it is difficult to assess the wavelength dependence of $Im\chi^{(3)}$. Normally as an absorption resonance is approached $Im\chi^{(3)}$ increases due to resonant enhancement, (Boyd 1992). For this series of measurements the nearest resonance occurs at around 610 nm thus one would expect to find $Im\chi^{(3)}_{577} > Im\,\chi^{(3)}_{570} > Im\,\chi^{(3)}_{563}$. This is indeed the case for vapour treated Na(TCNQ)/PMMA films, however for heat treated Na(TCNQ)/PMMA films, vapour treated K(TCNQ)/PMMA films and vapour treated Rb(TCNQ)/PMMA films the measured values of $Im\,\chi^{(3)}$ do not follow this pattern. For instance in the case of K(TCNQ) films, the intermediate wavelength (570 nm) value of Im $\chi^{(3)}$ is greatest.

As for the effect of crystallite size, again the fact that only two size regimes (1-2 μm and sub-optical), were studied, makes it difficult to draw any definite conclusions. In K(TCNQ) doped films at all three wavelengths, $Im\chi^{(3)}$ was largest for larger crystals. For Rb(TCNQ) and Na(TCNQ) doped films, at some wavelengths large crystals (1-2 μm) exhibited the greater nonlinearities at other wavelengths sub-optical crystallites did so. However in no case is the discrepancy between the value of $Im\chi^{(3)}$ for dispersions of suboptical crystals and for dispersions of crystals of 1-2 μm, greater than a factor of 2.5, (Rb(TCNQ) doped film at 563 nm)

Summarising the important features of these results:

a) For a particular film, it is possible for Im $\chi^{(3)}$ measured at one wavelength to be larger than that measured at another wavelength closer to resonance.

b) For a particular dopant salt at some wavelengths, larger crystals exhibit a larger value of Im $\chi^{(3)}$ than smaller crystals, whilst at other wavelengths the reverse is true.

In explaining these observations we should first consider the possibility that the variations in the measured value of $\chi^{(3)}$are in fact attributable to experimental error. The experimental procedure involves determination of (i) the characteristics of the incident beam and (ii) the energy transmission of the film under investigation. The former measurement requires determination of a number of parameters - total energy, temporal width and spatial profile for example and is thus potential a source of significant error. A major contribution to the uncertainty in the results arises from the method used to determine total pulse energy. This requires calibration of the photodiodes so as to allow one to convert the voltage signal they produce into a value for incident light pulse energy. A thermopile detector is used in this process which is calibrated by the manufacturers. The pulses used in the experiments were of an energy which while measurable, produced a relatively small signal (around 15 mV). The accuracy with which this can be measured (by observing the signal on an oscilloscope) is of the order of ±1 mV corresponding to a large relative error. In the analysis of the data although the radial variation of beam intensity is taken into account by fitting a Gaussian profile to the beams spatial profile, the temporal profile of the beam is not determined in detail. Instead, the full width at half maximum Δt, is measured and the temporal profile is approximated as a square pulse of width Δt. In contrast the errors in the measured values of film transmission should be comparatively small. To determine the accuracy of the technique used in transmission measurements, this technique was applied to a number of neutral density filters, whose transmission had been determined using a visible wavelength

spectrometer. From these measurements, the error was found to be around ± 0.3%.

With the above considerations in mind, in order to minimise errors, at each wavelength used, measurements on all films were conducted without adjusting the laser cavity, hence ensuring that the incident beam had the same profile in each measurement. The errors introduced by approximating the beam profile should then be the same for each measurement. This should ensure that the relative sizes of Im $\chi^{(3)}$ determined for all the films at a particular wavelength are reliable even if the absolute values may be less so. Reliable comparison of measurements made at the same wavelength should therefore be possible. Changing from one wavelength to another generally requires adjustment of the laser cavity, resulting in a new beam profile which must be determined, and which may involve a greater or lesser error. This implies comparison of values made at different wavelengths is more problematic and conclusions drawn from such comparison are less reliable.

Assuming the differences in the measured values of $\chi^{(3)}$ at different wavelengths and for crystals of different sizes are real one is lead to the conclusion that some mechanism is influencing Im $\chi^{(3)}$ other than those simply arising from the intrinsic optical properties of the salts. One might seek an explanation in terms of the confinement effects described in chapter 1, i.e. quantum confinement and dielectric confinement:

It is unlikely that the crystallites are showing quantum confinement as such effects generally become apparent for very small crystallite dimensions (less than 10 nm in CdS). In addition the saturable absorption measurements were carried out close to a 'local' excitation band associated with a transition confined to the TCNQ molecules in the crystal. Thus the wavefunction of the associated electron is expected to be highly localised and insensitive to crystallite dimension down to very small sizes. Whilst the size of crystallites

in films containing sub-optical crystals is not known it seems unlikely that they are of such a small size. In any case in quantum confined systems one expects nonlinearity to decrease as crystallite size increases which was not always the case in the results described above.

Turning now to dielectric confinement effects. Taking first the SP-dielectric confinement mechanism described in appendix 1 an estimate of its likely effect in films containing sub-optical crystals can be determined by calculating the local field correction factor f_l .

Due to the anisotropic nature of these materials the enhancement factor is dependent on relative alignment of crystals and electric field. For fields polarised perpendicular to the TCNQ axis of the crystal the dielectric constant at 580 nm (see appendix 3) is 0.96 + **i** 2.40. Using equation A1.2, and approximating the dielectric constant of PMMA as n^2, where n=1.492 is the measured value of refractive index at 633 nm, the magnitude of the local field correction factor is found to be 1.13. From equation A1.7, this produces an enhancement in $\mathrm{Im}\chi^{(3)}$ of f_l^4 =1.63. For fields polarised parallel to the TCNQ axis the dielectric constant at 580 nm is 1.12 + **i** 0.17, the magnitude of the local field correction factor is found to be 1.20. From equation 1.7 this produces an enhancement in $\mathrm{Im}\chi^{(3)}$ of f_l^4 = 2.05.

For larger crystals the LP-dieletric confinement mechanism described by the factor Q_{NF} of chapter 1, which occurs when the wavelength of incident light coincides with a resonance of a particle comes into play. Quantitative calculations are complex. However the general features of this type of confinement may throw light on these results. Calculations (Wang 1991) for CdS spheres in various liquid media predict that Q_{NF} is small (around two) for

very small crystals i.e. < 10 nm. As crystal size increases from 10 nm to 100 nm Q_{NF} increases monotonically. For sizes larger than this the behaviour of Q_{NF} depends on whether the exciting wavelength is in a strongly or weakly absorbing region. In weakly absorbing regions oscillations appear in Q_{NF} which is now very sensitive to changes in crystallite size. For instance, under illumination by light of wavelength 641 nm, Q_{NF} varies from 20 to 6 as crystallite radius changes from 550 nm to 600 nm. When the wavelength of light is in an absorbing region these oscillations are suppressed. In that case Q_{NF} is largest for smaller crystals of around 100 nm radius after which Q_{NF} begins a steady downward trend, onto which smaller but still significant oscillations in Q_{NF} are superimposed (see figure 7.15).

Whilst the details of these calculations apply only to CdS spheres, one may perhaps expect the general features to apply in the composites studied here. The saturable absorption measurements were carried out in a strong absorption region. Thus on the basis of the calculations of Wang (1991) one expects a behaviour of Q_{NF} qualitatively similar to that shown in figure 7.15. It is possible that in films exhibiting largest nonlinearities resonances in Q_{NF} are occurring. The sensitivity of these resonances to both wavelength and crystallite size could explain the observed dependence of nonlinearity on these parameters. In order to determine wether dielectric confinement is responsible for the erratic values of $\mathrm{Im}\chi^{(3)}$ it would be necessary to actually calculate the values of Q_{NF} and hence determine for which wavelengths/crystal sizes resonances are expected. This would however require knowledge of the size and shape of the crystals which is not known at present.

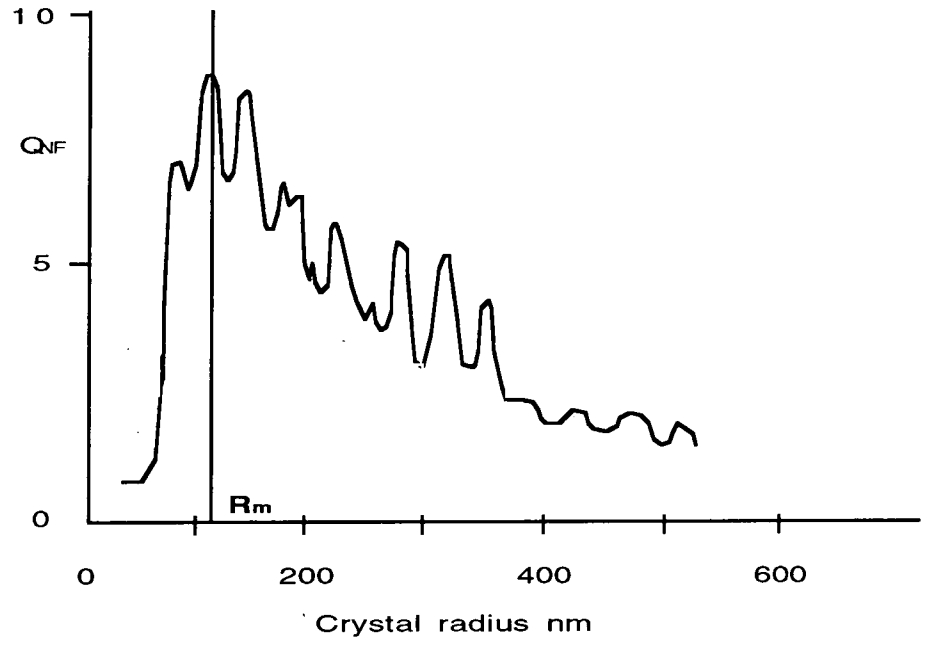

Figure 7.15 Typical variation of QNF with crystal size (absorbing region), (Wang 1991)

Moving on to the measurements made at 750 nm, all the films exhibited reverse saturable absorption corresponding to positive values of $\mathrm{Im}\chi^{(3)}$. The two possible mechanisms for this reverse saturable absorption are, excited state absorption, where following promotion to an excited state, further transitions to newly accessible states are made possible. The second mechanism is two photon absorption where at high intensity the probability of two photons being simultaneously absorbed becomes significant (Boyd 1992). Further measurements, in particular, measurement of the temporal evolution of the nonlinearity, are required to determine which process is responsible in this case

Measurements were only made at one wavelength, so nothing can be said of the wavelength dependence of $\mathrm{Im}\chi^{(3)}$. In the 750 nm region the size of the $\mathrm{Im}\,\chi^{(3)}$ was

significantly larger in Rb(TCNQ) and K(TCNQ) doped films than in Li(TCNQ) and Na(TCNQ) films. The reasons for Rb(TCNQ) having a significantly larger value of Im $\chi^{(3)}$ are not clear. Further work is required to determine whether this is due to confinement effects and therefore related to crystallite morphology, or is due to Rb(TCNQ) having a larger intrinsic nonlinearity. As far as the crystallite size dependence of Im$\chi^{(3)}$ is concerned, for all salts except Na(TCNQ), films containing larger crystals exhibited greater nonlinearity. The difference was particularly large (factor of 5) in the case of K(TCNQ) doped PMMA films. Again, a possible explanation for the size dependence of Im $\chi^{(3)}$ is the occurrence of resonances due to LP-dielectric confinement in the larger crystals.

One might compare the measured nonlinearities to other similar systems currently being investigated. Due to the fact that different groups quote different parameters to describe the size of the resonant nonlinearity it is sometimes difficult to make direct comparison. In degenerate four wave mixing (DFWM) studies a commonly quoted parameter is $|\chi^{(3)}|/\alpha$ where α is the linear absorption coefficient measured at low intensity. In saturable absorption measurements the parameter 1/Ic is often quoted. Reference to equation 7.23 shows that providing the real part of $\chi^{(3)}$ is small compared to the imaginary part, these two parameters are directly proportional to each other.

In the films studied in this work greatest nonlinearity in the LE1 absorption band region was observed at 570 nm in a K(TCNQ) doped film containing 1-2 μm crystals.

For this film $|\chi^{(3)}|/\alpha \geq \text{Im}\,\chi^{(3)}/\alpha = -1.1 \times 10^{-7}/1.86 \times 10^{5} = -5.9 \times 10^{-13}$ esu m

This corresponds to a value of Ic given by $1/Ic = 8.3 \times 10^{-12}$ m^2/W

The associated lifetime of the excited state was $\tau = 0.48$ ns

Greatest nonlinearity at 750 nm was seen for Rb(TCNQ) doped film containing 1-2 μm crystals.

For this film $|\chi^{(3)}|/\alpha \geq \mathrm{Im}\chi^{(3)}/\alpha = 2.2 \times 10^{-7}/0.74 \times 10^{5} = 3.0 \times 10^{-12}$ esu m

Comparing the above values first with microcrystalline dispersions, Hilinski (1988) measured saturable absorption of the exciton absorption band at 480 nm in polymer films containing cadmium sulphide microcrystals. The bleaching mechanism was proposed to be due to exciton/trapped carrier interaction reducing the oscillator strength of exciton absorption. A saturation intensity of $1.3 \times 10^{10} W/m^2$ was measured corresponding to a value of $1/Ic = 7.7 \times 10^{-11}\ m^2/W$. The recovery time was around 0.1 ns although a slow component did persist for several nanoseconds.

Olbright (1987) measured saturable absorption in a Corning CS 3-69 filter containing CdS_xSe_{1-x} and determined a saturation intensity of $1 \times 10^{11}\ W/m^2$ giving a value of 1/Ic of $1 \times 10^{-11} m^2/W$.

Horan (1990) measured saturable absorption in colloidal distributions of BiI_3 and determined a saturation intensity of $3 \times 10^{11}\ W/m^2$ giving $1/Ic = 3.3 \times 10^{-12} m^2/W$. Here the mechanism was thought to be chemical dissociation of the I^{3-} ion. Consequently the recovery time was slow i.e. several nanoseconds.

Yumoto studied CdSe microcrystallites in a sputtered SiO_2 film using degenerate four

wave mixing. At 600 nm a value of $|\chi^{(3)}| = 1.3 \times 10^{-8}$ e.s.u. was obtained. The absorption coefficient α, at 600 nm was 1.27×10^5 m^{-1}. Thus $|\chi^{(3)}|/\alpha = 1.02 \times 10^{-13}$ e.s.u. m. Biexponential decay of the nonlinearity was noted with lifetimes 10 ps and 120 ps.

Shinojima (1992), studied CdSSe doped glass using DFWM . A value of $|\chi^{(3)}| = 1 \times 10^{-9}$ e.s.u. was measured at 600 nm. The absorption coefficient here was 2×10^3m^{-1} giving a value of $|\chi^{(3)}|/\alpha = 5 \times 10^{-13}$ e.s.u. m. The associated lifetime was 70 ps.

Masumoto (1988) used saturable absorption to determine the nonlinear optical properties of CuCl microcrystals in NaCl. Crystallites of sizes ranging from 3 nm to 10 nm were studied around 385 nm near an exciton absorption. Nonlinearity was found to decrease, with increasing crystallite size. A saturation intensity of 4.2×10^6 W/m^2 was measured, corresponding to a $1/I_c$ value of 2.4×10^{-7} m^2/W. This value indicates a very large value of nonlinearity comparable to that of multiple quantum wells, however doubt has recently been expressed about the accuracy of these values.

Vandyshev (1992) studied saturable absorption at 533 nm, in CdSe doped glasses containing crystallites of 10 nm and below. Nonlinearity was found to decrease, with decreasing crystallite size. A saturation intensity of 1×10^9 Wm^{-2} was measured corresponding to a value of $1/Ic = 1 \times 10^{-9}$ m^2/W with a lifetime of 2 ns.

At present a great deal of interest is being shown in multiple quantum wells as sources of large resonant nonlinearity. Miller (1982) measured saturable absorption in $GaAs/Ga_{1-x}Al_xAs$ multiple quantum well structures near to the exciton absorption peak at

around 848 nm. A saturation intensity of 5.8×10^6 W/m^2 was measured. Thus $1/Ic = 1.7 \times 10^{-7}$m^2/W. A recovery time of 21ns was measured. The likely mechanism for saturation was screening of the electron/hole interaction by photogenerated electrons and holes.

Thus the nonlinearities measured in the present work are well below those of multiple quantum wells. However they are comparable with most of the microcrystalline dispersions described above.

Chapter 8

Summary & Conclusions

It has been demonstrated that a series of TCNQ salts can be dispersed, in microcrystalline form, within host polymer matrices producing thin film composites of good optical quality, allowing their characterisation by optical techniques. Such dispersions can be formed by either heat treatment, or solvent vapour infusion of films containing the salt in ionically dispersed form. Conversion from molecularly dispersed phase to microcrystalline phase can be very efficient approaching 100% using both methods. Vapour treatment gives the most satisfactory results in that a greater range of crystallite sizes can be produced by control of various treatment parameters (see chapter 4). Crystallite diameters ranging from 100 μm to sub-optical (estimated as < 300 nm) have been produced. Crystallites are uniformly dispersed throughout the film and where visible, are of uniform size. It should be possible to extend these methods of preparation to other salts of the TCNQ family providing there exists:

a) a common, efficient solvent of the salt and host polymer, to enable formation of the initial solution from which thin films may be formed.
b) a non-solvent of the salt which is able to infuse the host polymer film and bring about crystallisation.

In the case of the Na, K and Rb salts of TCNQ, the position of the CT band in the linear absorption spectra of thin film dispersions shows shifts to higher energy compared to its position in the spectra of KBr pellets containing ground, bulk crystals, grown from solution. In the case of Li(TCNQ) film dispersions, no shift in the CT band to high energy is seen. Instead the CT band either coincides with its position in KBr disc dispersions (this is the case following the treatment with non-solvents, of Li(TCNQ), resulting in suboptical crystals), or is shifted to lower energy (this is the case following treatment with efficient solvents of Li(TCNQ) such as acetonitrile, resulting in crystals of 1-2 μm with needle-shape).

Possible reasons for these shifts are the differences of crystallite shape within KBr disc and thin film dispersions. Mie-Gans theory, (chapter 5), predicts that spheres produce absorption spectra with the CT band in the same position as in bulk material; disc-like morphology leads to shifts of the CT band to higher energy; and needle-like morphology leads to shifts towards lower energy. For K(TCNQ) quantitative calculations indicated that the position of the CT band in measured absorption spectra of thin film dispersions could be explained by assuming a disc like morphology with axial ratio around 1:12. However to explain the strength of the LE1 and CT bands it is necessary to assume a high degree of alignment of the discs with their short axes perpendicular to the plane of the film. Film refractive index measurements (Chapter 6), do not support the existence of such a distribution

Shifts of the CT band to higher energy could also arise from either an increase in the onsite Coulomb repulsion U or the transfer integral t as described in chapter 3. Increases in U can occur in very small crystallites due to reduction in the screening of electron correlations Reduction in t could be brought about by changes in the structure of the microcrystals to one exhibiting a larger spacing of TCNQ molecules within the stack. Such structural

changes could be caused in crystals within thin film dispersions, by the high viscosity, supersaturated environment in which crystallisation occurs.

To identify with certainty which mechanism is responsible for the observed spectral shifts, it is essential that methods of determining shape, size and alignment of crystallites within the film are developed. In principle this should be possible using either TEM or small angle X-ray scattering. Attempts to use these methods have so far proved unsuccessful for reasons already outlined in chapter 4. Nevertheless perseverance with these techniques is still justified. For TEM for instance different host polymers and resins could be used to find a combination capable of yielding good microtomed samples. In addition infusion of microtomed samples with heavy metal dyes to increase contrast between crystallites and surrounding polymer may improve the quality of the images obtained. One of the main advantages of successfully determining crystallite size is that it would allow a better understanding of the factors affecting crystallite size and would allow determination of the lower limit of crystallite size obtainable with these techniques. Further, quantum confinement effects come into play for crystallite dimensions much smaller than are visible with optical microscopes and if one is to be able to follow changes in electronic properties due to quantum confinement it is essential that a way of measuring crystallite dimension in this size regime is found.

The films produced by these methods are of sufficient quality to allow measurement of nonlinear optical properties. Moderate, resonantly enhanced nonlinearity is observed. Intensity dependent transmission measurements around 570 nm have indicated that the LE1 band exhibits bleaching. On the assumption of a two level model the lifetime of the excited state associated with this absorption process is found to be in the range 0.1-0.5 ns. Some evidence of dielectric confinement originating from resonances between the optical field and the modes of oscillation of the crystallite comes from the variation of saturation

intensity with wavelength and crystallite dimension. At 750 nm instead of bleaching of the absorption an increase in absorption is noted. The mechanism responsible for this process remains to be clarified.

The nonlinearities measured in this work are well below those of multiple quantum wells. However they are comparable with most of the microcrystalline dispersions described above. It is unlikely that the composites so far studied have potential for being the basis of actual devices. However the methods of composite formation should be applicable to other members of the TCNQ salt series which may exhibit greater nonlinearity. In particular it would be interesting to disperse some of the more conductive TCNQ salts such as TTF(TCNQ) into polymers and to determine their nonlinear properties. Furthermore, once techniques have been developed to determine the size and shape of sub-optical crystallites in thin film dispersions it should be possible to correlate nonlinear properties with crystallite dimension and to compare behaviour with inorganic semiconductors. The temporal evolution of the nonlinearity is yet to be determined and could throw light on the underlying electronic processes in these materials.

Appendix 1

Confinement Effects in Semiconductor Particles

A1.1 Small particle or SP-dielectric confinement

Dielectric confinement effects are caused by the difference between the microscopic electric field which acts to polarise crystallites dispersed within a host medium and the macroscopic electric field associated with an incident light wave. Two sources of dielectric confinement effects exist. The first which is important for large crystals (i.e. greater than 100 μm) and which depends on resonances between the optical modes of the crystallite and the wavelength of the incident light, has been described in chapter 1. The second dielectric confinement mechanism, depends on the difference between the dielectric constant of the dispersed particles, and of the surrounding medium. The theory describing it which is outlined below, is applicable to very small crystallites - i.e. much smaller than the wavelength of the incident light. This mechanism is subsequently termed the small particle, or SP-dielectric confinement effect.

For a dispersion of spherical crystallites, in which the volume fraction of crystallites V, is much less than 1, the effective dielectric constant at low electric field strength is given by (Bottcher 1973))

$$\varepsilon^* = \varepsilon_1 + 3V\varepsilon_1 \frac{\varepsilon_d - \varepsilon_1}{\varepsilon_d + 2\varepsilon_1} \qquad \text{(A1.1)}$$

Where ε_d is the dielectric constant of the crystallite, ε_1 is the dielectric constant of the

surrounding medium and ε^* is the effective dielectric constant of the medium as a whole.

When subject to intense optical fields, ε^* will undergo changes due to induced polarisation components dependent on the third order susceptibility, (for centrosymmetric systems no second order component comes into play). If the contribution due to the change in the dielectric constant of the linear host medium can be neglected, then from A1.1:

$$\delta\varepsilon^* = V\left(\frac{3\varepsilon_1}{\varepsilon_d + 2\varepsilon_1}\right)^2 \delta\varepsilon_d = V f_1^2 \delta\varepsilon_d \qquad \text{(A1.2)}$$

where f_1 is known as the local field correction factor. The field inside a spherical crystallite E_i is related to the field in the vicinity of the particle E by equation A1.3, (Bottcher 1973).

$$E_i = f_1 E \qquad \text{(A1.3)}$$

A1.3 holds for oscillating, as well as static fields. For an optical field given by

$$E(t) = E(\omega)e^{-i\omega t} + E^*(\omega)e^{i\omega t} \qquad \text{(A1.4)}$$

the change in the dielectric constant of the individual crystallites such a field induces, is given by A1.5 (see equation 7.5 in Chapter 7) :

$$\delta\varepsilon = 3\chi^{(3)}|E_i|^2 = 3\chi^{(3)}|f_1 E|^2 \qquad \text{(A1.5)}$$

Where $\chi^{(3)}$ is the third order susceptibility of the dopant material.

Thus from A1.2 the change in the dielectric constant of the composite medium is given by

$$\delta\varepsilon^* = 3V|f_1|^2 f_1^2 \chi^{(3)}|E|^2 \qquad \text{(A1.6)}$$

So the effective third order susceptibility of the composite medium is given by

$$\tilde{\chi}^{(3)} = V|f_1^2|f_1^2\chi^{(3)} \qquad \text{(A1.7)}$$

Thus in the small crystal regime $\chi^{(3)}$ can be enhanced by the fourth power of the local field correction factor.

A1.2 Quantum confinement

As described in chapter 1, quantum confinement refers to the confinement of the electrons and holes within a crystallite small enough that their wavefunctions become perturbed by the presence of a crystallite's boundary. This confinement can result in significant differences in the optical properties of such crystallites compared to those of bulk material. In small crystallites the oscillator strength becomes concentrated in the sharp excitonic transitions of lower energy and the dominant nonlinear optical process becomes that of state filling of these excitonic transitions, as opposed to the band filling mechanism predominant in bulk materials, (Schmitt-Rink, 1987).

The physics of semiconductor microcrystallites lies between that of individual molecules and that of normal bulk material. It is not possible to adopt the normal Bloch theory of bulk semiconductors as this requires an infinitely extended periodic system. The usual approach is the so-called effective mass approximation (Harrison 1970), where the electron motion is

represented as a wave packet Ψ, of Bloch states $u_n(r)$, given by:

$$\Psi = F_n(r)u_n(r) \tag{A1.8}$$

Where $F_n(r)$ is an envelope function.

In quasi-bulk systems a two band model - a filled valence band and an empty conduction band separated by an energy gap Eg results. The finite value of the dielectric constant enables bound states of electron hole pairs, (excitons), to exist. In the bulk these excitons have a spatial extension characterised by the exciton Bohr radius a_{exc}. In addition when trapped by an impurity the electron and hole states have finite spatial extent characterised by the electron and hole Bohr radii, a_e and a_h,. The Bohr radii are inversely proportional to the effective mass of the associated particle m_e^*, m_h^*. In general $m_e^* < m_h^*$ hence electrons have larger Bohr radii and kinetic energies making them harder to localise than holes.

Much of the interest in the nonlinear properties of semiconductor doped glasses has centred around wavelengths close to the exciton resonances of the semiconductor, as it is here where quantum confinement effects are thought to lead to enhancements in third order nonlinearity.

Excitons within a semiconductor crystallite obey the following Schrodinger equation (Brus 1986).

$$\left(-\frac{\hbar^2}{2m_e^*}\nabla_e^2 - \frac{\hbar^2}{2m_h^*}\nabla_h^2 - \frac{e^2}{4\pi\varepsilon|r_e - r_h|} + W\right)\Psi(r_e, r_h) = E\Psi(r_e, r_h) \tag{A1.9}$$

The first two terms in brackets describe the kinetic energy of the electron and hole. The third term represents the electron/hole Coulombic interaction. W is a term which describes the potential due to the presence of the crystal/host-medium interface. In simple analyses W is assumed to be zero inside the crystallite and infinite outside. Brus (1984), included a more realistic interface potential which greatly complicates the analysis but leads to qualitatively similar results.

As crystallite radius decreases confinement effects begin to influence the solutions to A1.9. The degree of confinement and hence the deviation from bulk properties is governed by the relative size of the Bohr radii and crystallite radius, a. For weak confinement, where $a_h < a_e < a$, deviations from bulk properties are slight. The electron/hole potential is comparable to the kinetic energy of both holes and electrons and enables exciton states to be formed which are only slightly distorted compared to those that occur in bulk material. The main difference is the limited translational freedom of these excitons due to the finite crystallite size.

For the intermediate confinement regime where $a_h < a < a_e$, the kinetic energy of the electrons is much larger than the electron/hole potential term in A1.9 and so they can be treated as free particles in an infinite potential well. Consequently the electrons exist in discrete states characterised by three quantum numbers, one radial and two orbital (Schmitt-Rink 1987). However when considering holes it is still necessary to include the electron/hole interaction. The holes also exist in discrete states which are split into closely spaced lines by the electron/hole interaction. This regime can be particularly important in direct band gap semiconductors where large differences exist between the electron and hole effective masses.

Strong confinement refers to situations where $a < a_h < a_e$. Here the electron/hole potential is small compared to the wall potential and the kinetic energy of both electrons and holes. Hence the electron and hole terms in the Schrodinger equation are decoupled and the problem becomes that of free particles of effective mass m^*_e and m^*_h in an infinite potential well. The conduction band and valence band are split into a series of discrete energy levels each state being characterised by three quantum numbers, one radial and two orbital.

Features associated with strong confinement are :

i) the replacement of the continuous band to band transition spectrum in the bulk by one containing discrete features associated with transitions between electron and hole states and ii) a shift in the onset of absorption to higher energies (i.e. blue shift) as crystal size decreases

Inhomogeneous broadening due to non-uniform size distribution often leads to discrete bands being smeared out into broader features. Thus the discrete nature of the transitions only becomes clearly visible for very small crystallites. Blue shifts of absorption spectra have been observed in many types of dispersion e.g. dispersions of small CuCl and CuBr crystallites (Ekimov 1985).

Appendix 2

Film Deposition Techniques

The two techniques used to deposit films in the present work are spin coating, and withdrawal from solution

A2.1 Spin coating

In the spin coating technique, a few drops of a solution containing the polymer of which the film is to be made are deposited onto a cleaned substrate. The substrate is then spun at high speed. The spinning action causes the solution to spread into a film which covers the substrate and also causes it dry. Resulting film thickness is governed by spinning speed and spinning period; increasing either parameter results in thinner films. Obviously more concentrated solutions, being more viscous lead to thicker films. The method works best for non-volatile solvents (boiling point greater than 100 C). Volatile solvents evaporate too quickly causing the film to dry before the spinning action can produce a smooth film covering the substrate. Figure A2.1 shows the relation between spinning speed and the resulting film thickness for a PMMA/DMF solution with the stated concentration.

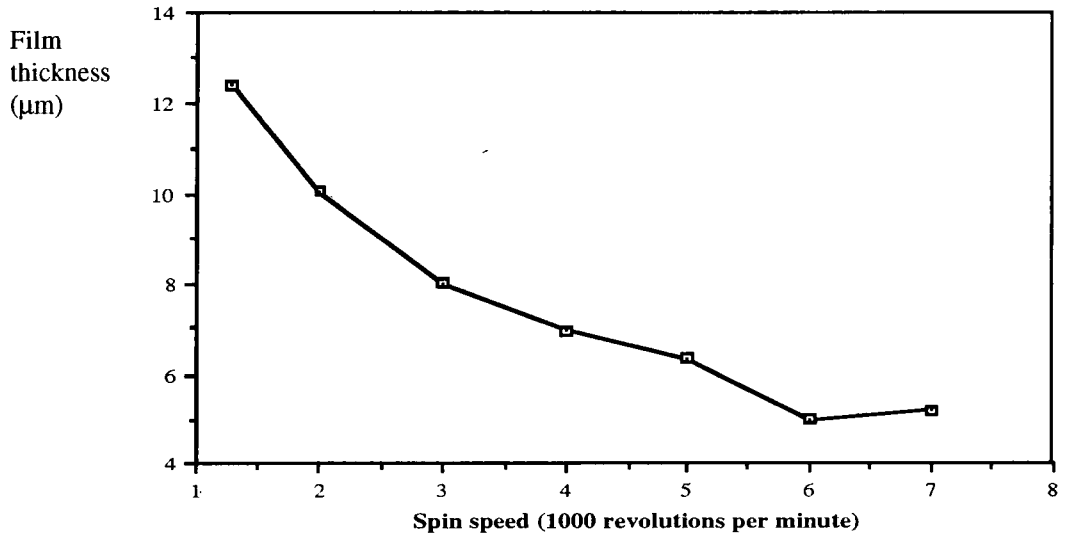

Figure A2.1 Film thickness as a function of spin speed for 4.2 g PMMA, 12 cm^3 DMF

A2.2 Withdrawal from solution

This is a technique developed by Yang et al (1980) and now used widely. In this technique a cleaned substrate is withdrawn at a constant speed from a solution of polymer and solvent. As the substrate emerges from the solution a thin film of solution adheres to the substrate, which then dries to leave the final film. Film thickness is governed by the concentration of the solution and on the withdrawal speed. Faster withdrawal leads to thicker films. This method works best for volatile solvents (boiling point less than 80 C). For non volatile solvents the action of gravity causes the film to slide down the substate before it dries, leading to an uneven film. A diagram of the apparatus used in the substrate withdrawal method is shown in figure A2.2. For solvents with boiling points close to the limit that permits use of solution withdrawal, problems with microbubble formation in the drying film can be encountered. These are caused by solvent vapour which is unable to

escape from the solidifying film, it results in films with a misted appearance.

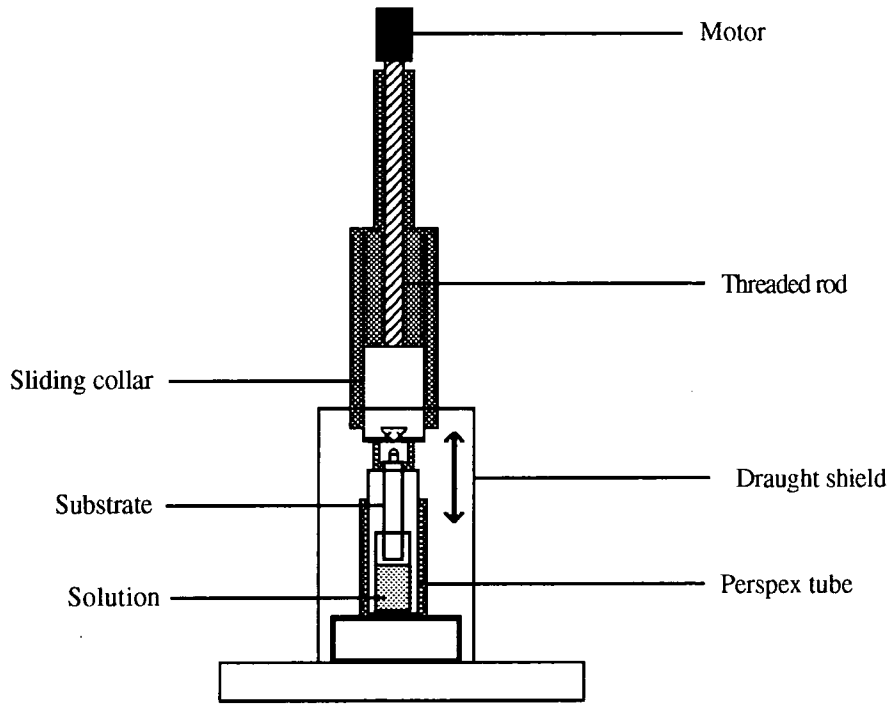

Figure A2.2 Apparatus for substrate withdrawal method

This problem can be overcome by withdrawing the film into an atmosphere rich in solvent vapour, this slows the drying process sufficiently to allow time for solvent to evaporate from the film before the film solidifies. The atmosphere must not be so rich in solvent vapour than the film becomes fluid as this would result in the film slipping down the substrate leading to an uneven film. Usually it is sufficient to attach a perspex tube to the solution container as shown in figure A1.2. This traps some of the solvent vapour from the solution and provides a vapour enriched atmosphere around the film.

With very volatile solvents, if the solution is left exposed to the air for a significant length

of time, sufficient vapour can evaporate from the solution that a concentration gradient is set up in the solution causing the viscosity near the surface to be greater than that in its centre. Such an inhomogeneous solution results in poor quality films with a rippled appearance. This can be remedied by agitating the solution for a few minutes between each withdrawal. Figure A2.3 shows the relationship between withdrawal speed and film thickness for a PMMA/Acetonitrile solution.

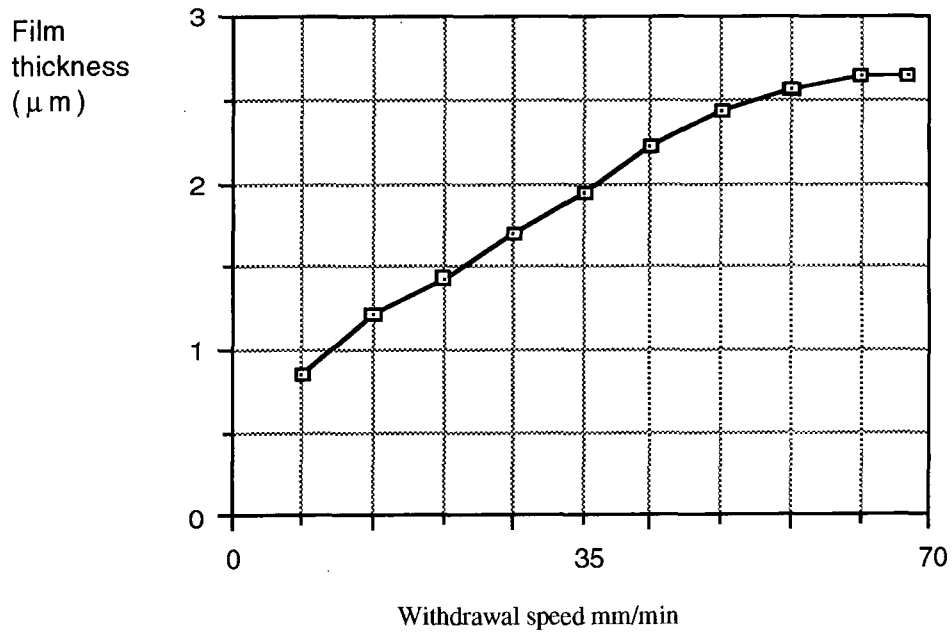

Figure A2.3 Film thickness as function of withdrawal speed for 4.0 g PMMA, 21 cm^3 acetonitrile

Both methods can be used to form films of thicknesses ranging from 100 μm to 0.1 μm.

Appendix 3

Values of the Dielectric Constant of K(TCNQ)

Table A3.1 gives the value of the dielectric constant of K(TCNQ) as measured by Papavasilliou (1979). They are the results of Kramers-Kronig analysis of single crystal, optical reflection measurements.

Key: z refers to the value of the dielectric function parallel to the TCNQ axis

x " " " perpendicular " "

λ(nm)	Re(εz)	Im(εz)	Re(εx)	Im(εx)	λ(nm)	Re(εz)	Im(εz)	Re(εx)	Im(εx)
2200	4.20	0.99	2.93	0.73	1020	-0.74	1.56	3.30	0.74
2100	4.33	1.05	2.87	0.69	1000	-0.60	1.42	3.31	0.78
2000	4.52	1.12	2.82	0.64	980	-0.50	1.27	3.34	0.81
1900	4.75	1.25	2.80	0.59	960	-0.38	1.15	3.35	0.83
1800	5.06	1.50	2.80	0.53	940	-0.28	1.05	3.37	0.82
1700	5.48	1.98	2.81	0.48	920	-0.18	0.95	3.32	0.80
1600	6.05	2.98	2.85	0.45	900	-0.09	0.85	3.25	0.76
1540	6.25	4.10	2.89	0.43	880	0.00	0.80	3.20	0.74
1500	6.07	4.95	2.93	0.42	860	0.05	0.70	3.25	0.71
1460	5.62	5.97	2.97	0.41	840	0.18	0.65	3.33	0.76
1420	4.65	7.10	3.02	0.40	820	0.25	0.60	3.42	0.83
1380	3.32	7.76	3.10	0.41	800	0.32	0.50	3.55	0.96
1340	1.75	7.80	3.13	0.42	780	0.50	0.47	3.68	1.14
1300	0.20	7.48	3.16	0.44	760	0.63	0.40	3.86	1.38
1280	-0.37	7.02	3.18	0.45	740	0.72	0.33	4.02	1.74
1260	-0.80	6.35	3.19	0.45	720	0.80	0.32	4.14	2.05
1240	-1.10	5.82	3.20	0.46	700	0.85	0.31	4.30	2.57
1220	-1.33	5.21	3.20	0.46	680	0.88	0.30	4.42	3.18
1200	-1.48	4.64	3.20	0.47	660	0.92	0.27	4.50	3.85
1180	-1.55	4.20	3.20	0.49	640	0.98	0.24	2.50	4.20
1160	-1.58	3.71	3.21	0.50	620	1.01	0.22	0.50	4.47
1140	-1.55	3.25	3.21	0.52	600	1.06	0.20	0.74	3.65
1120	-1.43	2.83	3.22	0.55	580	1.12	0.17	0.96	2.40
1100	-1.32	2.46	3.22	0.57	560	1.16	0.11	1.24	1.20
1080	-1.17	2.17	3.23	0.61	540	1.25	0.09	1.53	0.24
1060	-1.02	1.96	3.25	0.65	520	1.35	0.07	1.83	0.21
1040	-0.88	1.75	3.27	0.69	500	1.48	0.05	2.12	0.30

Table A3.1 Dielectric constant of K(TCNQ) as measured by Papavasilliou (1979)

Appendix 4

Synthesis of the Alkali Metal Salts

Synthesis of Rb(TCNQ), K(TCNQ), Na(TCNQ) and Li(TCNQ) was carried out according to the methods of Melby (1962). In each case the metal iodide was dissolved in acetonitrile and then added to a hot solution of TCNQ also in acetonitrile (previously dried and distilled). The metal iodide was present in a 2:1 molar ratio to discourage the back reaction. The reaction mixture was filtered and the salt crystals washed with acetonitrile until green washings were obtained.

Elemental analysis was used to determine the purity of the crystals so produced. The results of the elemental analysis are given in table A4.1 along with the calculated values which would be obtained for pure material.

Salt	Experimentally measured composition (%)				Calculated composition of pure material (%)			
	H	C	N	Li	H	C	N	Li
Li(TCNQ)	1.90	68.23	26.57	3.27	1.91	68.27	26.54	3.28
	H	C	N	Na	H	C	N	Na
Na(TCNQ)	1.77	63.78	24.91	10.38	1.77	63.44	24.66	10.12
	H	C	N	K	H	C	N	K
K(TCNQ)	1.69	59.20	23.00	16.10	1.66	59.25	23.02	16.07
	H	C	N	Rb	H	C	N	Rb
Rb(TCNQ)	1.33	49.72	19.49	29.45	1.40	49.83	19.38	29.39

Table A4.1 Elemental analysis results

Appendix 5

Analysis of Intensity Profile of a Gaussian Beam

Consider a light beam with a Gaussian spatial profile given by

$$I = I_p e^{\frac{-r^2}{w^2}} = I_p e^{\frac{-(x^2+y^2)}{w^2}} \qquad \text{(A5.1)}$$

Where r is the distance from the centre of the beam .

As in Chapter 7, let $I_{av}(x)$ be the average intensity in a portion of the beam of length l between X and X+ Δx, where Δx is sufficiently small that the intensity can be considered independent of x in this interval (see figure A5.1).

Thus $I_{av}(x)$ is given by

$$I_{av}(x) = \frac{\int_{-\frac{\ell}{2}}^{\frac{\ell}{2}} I_p e^{-\frac{x^2+y^2}{w^2}} \partial y \Delta x}{\ell \Delta x} \qquad \text{(A5.2)}$$

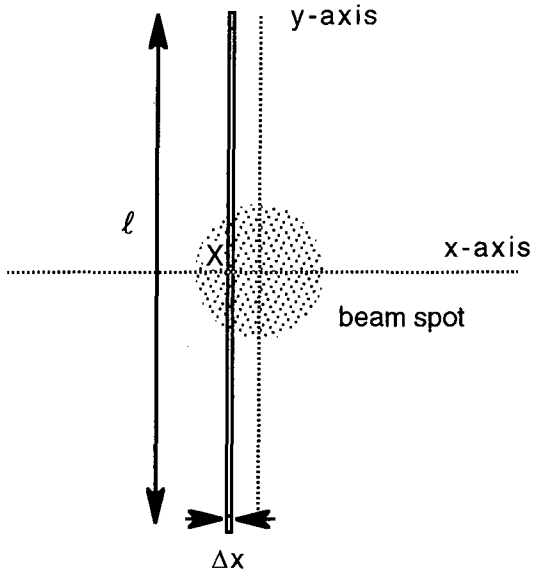

Figure A4.1

Rearranging A5.2 we obtain

$$I_{av}(x) = \frac{\int_{-\frac{\ell}{2}}^{\frac{\ell}{2}} I_p e^{-\frac{y^2}{w^2}} \partial y}{\ell} I_p e^{-\frac{x^2}{w^2}} \qquad \text{(A5.3)}$$

The integral yields a constant value so that we can write

$$\boxed{I_{av}(x) = K I_p e^{-\frac{x^2}{w^2}}} \qquad \text{(A5.4)}$$

Where

$$K = \frac{\int_{-\frac{\ell}{2}}^{\frac{\ell}{2}} I_p e^{-\frac{y^2}{w^2}} \partial y}{\ell} \qquad \text{(A5.5)}$$

Equation A5.4 shows that $I_{av}(x)$ has a Gaussian profile with width, w between the 1/e peak value points. Thus determining the 1/e width of $I_{av}(x)$ as described in chapter 7, is equivalent to finding the 1/e width of the beam as expressed in A5.1

References

Acker, D.S., Hertler, W. R., *J. Amer. Chem. Soc.*, **84**, 3372, (1962).

Afifi, H.H., *Z. Naturforsch.* A, **33**, 344, (1978).

Allais, M., Gandais, M., *J. Appl. Crystallogr.*, **23**, 418, (1990).

Ashcroft, W., Mermin, N. D., *Solid State Physics*, Holt Saunders, Tokyo, (1981).

Atkins, P.W., *Physical Chemistry,* Oxford University Press, Oxford, 503, (1990).

Banyai, L., Hu, Y. Z., Lindberg, M., *Phys. Rev. B*, **38**, (12), 8142, (1988).

Berger, P.R., *Appl. Phys. Lett.*, **52**, 1125, (1988).

Bespelov, B.P., Titov, V. V., *Rus. Chem. Revs.*, **44**, (12), 1092, (1975).

Blanc, J.P., *C.R. Acad. Sci. Ser. B*, **273**, 147, (1971).

Bodegom, B.V., Boer, J. L. d., Vos, A., *Acta. Crystallogr. B,* **33**, 763, (1977).

Bottcher, C.J., *Theory of Electric Polarisation*, Elsevier, Amsterdam, (1973).

Boyd, R.H., Phillips, W. D., *J. Chem. Phys.*, **43**, (9), 2927, (1965).

Boyd, R.W., *Nonlinear Optics*, Academic Press Ltd., London, (1992).

Bozio, R., Pecile, C., *Spectoscopy of Advanced Materials*, R.J. Clark & R.E. Hester, Eds., Wiley & Sons Ltd., London, 1, (1991).

Brau, A., Farges, J. P., *Phys. Stat. Sol. B*, **61**, 257, (1974).

Bret, G., Gires, F., *Appl. Phys. Lett.,* **4,** 175, (1964)

Brus, L.E., *J. Chem. Phys.*, **80**, 4403, (1984).

Brus, L., *J. Phys Chem,* **90**, 2555, (1986).

Chappell, J.S., Bloch, A. N., Bryden, W. A., M. Maxfield, *J. Am. Chem. Soc.*, **103**, 2443,(1981).

Chemla, D.S., Miller, D. A. B., *Optics Lett.*, **11**, 522, (1986).

Cheng, L.P., Herron, N., Wang, Y. J., *J. Appl. Phys.*, **66**, 3417, (1989).

Cohen, R.W., Cody, G.D., Coutts, M.D., Abeles, B., *Phys. Rev. B.,* **8**, 3689, (1973).

Conwell, E.M., *Semiconductors and Semimetals,* E. Conwell, Ed., Academic Press, London, **27**, 215, (1988).

Cotter, D., Girdlestone, H. P., Moulding, K., *Appl. Phys. Lett.*, **58**, (14), 1455, (1991).

Duffin, W.J., *Electricity and Magnetism*, McGraw-Hill, Maidenhead, 313, (1980).

Efros, A.A., *Sov. Phys. Semicond.*, **16**, 772, (1982).

Ekimov, A.I., Efros, A., Onushchenko, A. A., *Solid State Commun.*, **56**, 921, (1985).

Endres, H., *Extended Linear Chain Compounds,* J.S. Miller ed., Plenum press, New York, 274, (1983).

Epstein, A.J., Etemad, S., Garito, A. F., Heeger, A.J., *Phys. Rev. B*, **5**, (3), 952, (1971).

Etemad,S., Penney, T., Engler, E. M., B.A. Scott, P.E. Seiden, *Phys. Rev. Lett.*, **34**, 714, (1975).

Farges, J.P., Baru, A., Vasilescu, D., Neel, J., *Phys. Stat. Solidi*, **37**, 745, (1970).

Gans, R., *Ann. Physik,* **37**, 881, (1912).

Giorgio, V.D., Potenza, G., *Il Nouvo Cimento,* **XLI B**, (2), 254, (1966).

Giorgio, V.D., Banfi, G. P., Righini, G., Rennie, A., *Appl. Phys. Lett.*, **57**, 2879, (1990).

Gires, F., IEEE *J. Quan. Elec.*, **2**, (9), 624, (1966).

Glatter, O., Kratky, O., *Small Angle X-ray Scattering,* Academic Press, London, 3, (1982).

Goldberg, Z.Z., *J. Am. Chem. Soc.*, **99**, 110, (1977).

Gotoh, T., Kondoh, T., Egawa, K., *J. Opt. Soc. Am. B*, **6**, 703, (1989).

Hall, D.W., Borrelli, N. F., *J. Opt. Soc. Am. B*, **5**, 1650, (1988).

Hanamura, E., *Phys. Rev. B*, **37**, (3), 1273, (1988).

Hanson, A.W., *Acta. Cryst.*, **19**, 610, (1965).

Harris, A.B., *Phys. Rev.*, **157**, 295, (1967).

Harrison, W.A., *Solid State Theory,* McGraw-Hill, U.S.A., (1970).

Herbstein, F.H., *Perspectives in Structural Chemistry,* J.D. Dunitz and J.A. Ibers Eds., Wiley, New York, IV, (1971).

Hilinski, E.F., Lucas, P. A., Wang, Y., *J. Chem. Phys.*, **89**, (6), 3435, (1988).

Hill, S.C., Benner, R. E., *Optical effects associated with small particles,* P.W. Barber, R.K. Chang Eds., World Scientific Publishing, Singapore, 3, (1988).

Hiroma, S., Kuroda, H., Akamatu, H., *Bull. Chem. Soc. Jap.*, **44**, 9, (1971).

Hoekstra, A., Spoelder, T., Vos, A., *Acta. Crystallogr. B*, **28**, 14, (1972).

Horan, P., Blau, W., *J. Chem. Phys.*, **92**, (7), 4139, (1990).

Hubbard, J., *Proc. Roy. Soc. Lond. A*, **285**, 542, (1964).

Hubbard, J., *Phys. Rev. B,* **17**, 494, (1978).

Iida, Y., *Bull. Chem. Soc. Jap.*, **42**, 71, (1968).

Iida, Y., *Bull. Chem. Soc. Jap.*, **50**, (6), 1445, (1977).

Ironside, C.N., *J. Opt. Soc. Am. B*, **5**, 492, (1988).

Jacobsen, C.S., *Semiconductors and Semimetals*, E. Conwell, Ed., Academic Press, London, **27**, 325, (1988).

Jain, R.K., Lind, R. C., *J. Opt. Soc. Am.*, **73**, 647, (1983).

Jeszka, J.K., Ulanski, J., Kryszewski, M., *Nature*, **289**, 390, (1981).

Jeszka, J.K., Tracz, A., M. Kryszewski, *J. Phys. D: Appl. Phys.*, **18**, L167, (1985).

Jonkman, H.T., Velde, G. A., Van de, Nieuwpoort, W. C., *Chem. Phys. Lett.*, **15**, 496, (1972).

Kagoshima, S., Ishiguro, T., *J. Phys. Soc. Jpn,* **41**, 2061, (1976).

Karakus, Y., Bloor, D., Cross, G. H., *J. Phys. D: Appl. Phys*, **25**, 1014, (1992).

Katz, H.E., Schilling, M. L., *J. Am. Chem. Soc.*, **111**, 7554, (1989).

Kerker, M., *The Scattering of Light and Other Electromagnetic Radiation*, Academic Press, New York, (1969).

Khanna, S.K., Bright, A. A., Garito, A. F., Heeger, A.J., *Phys. Rev. B*, **10**, (6), 2139, (1974).

Kobayashi, H., *Acta. Cryst., B,* **29**, 2693, (1973).

Kobayashi, H., *Acta. Cryst., B,* **30**, 1010, (1974).

Kobayashi, H., *Acta. Cryst, B*, **34**, 2818, (1978).

Konno, M., *Acta. Cryst. B*, **30**, 1294, (1974).

Konno, M., Saito, Y., *Acta. Cryst. B*, **31**, 2007, (1975).

Konno, M., Ishii, T., Saito, Y., *Acta. Cryst., B*, **33**, 763, (1977).

Lepine, Y., *Phys. Rev. B*, **18**, 3585, (1978).

Liu, L.C., Risbud, S. H., *J. Appl. Phys.*, **68**, (1), 28, (1990).

Lowitz, D.A., *J. Chem. Phys.*, **46**, 4698, (1967).

Lyo, S.K., Gallinar, J. P., *J. Phys. C: Solid State Phys.*, **10**, 1696, (1977).

Maiman, T.H., *Nature*, **187**, 463, (1960).

Masumoto, Y., Yamazaki, M., *Appl. Phys. Lett.*, **53**, (16), 1527, (1988).

Maxwell-Garnett, J.C., *Phil. Trans. R. Soc., Lond. A*, **203**, 385, (1904).

Mazumdar, S., Bloch, A. N., *Phys. Rev. Lett.*, **50**, 207, (1983).

Melby, L.R., Harder, R. J., Hertler, W. R., Mahler,W., R.E. Benson, W.E. Mochel, *J. Am. Chem. Soc.*, **84**, 3374, (1962).

Mie, G., *Ann. Physik*, **25**, 377, (1908).

Miller, D.A., Seaton, C. T., Prise, M. E., Smith, S.D., *Phys. Rev. Letts.*, **47**, 197, (1981).

Miller, D.A.B., *Pro. R. So. London A*, **379**, 91, (1982).

Miller, D.A.B., Chemla, D. S., Eilenberger, D. J., Gossard, A.C., Sang,W.T., *Appl. Phys. Lett.*, **41**, (8), 679, (1982).

Mizoguchi, K., Tsuji,S., *J. Poly. Sci.: Polymer Cemistry Edition,* **16**, 3259, (1978).

Mott, N.F., *Metal-Insulator Transitions,* Taylor and Francis, London, 5, (1974).

Murphy, D.V., Brueck, S. R. J., *Opt. Lett.*, **8**, 496, (1983).

Musurkin, I.A., *Sov. Phys. Solid State*, **12**, 2031(1970).

Olbright, G.R., Peyghambarian, N., Koch, S. W., Banyai, L., *Opt. Lett.*, **12**, 413, (1987).

Oohashi, Y., Sakata, T., *Bull. Chem. Soc. Jap.*, **46**, 3330, (1973).

Ovchinnikov, A.A., *Sov. Phys. JETP*, **30**, 1160, (1970).

Papavassiliou, G.C., Spanou, S. S., *J. Chem. Soc. Faraday Trans. II*, **73**, 1425, (1977).

Papavassiliou, G.C., *J. Chem Soc. Faraday Trans. II*, **74**, 1446, (1978).

Papavassiliou, G.C., *Progr. Sol. St. Chem.*, **92**, 185, (1979).

Papavassiliou, G.C., Yartsev, V. M., *Chem. Phys. Letts.*, **200**, (1&2), 209, (1992).

Park, S.H., Morgan, R. A., Hu, Y. Z., Koch, S.W., Peyghambarian, N., *J. Opt. Soc. Am. B*, **7**, 2097, (1990).

Peierls, R.E., *Quauntum theory of solids, University Press, London,* **108**, (1955).

Polymer Handbook, J. Prandrup, C.H. Immergel Eds., 3rd Edition, (1989).

Rice, M.J., *Solid State Comms.*, **31**, 93, (1979).

Roussignol, P.D., Ricard, D., Rustagi, K. C., Flytzanis,C., *Opt. Commun.*, 55, 143, (1985).

Roussignol, P., *Appl. Phys. A*, **44**, 285, (1987).

Roussignol, P., Flyntzanis, C., *Proc. SPIE Optical Materials 2*, **1127**, 109, (1989).

Sakai, N., *Bull. Chem. Soc. Jap.*, **45**, 3314, (1972).

Sasahi, H., *Elect. Lett.*, **13**, 683, (1977).

Sauteret, C., Herman, J. P., Frey, R., *Phys. Rev. Lett.*, **36**, 956, (1976).

Schulz, T.D., *The Physics and Chemistry of One Dimensional Solids*, L. Alcacer Ed., Riedel London, 1, (1979)

Schmitt-Rink, S., Miller, D. A. B., Chemla, D. S., *Phys. Rev. B*, **35**, 8113, (1987).

Shinojima, H., Yumoto, J., Uesugi, N., *Appl. Phys. Lett.*, **60**, 298, (1992).

Shirotani, I., Kobayashi, H., *Bull. Chem. Soc. Jap.*, **46**, 2595, (1973).

Siemons, W.J., *J. Chem. Phys.*, **39**, 3523, (1963).

Smith, G.B., *J. Phys. D. Appl. Phys.*, **10**, L39, (1977).

Sohler, W., Suche, H., *Appl. Phys. Lett.*, **33**, 518, (1978).

Takagahara, T., *Phys. Rev. B,* **36**, (17), 9293, (1987).

Tanaka, J., Tanaka, M., Kawai, T., Takabe, T., Maki, O., *Bull. Chem. Soc. Jap.*, **49**, (9), 2358, (1976).

Tanner, D.B., Jacobsen, C. S., Bright, A. A., Heeger, A.J.,*Phys. Rev. B*, **16**, 3283, (1977).

Terauchi, H., *Phys. Rev. B*, **17**, 2446, (1978).

Tien, P.K., Ulrich, R., *J. Opt. Soc. Am.*, **60**, (10), 1325, (1970).

Tien, P.K., *Appl. Opt.*, **10**, (11), 2395, (1971).

Torrance, J.B., Scott, B. A., Kaufmann, F. B., *Sol. State Comms.*, **27**, 1369, (1975).

Torrance, J.B., Silverman, B. D., *Phys. Rev. B,* **15**, 788, (1977).

Torrance, J.B., *Acc. Chem. Res.*, **12**, (3), 79, (1979).

Tracz, A., Jeszka, J. K., Shafee, E. E., J. Ulanski, M. Kryszewski, *J. Phys. D: Appl. Phys.*, **19**, 1047, (1986).

Tracz, A., Jeszka, J. K., Kryzsewski, M., Ulanski, J., Botteux, A. Firlej, A., Graja, A. *Synth. Mets.*, **24**, 107, (1988).

Ulanski, J., Kryszewski, M., Tracz, A., *J. Phys. D: Appl. Phys.*, **18**, 451, (1985).

Vandyshev, Y.V., Dneprovskii, V. S., Klimov, V. I., *Sov. Phys. JETP*, **74**, (1), 144, (1992).

Vegter, J.G., Kuindersma, P. I., Kommandeur, J., *Proc . 2nd Int. Conf. on Low Mobility Materials.,* Eilat, Israel, Taylor and Francis, London, 363, (1971).

Vegter, J.G., Kommandeur, J., *Mol. Cryst. Liq. Cryst.*, **30**, 11, (1975).

Vegter, J.G., *Chem. Phys. Lett.*, **3**, 427, (1979).

Wang, Y., *J. Phys. Chem.*, **95**, 1119, (1991).

Weiss, R.S., Gaylord,T.K., *Appl. Phys. A.,* **37**, 191, (1985).

Wherret, B.S., Higgins, N. A., *Proc. R. Soc, Lond. A*, **379**, 67, (1982).

Whiteley, M.A.,*Thorpe's Dictionary of Applied Chemistry Vol. VIII,* Longmans, London, 201, (1947)

Wigner, *Trans. Farad. Soc.*, Lond., **34**, 678, (1938).

Wunderlich, W., *Polymer Handbook,* J. Prandrup, C.H. Immergel Eds., 3rd Edition, 77, (1989).

Yakushi, K., Ikemoto, I., Kuroda, H., *Acta Cryst., B,* **30**, 835, (1974).

Yakushi, K., Ikemoto, I., Kuroda, H., *Acta. Cryst., B,* **30**, 1738, (1974).

Yakushi, K., Kusaka, T., Kuroda, H., *Chem. Phys. Lett.*, **68**, 139, (1979).

Yang, C.C., Josefowicz, J. Y., Alexandru, L., *Thin Solid Films*, **74**, 117, (1980).

Yao, S.S., Karaguleff, C., Gabel, A., R. Fortenberry, Seaton, C.T., Stegeman, G.I., *Appl. Phys. Lett.*, **46**, 801, (1985).

Yao, H., Hayashi, H., *Chem. Phys. Lett.,* **197**, (1& 2), 21, (1992).

Ye, C., Marks, T. J., Yang, J., Wong, G.K., *Macromolecules*, 20, 2324, (1987).

Yumoto, J., Shinojima, H., Uesugi, N., H. Nasu, Y. Osaka, *Appl. Phys. Lett.*, **57**, (23), 2393, (1990).

Zeldovitch, B.Y., Pilipetsky, N. T., Shkunov, V. V., *Principles of Phase Conjugation*, Springer, Berlin, (1985).

Zheludev, N.I., Ruddock, I. S., Illingworth, R., *Opt. Quantum Electron*, **20**, 119, (1988).

Ziman, L.G., Gaponenko, S. V., Malinovski, I. E., *Phys. Status Solidi,* **159**, 449, (1990).

Zyss, J., Chemla, D. S., Nicoud, J. F., *J. Chem. Phys.*, **74**, 4800, (1981).